Adaptive Optics for Optical Coherence Tomography

by David Merino

The thesis is submitted to National University of Ireland, Galway for the degree of PhD in the Faculty of Physics

National University of Ireland, Galway
Ollscoil na hÉireann, Gaillimh

PHYSICS DEPARTMENT, APPLIED OPTICS GROUP

Contents

List of Figures

List of Symbols

α: Angle to optical axis

β: Angle to optical axis

$\gamma(\tau)$: Complex degree of coherence

$\Delta\nu$: Full width at half maximum of the power spectral density of the light source

$\Delta\lambda$: Bandwidth of the light source

ΔL: Depth resolution of an OCT system

ΔY: Dimension of the image in the y direction

Δz: Optical path difference between the object and reference arms in a Michelson interferometer

ϵ: Transmission coefficient of the optical instrumentation in the reference arm

E: Error function

ϕ: Average tilt of the wavefront over a lenslet area

$\Phi_i(x, y)$: Set of vectors that form a complete basis over the pupil area

ζ: Conversion factor from voltage applied to deflection in the scanning mirror

κ: transmission coefficient of the directional coupler

λ: Wavelength

λ_0: Central wavelength

μ: Center of a gaussian function

ν: Frequency

ν_0: Central frequency

Π: Polarization factor

ρ: Distance to the optical axis

σ: Full width at half maximum for a Gaussian function

τ: Time delay

ψ: Transmission coefficient of the optical instrumentation in the object arm

Ω: Surface deformation for a bimorph mirror

φ: Phase

a: Coefficient of a certain Zernike polynomial, element of vector $\mathbf{A}$

$\mathbf{A}$: Vector formed by the coefficients of the Zernike polynomials

AO: Adaptive optics

B: Bandwidth of the image

BS: Beam splitter

c: Light speed

c: Element of the matrix forward matrix $\mathbf{C}$

$\mathbf{C}$: Forward matrix

C: Weighed sum of the square errors of the spot intensity centroids

d: Diameter of the spot

D: Diameter of the lens

DAC: Digital to analogue converter

ds: Displacement of the spot in the Shack-Hartmann wavefront

DC: Directional coupler

e: Electron charge

$\overrightarrow{E}$: Electric field

e_i: Lattice vectors

E: Lattice matrix (Fourier space)

f: Focal length

F: Frequency

F_z: Frequency of scanning along the z (optical) axis

FT: Fourier transform

$FWHM$: Full width at half maximum

$g_{i,j}$: Pixel grey level

g: Gain

G: Transfer function

GF: Gaussian function

$h(\eta)$: Electric field distribution (η is defined in eq. 2.1)

H: Feedback parameter

i: Electric current intensity

I: Light intensity

J_1: Bessel function of the first kind of order one

k: Wave number

k_B: Boltzmann constant

k_i: Periodicity of the spots lattice

K: lattice matrix (real space)

l_c: Coherence length

LCI: Low coherence interferometry

m: Spot displacement

M: Integer index of the of the Newton rings

$MMDM$: Micromachined deformable mirror

n: Refractive index

N: Fresnel number (defined at eq. 2.9)

N_y: Number of pixels on the image in the y direction

N_z: Number of pixels in the z axis direction

NA: Numerical aperture

NFL: Nerve fiber layer

No: Noise (in signal to noise ratio)

$OCDR$: Optical coherence domain reflectometry

OCT: Optical coherence tomography

OPD: Optical path difference

P: Optical power

PSF: Point spread function

r: Radius

R: Radius of the Newton rings

R_L: Charge resistance

RMS: Root mean square

RPE: Retinal pigment epithelium

Sig: Signal (in signal to noise ratio)

$S(\nu)$: Power spectral density of the light source

SLD: Superluminescent diode

SLO: Scanning laser ophthalmoscope

SNR: Signal to noise ratio

st: Strehl ratio

t: Time

T: Temperature

u: Variable defined in eq. 2.10

U: Voltage applied to the scanning mirrors

UHR: Ultrahigh resolution

U_y: Voltage applied to the y scanning mirror

v: Voltage applied to a certain actuator of a wavefront corrector, element of the vector $\mathbf{V}$

$\mathbf{V}$: Vector for the voltage applied to the wavefront corrector actuators

$W(x, y)$: Wavefront surface

w: pixel weight for centroid estimation

z: Position along the optical axis, depth position

z_1: Object distance (from scanner to lens)

z_2: Image distance (from lens to eye pupil)

Z_n^l: Zernike polynomial

Summary

A novel combination of adaptive optics with high resolution imaging for the eye is presented. The adaptive optics corrects for the aberrations of the eye to benefit images simultaneously collected in two channels, an *en-face* OCT and a confocal channel. The system includes an adaptive optics closed-loop that uses a Shack-Hartmann wavefront sensor using a 37 actuators OKO membrane deformable mirror to correct for ocular aberrations. The correction of aberrations obtained by the adaptive optics closed-loop has increased the signal-to-noise ratio in images obtained from volunteer eyes.

1

Introduction

The human retina is an extremely complex structure that is composed of six different types of neuron cells and ten histological layers within a depth of a few hundred microns. Imaging the retina with high resolution is essential in order to detect diseases or defects that affect its performance. Confocal scanning laser ophthalmoscopy (SLO) is a flying spot imaging technique based on confocal microscopy that is used to obtain high resolution retinal images of the *en-face in-vivo* human eye [93, 92]. Scanning mirrors are used to sweep the probing beam over the retina. A pinhole is placed in a plane conjugate to the depth of the retina that is being imaged to block spurious light coming from scattering bodies that lie at other depths. This provides the system with the capability of optical depth sectioning. The achievable resolutions of an SLO system are typically of around 300 μm in depth and 10 μm lateral [51].

The performance of SLO is mainly limited by the aberrations of the patient's eye, since the images are obtained through its optics. These aberrations vary

widely between subjects [60], and are not constant in time [47]. Adaptive optics (AO) has been demonstrated as a suitable method to correct for these aberrations [57]. AO-SLO systems have been presented showing 100 μm depth resolution and 2.5 μm lateral resolution [82].

Optical coherence tomography (OCT) [49] is a technique based on low coherence interferometry [7, 101] that is able to reconstruct tomographic (sectional) images of the object under study. It is usually implemented as a Michelson interferometer, in which the pattern of interference between the reference and object beams is used to determine the amount of light reflected back from a certain point within the volume of the object under study. A broad band source is used for illumination, and the two beams will only produce an interference pattern when their optical paths differ by less than the coherence length of the source. The bandwidth of the source determines the depth resolution of the OCT system. Lateral resolution achieved by OCT for retinal imaging is comparable to that obtained using SLO, but depth resolution is significantly higher, since it can reach values of just a few microns depending on the linewidth of the light source used.

Similar to SLO, lateral resolution in OCT for retinal imaging is limited by the aberrations of the patient's eye. AO has also been used to improve the performance of OCT for retinal imaging [46, 103]. An increase in the signal-to-noise ratio (SNR) of about 10 dB has been reported in OCT when AO was applied.

Speckle noise is very important in OCT images, and sometimes it makes it difficult to identify scattering bodies in the retinal images. On the other hand, the effect of speckle noise in SLO images is almost negligible. In this

sense, it would be advantageous to combine OCT with confocal imaging in order to synergetically benefit from the combination of information provided by the two images; low speckle noise in the SLO image, and high depth resolution on the OCT image.

Due to the use of longitudinal scanning to obtain traditional OCT images, these lie in a plane parallel to the optical axis and either the x or y axis, i.e., they lie on a plane perpendicular to that of the images obtained using SLO. In the case of *en-face* OCT, scanning mirrors are used to move the focused probing beam over the surface of the object under study to be imaged. The scanning configuration in *en-face* OCT is very similar to that used in SLO. The fast scanning is along the line in the raster (C-scan). This allows configuring an *en-face* OCT [71] system into a dual channel OCT/SLO that is able to generate simultaneously both *en-face* OCT and SLO images. These images have pixel to pixel correspondence [71, 70, 72].

The work presented in this Thesis is an extension of the work carried out by Podoleanu *et al*, in which they have developed a technique to obtain *en-face* OCT images from several different samples, that include biological tissues such as teeth and skin. This Thesis concentrates in the application related to retinal imaging of the *in-vivo* human eye. The main advantage of the technique presented by Podoleanu *et al* is the fact that due to the scanning method used to obtain the OCT images, the system can be easily modified to obtain simultaneously SLO images of the sample. SLO images do not present such high level of speckle noise as OCT images do. This, and the fact that the longitudinal resolution of SLO images is not as small as that for OCT images, makes them useful to place the OCT images into context.

Some work has been presented implementing adaptive optics with OCT. To our knowledge, the work presented here supposes the first implementation of an *en-face* OCT system combined with SLO using the technique developed by Podoleanu *et al.* together with adaptive optics.

The main results of this Thesis have been published [64] and several conference talks were presented during the course of this work [63, 20, 19, 68]

2

Scanning Laser Ophthalmoscopy

Scanning laser ophthalmoscopy is a technique used to obtain images of the *in-vivo* human retina. Images from different depths of the retina separated by a few hundred microns may be acquired using this technique by means of a small pinhole that blocks light scattered from other depths.
Based on confocal microscopy, it uses scanning mirrors in order to change the lateral position of the point of the retina that is being imaged, producing a point-by-point image of the sample. In this chapter a brief introduction to the technique is presented.

2.1 Confocal Microscopy

Confocal microscopy is an imaging technique that provides images from a prescribed section of a thick translucent object, with minimum disturbance due to the out-of-focus information from the adjacent sections. The term confocal refers to the fact that a detector pinhole is placed in the image plane of the layer in the object to be imaged, as it can be seen in fig. 2.1.

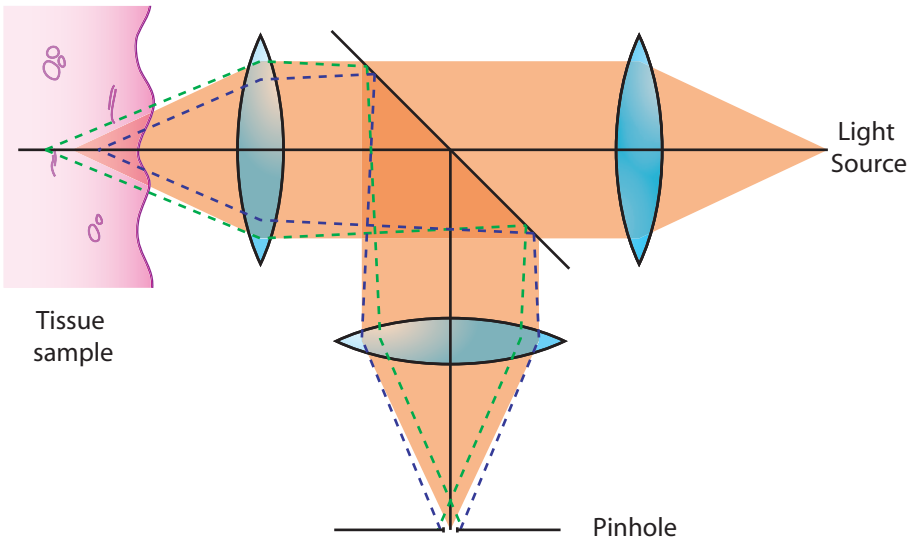

Figure 2.1: Confocal microscope

A pinhole is placed on a plane conjugate to the depth of the layer of the sample that is being imaged to block spurious light coming from scattering bodies that lie at other depths. This provides the system with the capability of optical depth sectioning. In the figure it can be seen how rays coming from different depths to that conjugate to the pinhole are mostly stopped on the pinhole, and thus the intensity in the detector plane is mainly due to light coming from the selected layer.

2.1.1 Lateral resolution

In confocal microscopy only one point is illuminated at a time, since the technique is only capable to image a point (the rest of the light is stopped by the pinhole). In order to determine the lateral resolution of such system, let us first consider the case of a standard microscope. If ideal operation is considered, the point on the object is imaged as a diffraction-limited spot

on the detector via the objective lens. The electric field distribution on the detector plane, $h(\eta)$, is given by the point spread function (PSF) of the objective lens [97]:

$$h(\eta) = \frac{2J_1(\eta)}{\eta} \tag{2.1}$$

where

$$\eta = \frac{2\pi}{\lambda}\rho n \sin(\alpha) \tag{2.2}$$

$n\sin(\alpha)$ is the numerical aperture, NA, of the objective, given approximately by $D/(2f)$, and ρ is the distance to the optical axis.

In the case of a standard microscope operated in incoherent imaging mode, only light intensities should be considered, and not electric fields. Consequently the intensity point spread function is:

$$I(\eta) = |h(\eta)|^2 = \left(\frac{2J_1(\eta)}{\eta}\right)^2 \tag{2.3}$$

This function describes the Airy disc, and the first zero of this function is at $\eta_0 = 1.22\pi$. The diameter of the first ring of zero intensity is then:

$$\rho_0 = \frac{\lambda}{2\pi\sin(\alpha)} 1.22\pi = 0.61\frac{\lambda}{n\sin(\alpha)} \tag{2.4}$$

If we consider the resolution of the system to be the diameter of the ring where the intensity of the spot is half the intensity in its center, i.e., full width at half maximum (FWHM), then this diameter is:

$$d_{FWHM} \approx 0.5\frac{\lambda}{NA} \tag{2.5}$$

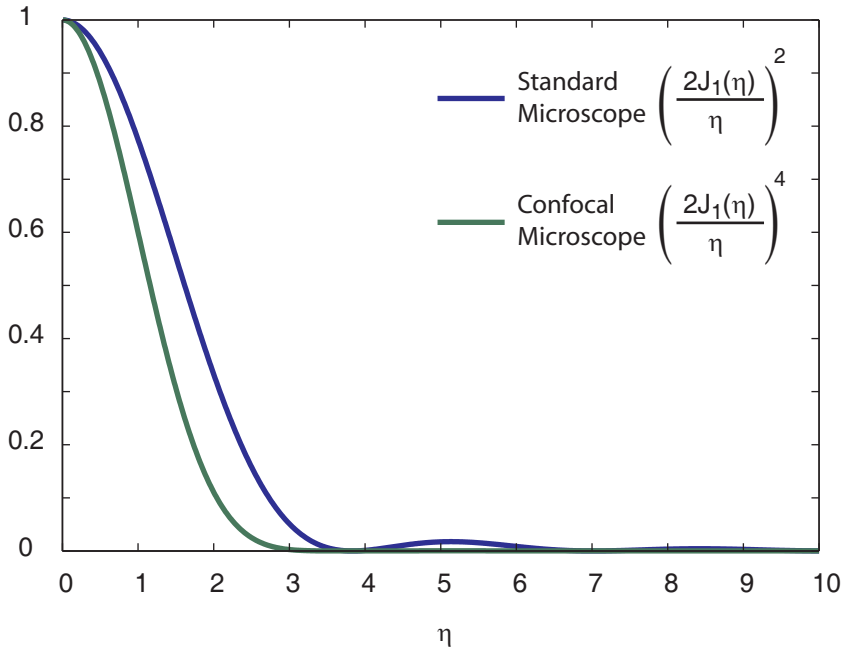

Figure 2.2: Light intensity distribution from an illuminated point for a standard and a confocal microscope

This is the size of the spot for a conventional microscope. In the case of a confocal microscope, and because the light has to go through one of the lenses twice, the light intensity distribution in the detector plane is given by the square of eq. 2.3.

$$I(\eta) = \left(\frac{2J_1(\eta)}{\eta}\right)^4 \tag{2.6}$$

The intensity distribution has the same zeroes as for a standard microscope, but the central peak is sharpened as it can be seen in figure 2.2, and the FWHM is reduced by a factor of 1.4:

$$d_{Conf,FWHM} \approx 0.3\frac{\lambda}{N.A.} \tag{2.7}$$

2.1.2 Depth profile

So far the transverse resolution for both standard and confocal microscopes has been determined. In this section the variation of the signal returned along the optical axis is also determined. Let us consider the situation in which a mirror is used as object. The resulting profile for the intensity returned from a mirror to the photodetector equipped with an infinitesimal pinhole and moving along the optical axis is described in the paraxial approximation by the following equation [97]:

$$I(u) = N^2 \left(\frac{\sin(u/2)}{u/2} \right)^2 \tag{2.8}$$

where N is the Fresnel number given by:

$$N = \frac{\pi D^2}{\lambda f} \tag{2.9}$$

Equation 2.8 is shown in figure 2.3, and u is defined as follows:

$$u = \frac{8\pi}{\lambda} zn \sin^2 \frac{\alpha}{2} \approx \frac{2\pi}{\lambda n} zn^2 \sin^2 \alpha = 2z \frac{\pi}{\lambda n} NA^2 \tag{2.10}$$

$u = 0$ is the position corresponding to the photodetector placed in the focal point of the lens, i.e., it is in focus with respect to the illuminated point of the sample.

Using these results it can be shown that the FWHM for the expression of the intensity profile along the optical axis is as follows:

$$d_{FWHM} = 2z_{FWHM} = u_{FWHM} \frac{\lambda n}{\pi (NA^2)} = 0.89 \frac{\lambda n}{NA^2} \tag{2.11}$$

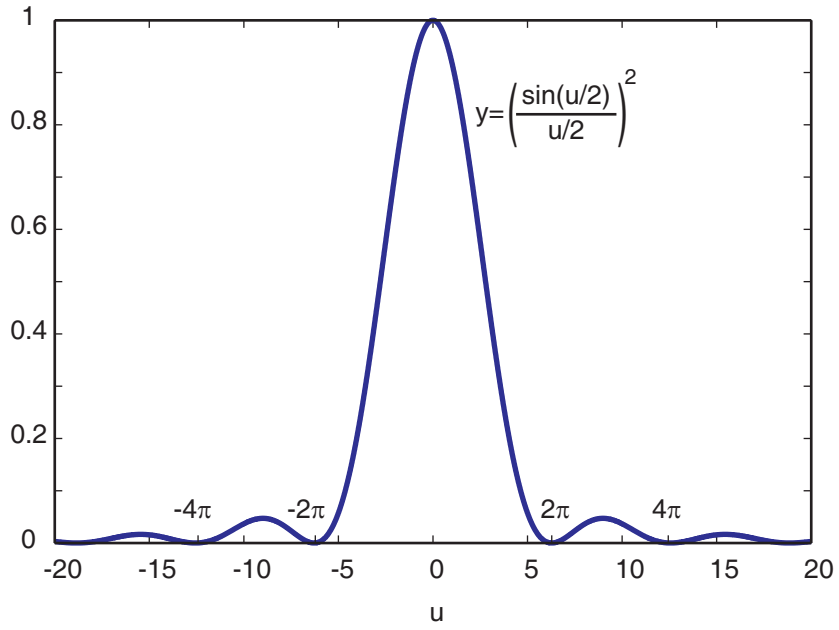

Figure 2.3: Intensity profile returned from a mirror along the optical axis for a confocal microscope equipped with an infinitesimal pinhole.

This result is the base of the capability of the technique to produce images of depth sections of the sample, since only light from a certain depth reaches the detector. Although so far it has only been explained how the system is able to produce the image of a point of the object, the following section will introduce the technique used to obtain two dimensional images of the sample, and in particular of the *in-vivo* human eye.

2.2 Scanning Optical Microscope

As already stated in the previous section, confocal microscopy is only valid to image a point in the object. In order to obtain a two dimensional image of the sample, the light spot has to be swept over the plane to be imaged. The intensity in the detector is recorded for each point and used to build a two

dimensional image of the corresponding layer in the sample. In order to sweep the beam over the sample, scanning mirrors can be used in several different configurations. One of these configurations for a scanning microscope used to image skin samples is shown in figure 2.4.

Figure 2.4.a shows a parallel beam incident to the scanner, where it is deviated a certain angle depending on the voltage applied to the scanner. Since the incident beam in the lens is collimated, the lens focuses it on its focal plane. The scanner is placed in the focal plane before the lens, therefore the central ray of the pencil of rays exiting the lens is parallel to the optical axis. By changing the voltage applied to the scanning mirror, the angle of deflection introduced by the scanner into the beam changes, and the point where the beam is focused on the sample can be moved along a line. Figure 2.4.b shows an extension of the scanning configuration for two scanners. This moves the point where the beam is focused over a plane surface, therefore by collecting the light scattered back from the sample over the whole surface, a two-dimensional image can be built.

2.3 Scanning Laser Ophthalmoscope

Scanning laser ophthalmoscopy (SLO) [92, 93] is an application of scanning confocal microscopy to retinal imaging. A beam of light is shone into the eye in order to collect the light scattered back from the different layers of the retina. The fact that the retinal images are obtained through the optics of the eye introduces a series of limitations that need to be considered in the configuration of the scanning optics. The first point to be considered is that the light beam needs to go through the center of the eye's pupil independently

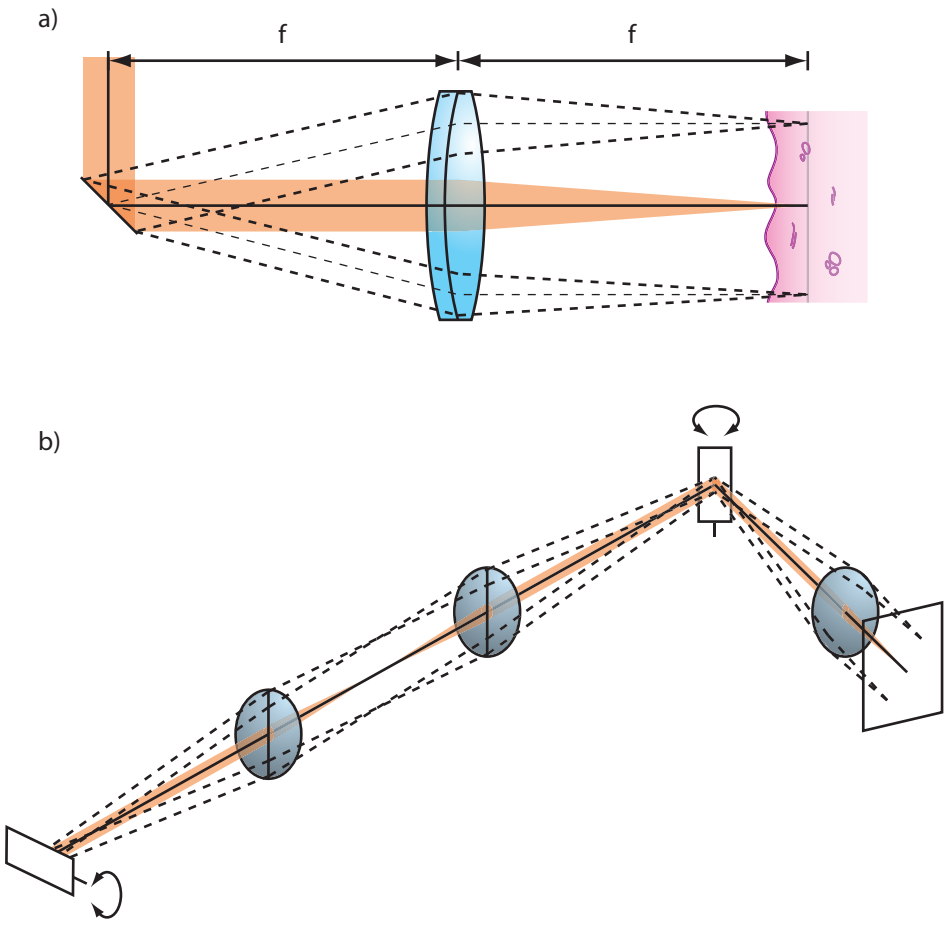

Figure 2.4: Scanning configuration for a confocal microscope used to image skin samples. a) Detail of the scanning configuration in one axis. b) Extension of the previous figure to produce two-dimensional images using two scanning mirrors rotating in perpendicular directions.

of the voltage applied to the scanners. The second issue to be considered is the fact that the eye itself includes a series of refractive surfaces. In a simple eye model, these surfaces can be considered as a lens in the pupil plane, and this lens should be considered in the design. Two different scanning configurations for an SLO are shown in figure 2.5.

Figure 2.5.a shows a scanning system built using one lens. The distances from the scanner to the lens, z_1, and from the lens to the eye pupil, z_2, follow the lens equation:

$$\frac{1}{z_1} - \frac{1}{z_2} = \frac{1}{f} \tag{2.12}$$

This ensures that independent on the angle of deflection introduced by the scanner, the beam is always going through the center of the pupil. On the other hand, the beam is converging when reaching the scanner, focusing in the focal plane of the lens. This ensures that the beam is collimated by the lens, and thus, assuming the eye is not affected by defocus, the beam is finally focused on the retina.

Figure 2.5.b shows another scanning configuration using two lenses. The lenses form a 4f system, where the scanner is placed in the focal plane of the first lens. This plane is imaged in the focal plane of the second lens, ensuring that the beam always passes through the center of the pupil independently of the angle of deviation introduced by the scanner. The beam reaching the first lens is parallel, and therefore it is also parallel after passing through the second lens, and similarly to the previous case, it is focused on the retina by the optics of the eye.

It will be explained in more detail in following chapters how this configuration

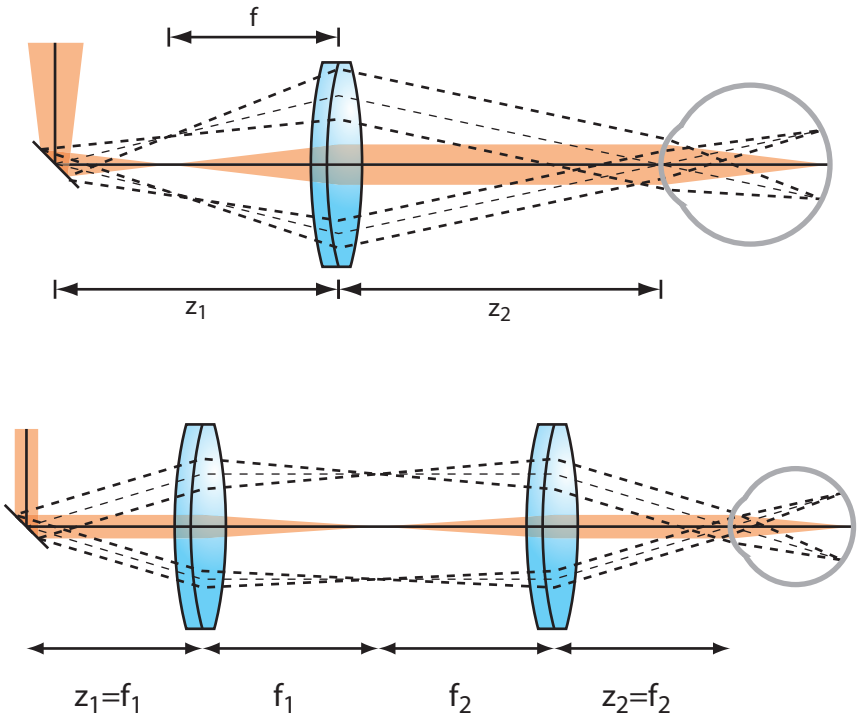

Figure 2.5: Example of two different scanning configurations for an SLO. a) Only one lens is used. The image of the scanner plane falls on the pupil of the eye, therefore the beam always passes through the center of the pupil of the eye. The beam is focused at the focal plane of the lens, so the beam is always parallel after passing through the lens. b) Two lenses are used in this case. The scanner is at the focal plane of the first lens, ensuring that the beam always passes through the center of the pupil. The beam is parallel before the first lens, thus it is also parallel after passing through the second lens. In both cases, the beam is finally focused on the retina by the optics of the eye itself.

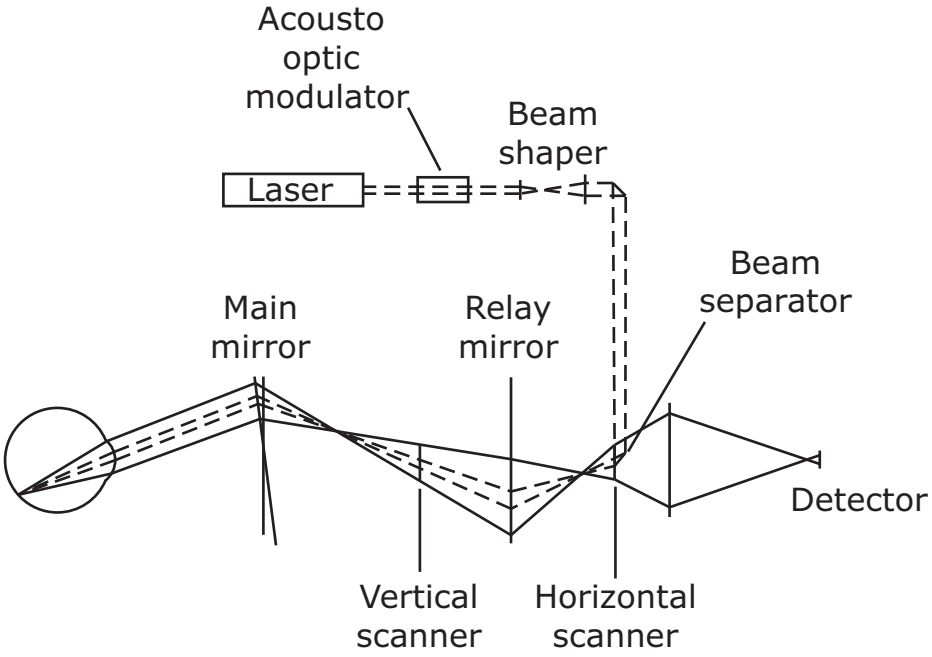

Figure 2.6: Example of the implementation of an SLO, from [92]

is more convenient for the combination of adaptive optics with SLO, since the scanner plane is a conjugate of the pupil plane.

In figure 2.6 a possible implementation of an SLO system is presented.

Using SLO images have been obtained from the *in-vivo* human retina presenting depth resolution of up to approximately $200\mu m$ and lateral resolution of up to approximately $6\mu m$ [51]. It can be easily seen that the theoretical values for both the lateral and depth resolution of an SLO system calculated using equations 2.7 and 2.11 respectively are better than those just mentioned. This is due to the fact that in order to obtain those equations, all the optical elements in the system have been considered to be diffraction limited. Unfortunately, this assumption is not valid for the optics of the human eye, as it will be detailed in chapter 4.1. This has a clear impact on the performance of an SLO system. In chapter 5 it will be explained how

adaptive optics can be used to correct ocular aberrations, and how it can be combined with SLO in order to improve the lateral and depth resolution of images obtained from real eyes.

3

Optical Coherence Tomography

Tomographic techniques produce two-dimensional sectional images of the internal structure of a sample. OCT is a non-invasive technique, that creates these images without damaging the sample. Due to this characteristic, the technique is very suitable to image biological tissue, since there is no need for a biopsy in order to obtain an image.

OCT has been used to obtain images of several different kinds of biological tissue, such as skin, teeth, muscles and others [18]. In this chapter it is introduced, concentrating mainly in *en-face* OCT, and explained how it can be used to obtain *in-vivo* retinal images of the human eye. It will be described how this technique can be combined with SLO, in order to produce pairs of simultaneous images using both techniques. It is also explained how these pairs of images may produce more information for a visual scientist than an OCT or SLO image on its own.

3.1 Introduction

OCT is an extension of optical coherence domain reflectometry (OCDR)[101], a technique based in low coherence interferometry (LCI) , where a low coherence light source is used in an interferometer to determine the position of a reflective surface with very high resolution. In the case of OCDR, one-dimensional profiles of reflected light intensity from the internal structure of an object are obtained by means of an oscillating mirror placed in the reference arm of the interferometer. The light source used in this technique has a wide spectral bandwidth, which translates into a very short coherence length, therefore interference in the detector of the interferometer only occurs between light from the object and reference arms that have travelled the same optical path, discriminating light scattered from other depths. The oscillating mirror in the reference arm changes the optical path length of that arm, and the amount of light scattered back from each depth in the sample can be determined by means of the interference amplitude measured for each position of the depth scanning mirror.

Several different techniques have been developed from the principles of OCDR. Time domain OCT is a technique that produces two dimensional images of the internal structure of the sample. In traditional time domain OCT two different scanning procedures are used in order to obtain an image: a depth scan using time-domain low coherence interferometry and a lateral scan addressing laterally adjacent positions to determine the location of light scattering bodies in the sample. This scanning configuration produces longitudinal images, i.e., parallel to the optical axis of the object arm. *En-face* OCT is based in this technique, but there is no depth scan. The images are not longitudinal,

but they are perpendicular to the optical axis; the name *en-face* refers from this orientation. In this technique two rotating mirrors are used in order to laterally sweep the object beam over a plane in the sample under study, as it will be explained in more detail in following sections. The work described in this Thesis is based on time domain OCT, and therefore special attention drawn to it. However, other variants of the technique have been developed, that are briefly mentioned below.

Frequency-domain OCT, also called Fourier-domain OCT, is one of these variants of OCT, where a diffraction grating is used in order to obtain a Fourier transform of spectrally resolved amplitude and phase data of the back-scattered object wave. The set-up for this particular variant of OCT corresponds to a Michelson interferometer with a spectrometer at its exit. Whereas in time domain OCT two scans have to be performed in order to obtain an x-z or y-z image, only one lateral scan needs to be performed in the case of frequency-domain OCT since a whole depth (z) profile is obtained at once without scanning in depth. This means the images can be obtained faster using this technique compared to time-domain OCT. However, an inconvenient of this characteristic may be the fact that while the whole depth scan is obtained at once, the system can only be focused at one depth, and therefore the images may be mostly out of focus.

Another variant of the technique is Doppler OCT [99]. In this technique Doppler velocimetry is combined with optical coherence tomography to detect the frequency shift in the light scattered back from moving particles and determine their velocity.

These are the most commonly used variants of OCT, although some other

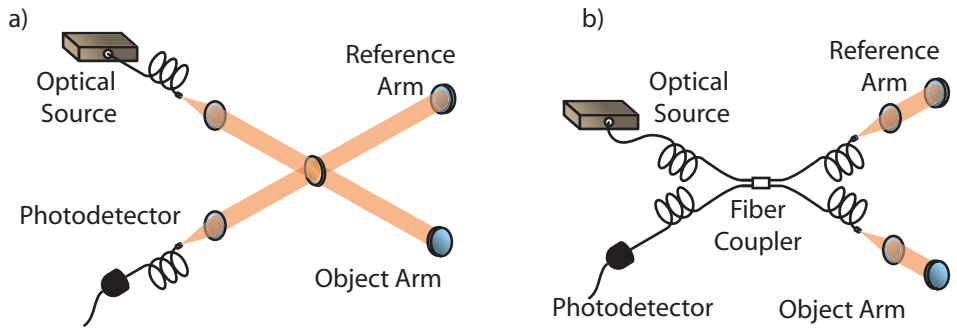

Figure 3.1: (a) Open space and (b) fiber optics implementations of a Michelson Interferometer

have been developed, such as full-field [29, 38] or polarization sensitive OCT. In the case of the work presented in this Thesis, only time domain OCT has been used, and therefore, only this variant is detailed in the following sections.

3.2 Michelson Interferometer

As already stated, OCT is based on a Michelson interferometer, in which light from a source is split into the light going to the sample under study and that used as reference. The sample under study is placed in the arm that is referred to as the object arm and the other is the reference arm. Two different implementations of a Michelson interferometer are shown in fig. 3.1: one is in open space and the other uses optics fibers. This last implementation can be more convenient sometimes, since it is easier to align and is more compact.

The light beams reflected back from both the sample and the reference arm are directed into a photodetector. OCT uses ballistic and near-ballistic pho-

tons. This means that, although the photons are scattered back in the sample, it is considered that their time-coherence and space-coherence is preserved. In the case of light scattered at large probing depths, incoherent photons will dominate, and the following mathematical treatment will no longer be valid [33]. For this reason, and also to ensure at this stage that the light from the object arm is scattered back only at a particular depth, let us consider that the sample in the object arm is a perfect mirror. This mirror is perfectly flat, and does not alter the time-coherence and space-coherence characteristics of the light reflected from it. Once this considerations are taken into account, the light intensity in the photodetector is then

$$I = < (\overrightarrow{E_{obj}} + \overrightarrow{E_{ref}})^* \cdot (\overrightarrow{E_{obj}} + \overrightarrow{E_{ref}}) > \quad (3.1)$$

$$= I_{obj} + I_{ref} + < \overrightarrow{E^*_{obj}} \cdot \overrightarrow{E_{ref}} + \overrightarrow{E^*_{ref}} \cdot \overrightarrow{E_{obj}} > \quad (3.2)$$

$$= I_{obj} + I_{ref} + 2\sqrt{I_{obj} I_{ref}} Re\{\overline{\gamma(\tau)}\} \quad (3.3)$$

where $\overrightarrow{E_{obj}}$ and $\overrightarrow{E_{ref}}$ are the electric field in the detector related to the light reflected back from the object and reference arms respectively, and $I_{obj} =< \overrightarrow{E^*_{obj}} \cdot \overrightarrow{E_{obj}} >$ and $I_{ref} =< \overrightarrow{E^*_{ref}} \cdot \overrightarrow{E_{ref}} >$ are the light intensities reflected back from the object and reference arms. $\gamma(\tau)$ is the complex degree of coherence of the electric fields, and the temporal average is made over a period of time that is longer than the oscillation period of the electric fields. The complex degree of coherence, $\gamma(\tau)$, is defined as the normalized autocorrelation function of the electric field emitted by the light source:

$$\gamma(\tau) = \frac{< E^*(t)E(t+\tau) >}{< E^*(t)E(t) >} \quad (3.4)$$

The time delay τ between the light coming from each arm is related to the optical path difference between both arms of the interferometer.

According to Wiener-Khinchin theorem [37], $\gamma(\tau)$ is related to the power spectral density of the source, $S(\nu)$, as:

$$\gamma(\tau) = \int_{-\infty}^{+\infty} S(\nu) e^{-i2\pi\nu\tau} d\nu \tag{3.5}$$

which means that the power spectral density of a source is obtained by calculating the Fourier transform of the complex degree of coherence, and so the intensity of the signal from the interferometer depends on the power spectral density of the light source.

In the experiment described in this Thesis a superluminescent diode (SLD) was used as light source. In the case of SLDs, the power spectral density can be approximated by a Gaussian function:

$$S(\nu) = \frac{2}{\Delta\nu}\sqrt{\frac{\ln 2}{\pi}} exp\left[-4\ln 2\left(\frac{\nu-\nu_0}{\Delta\nu}\right)^2\right] \tag{3.6}$$

where the function shows a maximum at $\nu = \nu_0$, and $\lambda_0 = c/\nu_0$ is the central wavelength of the source. $\Delta\nu$ is the full width at half maximum (FWHM) of the power spectral density. Using this result in eq. 3.5:

$$\gamma(\tau) = exp\left[-\left(\frac{\pi\Delta\nu\tau}{2\sqrt{\ln 2}}\right)\right] exp\left(-j2\pi\nu_0\tau\right) \tag{3.7}$$

Figure 3.2 shows the profile of the real part of the complex degree of coherence versus the optical path difference between the two arms of the interferometer. Finally, the intensity variation due to the interference pattern in the detector is described by:

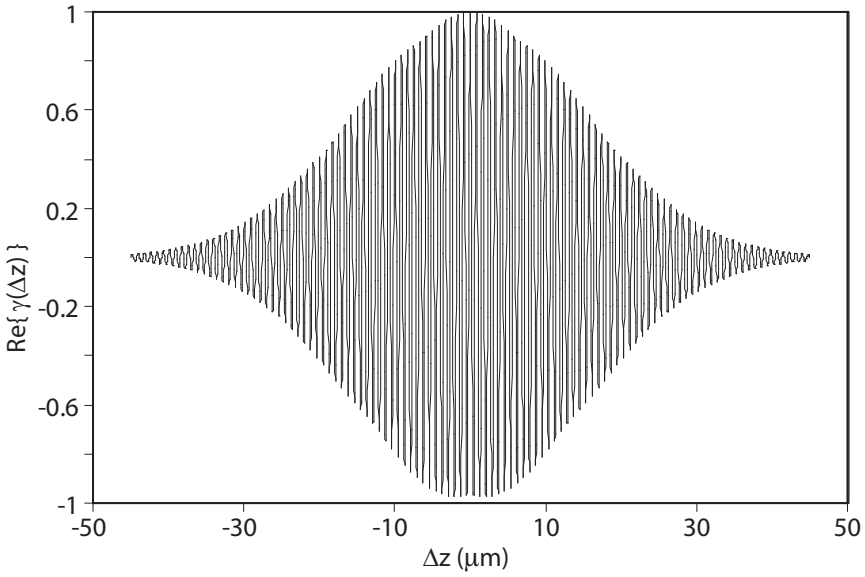

Figure 3.2: Real part of the complex degree of coherence versus the difference in optical path length between the two arms of the interferometer for a Gaussian light source with central wavelength 830.7 nm and 17 nm bandwidth, calculated using eq. 3.7.

$$
\begin{aligned}
I = \; & I_{obj} + I_{ref} + \\
& 2\sqrt{I_{obj} I_{ref}} exp\left[-\left(\frac{\pi \Delta\nu \tau}{2\sqrt{\ln 2/\pi}} \right)^2 \right] Re\left[exp\left(-j2\pi\nu_0 \tau \right) \right] \qquad (3.8) \\
= \; & I_{obj} + I_{ref} + 2\sqrt{I_{obj} I_{ref}} |\gamma(\tau)| \cos(2\pi\nu_0 \tau) \qquad (3.9)
\end{aligned}
$$

Eq. 3.9 describes a signal that has a certain background, $I_{obj} + I_{ref}$, with an oscillating term superimposed to it, that depends on the time delay τ between the light coming from each arm of the interferometer. This oscillating term is modulated by the complex degree of coherence, $\gamma(\tau)$, that sets the amplitude of the oscillation.

The visibility, V_{abs}, of the fringes can be defined as follows:

$$V_{abs} = \frac{I_{max} - I_{min}}{I_{max} + I_{min}} \qquad (3.10)$$

Using eq. 3.9, the visibility can be reduced to:

$$V_{abs} = \frac{2I_{obj}}{\sqrt{I_{obj} I_{ref}}} |\gamma(\tau)| \cos(2\pi\nu_0 \tau) \qquad (3.11)$$

where the assumption $I_{obj} \ll I_{ref}$ has been used to obtain this result.

Eq. 3.11 shows how the visibility of the fringes is modulated by the complex coherence function. As a conclusion, if $\gamma(\tau)$ is described by a Gaussian function, the visibility of the fringes is maximum when the time delay τ between light coming from the reference and object arms is zero, and it decays when the absolute value of τ increases. Since the time delay is related to the optical path difference, the function is maximum when the optical path difference between the arms is zero, and it also decays when the absolute value of this magnitude increases by moving the reference mirror either further or

closer. Finding the maximum visibility of the fringes, the position of the mirror in the object arm can be determined, with a resolution that depends on the width of the complex coherence function, $\gamma(\tau)$, and thus on the power spectral density of the light source used. At this point it is important to point out that the broader the power spectral density of the source, the narrower the complex degree of coherence, and the position of maximum visibility of the fringes can be determined with higher resolution. From this, it can be said that the broader the bandwidth of the light source used, the smaller the resolution of the OCT system.

3.3 OCT Signal

In the previous section, the light intensity profile in the photodetector of a Michelson interferometer in terms of the time delay between light coming from each arm has been determined. This expression can also be calculated in terms of the optical path difference between the arms of the interferometer, $\Delta z = 2(z_{ref} - z_{obj})$. To do so, the complex coherence function can be determined in terms of Δz, the same way it has been calculated in terms of τ. Its expression is:

$$\gamma(\Delta z) = exp\left[-\ln(2)\left(\frac{2\Delta z}{l_c}\right)\right] exp(-j2\pi\frac{\Delta z}{\lambda}) \tag{3.12}$$

where l_c is the coherence length of the source, which in the case of a source with a power spectral density described by a Gaussian function is given by

$$l_c = \frac{4\ln 2}{\pi}\frac{\lambda_0^2}{\Delta\lambda} \tag{3.13}$$

where $\Delta\lambda = \lambda_0^2 \Delta\nu / c$. For instance, the source used in the work described in this Thesis emits at 830.7 nm with 17 nm spectral bandwidth, therefore the coherence length is 35 μm.

Using these results, eq. 3.2 can be written in terms of the optical path difference between the interferometer arms as follows

$$I = I_{obj} + I_{ref} + 2\sqrt{I_{obj} I_{ref}} |\gamma(\tau)| \cos\left(\frac{2\pi}{\lambda} \Delta z\right) \tag{3.14}$$

Let us concentrate in the second part of the equation, that includes the oscillating term that modulates the light due to the optical path difference between the reference and object arms:

$$I_{OSC} = 2\sqrt{I_{obj} I_{ref}} |\gamma(\tau)| \cos\left(\frac{2\pi}{\lambda} \Delta z\right) \tag{3.15}$$

As it has been mentioned in section 3.2, this result is valid for the case in which the object is an ideal mirror, and light is only reflected at the mirror surface. If the object is a sample of biological tissue, light will be scattered back simultaneously from scattering bodies in the tissue placed at different depths. The reflectance of these scattering bodies can be referred to as $O(z_0)$. The confocal response of the system $I_{depth}(z_0/2)$ will be introduced in the calculation at this point. The intensity of light reaching the detector also depends on this factor, that has been described in detail in chapter 2.1.2. Finally, the oscillating term of the intensity is the integral of the contribution of the light reflected back from the biological tissue at all depths:

$$I_{OSC} = 2\sqrt{I_{ref}} \int_{-\infty}^{+\infty} \sqrt{O(z_0) I_{depth}(z_0/2)} |\gamma(\tau)| \cos\left(\frac{2\pi}{\lambda} \Delta z\right) dz_0 \tag{3.16}$$

The expression shows how the OCT signal is related to the convolution of the modulus of the complex degree of coherence of the source and the square root of the reflectance of the object multiplied by the confocal response of the object arm. If there is only one scattering body placed at z_0, then $O(z_0)$ is a constant O, positive and smaller than 1, and in the particular situation in which the confocal response is broader than the complex coherence function, the signal measured in the detector is [84]:

$$I_{OSC} = 2\sqrt{I_{ref}}\sqrt{O}|\gamma(\tau)|\cos\left(\frac{2\pi}{\lambda}\Delta z\right) \tag{3.17}$$

Up to this point, the polarization of the light used has not been considered. A factor Π is introduced, that takes this characteristic into account:

$$I_{OSC} = 2\Pi\sqrt{I_{ref}}\sqrt{O}|\gamma(\tau)|\cos\left(\frac{2\pi}{\lambda}\Delta z\right) \tag{3.18}$$

This polarization term, Π, will be ignored from now on, because in the case of the fiber optics implementation of the Michelson interferometer, there are devices that can be used to change the polarizing characteristics of the fibers in order to match the polarization of the reference and object beams. In this situation the polarization term becomes 1 and the signal in the interferometer is maximized.

3.4 Longitudinal Optical Coherence Tomography

Once the theoretical expression of the OCT signal has been introduced, it is possible to explain the method used to obtain a longitudinal image using a traditional OCT system.

When a certain sample is placed in the object arm of the interferometer, there is light reflected not only from one, but from all the the layers of the sample up to the probing depth of the system. It has also been explained how due to the broad power spectral density of the light source used, interference in the photodetector will only occur with light from the object arm that matches the optical path covered by light reflected from the reference arm. The amplitude of the interference of light that does not match the phase of light reflected from the reference arm will be low and will not contribute to the overall signal. The amplitude of the recorded interference is therefore related to the amount of light scattered from the object arm at the particular depth that matches the position of the reference mirror, and thus it indicates the presence or not of a scattering body at that depth. By scanning the reference mirror a profile of the reflectance of the sample along the optical axis, or A-scan, is obtained as shown in figure 3.3.

In order to obtain a two-dimensional image many of these A-scans are needed, from equally spaced adjacent positions. This may be achieved by slowly moving the sample with respect to the system in a direction perpendicular to the optical axis, at a speed sensibly slower than the speed at which the reference mirror is scanning in depth. Then the reflectance information from these A-scans is collected in order to built a longitudinal image, or B-scan as shown in fig. 3.3. It is also possible to keep the sample at the same position at all times, and somehow change the position at which the probing beam is focusing on the sample. Scanning mirrors are commonly used to perform this task. Some of the methods used to do so are detailed for example in section 3.5. It is necessary at this point to introduce the concept of *en-*

face images. These kinds of images may be both longitudinal (along the optical axis) or transversal (perpendicular to the optical axis). However, in *en-face* longitudinal images, the fast scanning direction is perpendicular to the optical axis, therefore the depth scanning mirror in the reference arm moves at a speed sensibly lower than the speed at which the lateral scanner vibrates.

Finally, C-scans are created using two different lateral scanners, but no depth scanning is performed. This method will be explained with more detail in following sections.

3.4.1 Depth resolution

The depth resolution of the system is the smallest distance that can be discriminated between two different diffusers situated along the propagation direction in the object arm. Due to the double pass of the light in the object arm, the depth resolution of an OCT system is half the coherence length of the source, and can be written in the case of a Gaussian light source as:

$$\Delta L = \frac{l_c}{2n} = \frac{2\ln 2}{n\pi}\frac{\lambda_0^2}{\Delta\lambda} \tag{3.19}$$

where n is the refraction index of the sample. In the particular case mentioned before of an SLD source with $\lambda_0 = 830.7nm$ and $\Delta\lambda = 17nm$ in the situation in which the refraction index of the sample is 1.33, the depth resolution is $\Delta L = 13.5\mu m$. The expression of the coherence length confirms the fact that the depth resolution is inversely proportional to the spectral bandwidth of the source, and for a source with very narrow bandwidth, like in the case of a laser with long coherence length, the resolution will be very

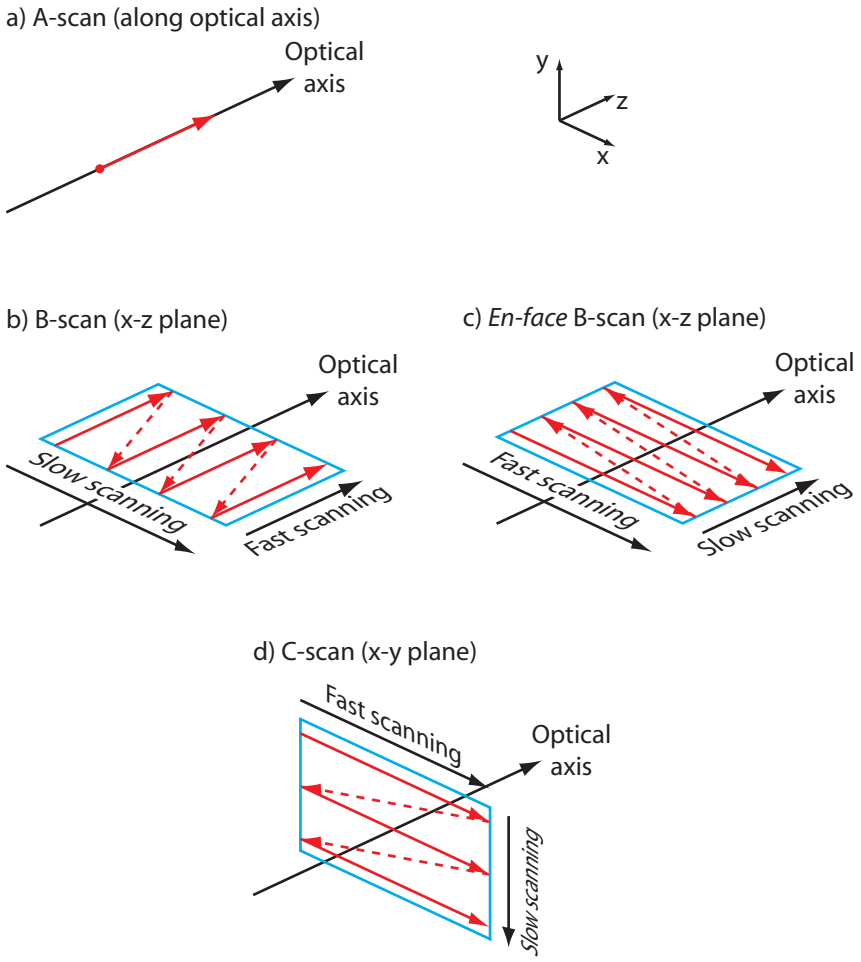

Figure 3.3: The figure shows different scanning configurations used in OCT

poor, while in the case of a source with wide bandwidth, like a white light tungsten lamp, the resolution will be high.

There are different broad band sources available to use on an OCT system. SLDs are available with $10 - 20\mu m$ coherence length, and in the case of multiplexed SLDs, the coherence length can be as short as $7 - 8\mu m$. Another option that is commonly used in OCT systems are femtosecond lasers. Cr^{4+}:forsterite lasers show a coherence length of $5-10\mu m$; Ti:sapphire lasers have a coherence length of $\sim 4\mu m$, and for sub-two cycles Ti:sapphire lasers it can be as low as $1\mu m$. However, thermal light has also been used in OCT, such is the case of a quartz tungsten white lamp light source, with $\sim 1\mu m$ coherence length.

SLDs are a good option as a light source for an OCT system because they have a broad power spectral density, and at the same time they can be pigtailed and optics fibers can be used to build the interferometer without much light loss. Another advantage of SLDs is the variety of wavelengths available in the range of the light spectrum called the therapeutic window [96]. The therapeutic window is the range of the spectrum in which the absorbance of water, melanin, haemoglobin and oxy-haemoglobin reaches a minimum, and it is comprised in the range of wavelengths between 600 and 1300 nm.

3.4.2 Dispersion

Up to this point of the introduction to longitudinal OCT it has been accepted the fact that there is no dispersive element in the system. Dispersion is due to the dependance of the phase speed of the optical radiation inside the

material with its wavelength. Let us consider the frequency-dependent phase introduced to the light wave when it propagates through a dispersive medium of path length Δz [32]:

$$\Phi_{Disp}(\nu) = k(\nu_0)\Delta z + (\nu - \nu_0)\dot{k}(\nu_0)\Delta z + \frac{1}{2}(\nu - \nu_0)^2\ddot{k}(\nu_0)\Delta z + \dots \quad (3.20)$$

where $\dot{k}(\nu_0)$ and $\ddot{k}(\nu_0)$ are respectively the first and second order derivatives with respect to ν of the wave number, k, calculated at $\nu = \nu_0$.

From the Fourier shift theorem, it follows that a multiplication of a function by a phase factor in Fourier space shifts the Fourier transform of that function in direct space. Therefore, using eq. 3.5:

$$\gamma(\tau + \Delta\tau) = FT^{-1}\{S(\nu)e^{-i2\pi\nu\Delta\tau}\} \quad (3.21)$$

An unmodified shift of the coherence function will only occur if the additional phase in the Fourier space is directly proportional to the frequency: $\Phi(\omega) = \omega\Delta t$. Thus, only zero-order dispersion shifts the coherence function without modification. Second and higher order dispersion will distort the Fourier spectrum and increase the coherence length degrading OCT depth resolution.

Although techniques for *a posteriori* dispersion compensation have been developed, dispersion effects may also be minimized by compensating the effect of dispersive elements in the object arm using pieces of glass and cuvettes containing water placed in the reference arm. Although perfect dispersion compensation is not possible when a certain sample is placed in the object arm of the interferometer because the distribution of materials in the sample

is unknown, the results obtained using glass and water to compensate for dispersion have proved satisfactory.

3.4.3 The bandwidth and electronic treatment of the signal

In the expression of the photocurrent given by equation 3.17 the phase difference between the reference and object beams is considered to be constant. When moving the depth scanning mirror along the optical axis, this situation changes. Let us consider this mirror is moved at a certain constant speed v. The difference between the lengths of the two arms changes at a rate given by:

$$\delta z = \delta z_0 + 2vt \tag{3.22}$$

where δz_0 is the optical path difference between the two arms just before the reference mirror starts moving. Using this result in equation 3.17

$$I_{OSC} = 2\sqrt{I_{Ref}O}|\gamma(\delta z_0 + 2vt)|\cos(\rho + 2\pi\nu_d t) \tag{3.23}$$

where $\rho = 2\pi\delta z_0$, and ν_d is the Doppler frequency of the signal, also referred to as heterodyne frequency or carrier, given by $\nu_d = 2v/\lambda$. Eq. 3.23 shows how the cosine function is modulated by the function $|\gamma(\delta z_0 + 2vt)|$.

Once the signal is detected it needs to be processed to obtain the OCT image. First, the signal is amplified, and then it is filtered using a band pass filter centered in the Doppler frequency. This filter will get rid of the constant component related to the background intensity reflected from the reference and object arms (I_{obj} and I_{ref} in eq. 3.14), as well as the oscillations on the intensity related to the interference between the two beams. The remaining

signal is related to the envelope of the signal. The bandwidth of the band pass filter used depends on the bandwidth of the OCT signal obtained, and it will be determined later in this section. After the signal has been filtered, it is rectified, changing its negative values into positive. Finally a low pass filter is used in order to eliminate the high frequency components generated in the rectifier. As a result, the envelope of the OCT signal containing the information of the depth profile of the reflectance can be obtained.

The bandwidth of the longitudinal OCT signal can be easily determined as follows. The pixel size in the image should be related to the depth resolution of the system. If the change in length of the reference arm is Δz, the number of pixels recorded, N_z, is

$$N_z = \frac{\Delta z}{\Delta L} = \frac{2\Delta z}{l_c} n \tag{3.24}$$

If the reference mirror is placed on top of a translation stage that oscillates at a frequency F_z, then the time needed to record the information from a pixel is $1/(N_z F_z)$ and the bandwidth of the OCT image is:

$$B = N_z F_z = \frac{2F_z \Delta z}{l_c} n \tag{3.25}$$

Since $\Delta z \simeq v/F_z$ and using the expression for the coherence length described in equation 3.13, then

$$B = 1.13 \times \frac{\Delta\lambda}{\lambda_0} \times \nu_d \times n \tag{3.26}$$

For the particular case of a source with central wavelength $830.7nm$ and with a spectral bandwidth of $17nm$, it leads to a 12 kHz Doppler frequency for a 5

mm/s translation speed. This results in a bandwidth of the image of around 275 Hz.

3.5 Transversal or *en-face* optical coherence tomography

In order to produce a transversal (*en-face*) image, the source beam needs to sweep the object point by point over the surface to be imaged. Usually, this is achieved by means of scanning mirrors that move the point where the beam is focused in the sample in the X and Y directions as shown in figure 3.3.c. There are several configurations that are valid in order to obtain transversal scanning. Figure 3.4.a shows a particular configuration for one scanner in which a telescope formed by two lenses is used. The configuration shown only scans in one direction, while scanning in two perpendicular directions is needed in order to obtain a two dimensional image. This one scanner configuration can be easily extended to scan in two directions by adding a new telescope and a scanning mirror rotating in a direction perpendicular to the first one, as shown in figure 3.4.b. Using Fourier optics it can be easily shown that, if the distances between the eye pupil and the lens is the appropriate, this configuration ensures that the pupil plane of the eye is conjugate to the two scanning mirrors planes. Therefore the phase distribution in the eye pupil plane of the wavefront emerging from the eye is replicated in the scanning mirrors planes. Although it will be explained in more detail in further chapters, it is worth mentioning at this point that this configuration is very convenient for adaptive optics. Further telescopes can be added to

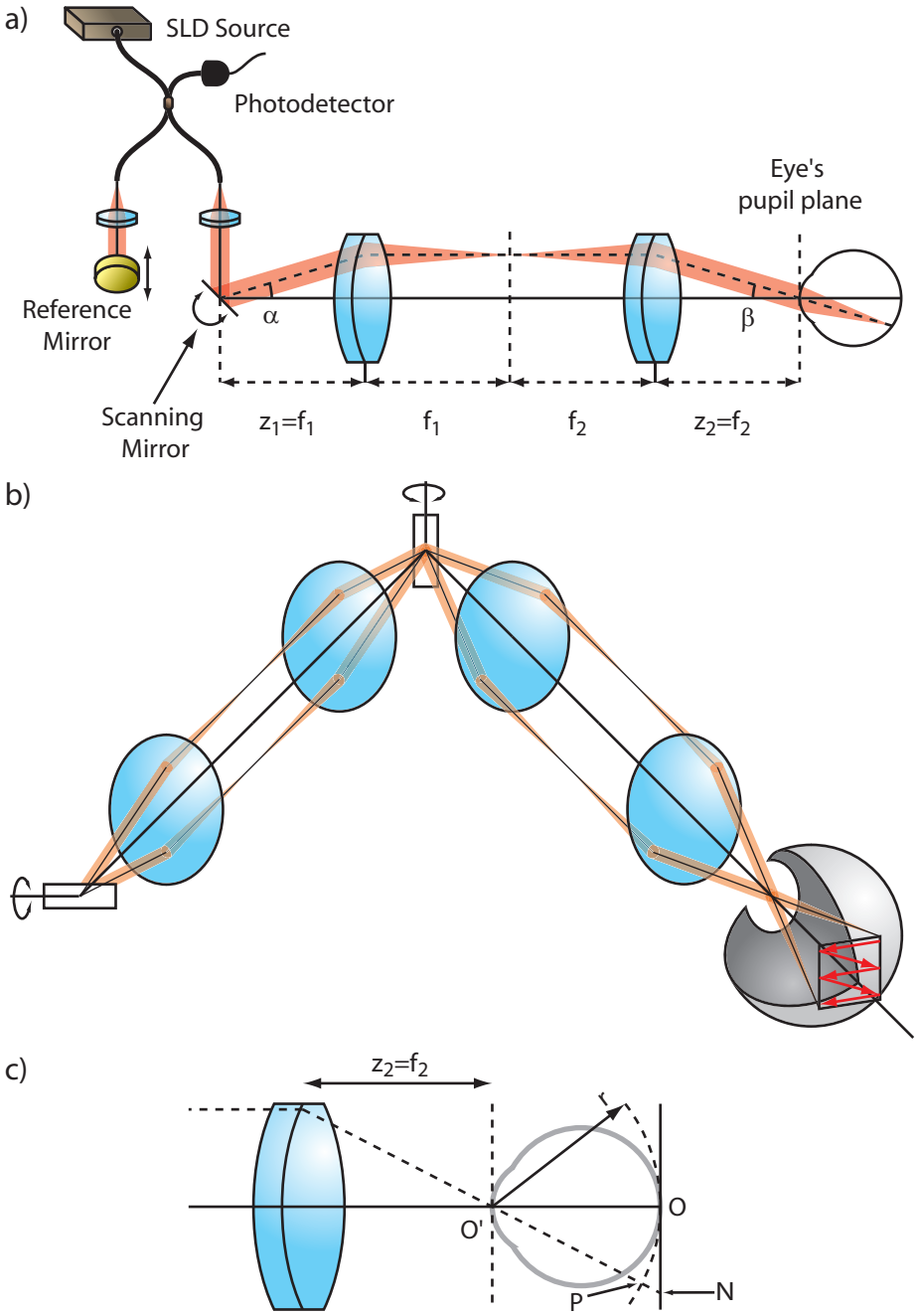

Figure 3.4: En-face *scanning configuration. a) Detail for one scanner. b) Extension for two scanners. c) Detail of the beam directions in the eye.*

the system to create new conjugate planes of the eye's pupil plane. These conjugate planes will be the positions at which the phase distribution of the emerging wavefront will be measured using a wavefront sensor and also corrected using a wavefront corrector. The fact that at those positions the phase distribution of the wavefront is replicated, ensures that the wavefront aberration measured and its correction correspond to the same quantities. This could not be ensured if the planes where the beam aberration is measured and corrected are not conjugate, since the aberration changes as the beam propagates.

The scanning configuration shown in figure 3.4.b also ensures that the probing beam is always going through the center of the pupil of the eye. Such situation avoids vignetting that could be introduced by the iris of the eye.

Let us consider that the scanning mirror is stopped in the position shown in figure 3.4.a, and the probing beam is at an angle β from the optic axis in the object arm. This discussion corresponds to the case of using one scanner, but can be easily extended to two scanners. Let us consider that the object is a mirror and that it is placed in a position where the optical path difference between the object and reference arm is zero when $\beta = 0$. For any other value of β, and using the notation from figure 3.4.a and c, the optical path difference between the two arms is:

$$\Delta z = 2(\overline{O'N} - \overline{O'P}) = 2r\left(\frac{1}{\cos\alpha} - 1\right) \tag{3.27}$$

The maxima in intensity in the detector will appear when the optical path difference between the two arms is a multiple of the wavelength $\Delta z_{Max} = M\lambda$. The angle $\delta\beta$ measured between two adjacent maxima of intensity is [71]:

$$\delta\beta \approx \frac{z_2}{z_1}\frac{\lambda}{2r\alpha} \tag{3.28}$$

If the scanning mirror is driven by a triangular voltage signal of amplitude U and frequency F then:

$$\beta(t) = 4\zeta UtF \tag{3.29}$$

where ζ is the conversion factor between the applied voltage and the deflection angle in the scanning mirror. Using this equation, the frequency at which the peak of light intensity are found in the detector is:

$$f = 4\zeta UF\frac{r\alpha}{\lambda_0} \tag{3.30}$$

This signal obtained in the detector is equivalent to that produced by a reference mirror that is moving at a speed v given by:

$$v = 4kUFr\alpha \tag{3.31}$$

In the case in which there are two scanning mirrors (one in the X and the other in the Y direction), the figure obtained in the detector consists of a series of concentric rings referred to as Newton rings [71], and the radius of these rings is determined by:

$$R_{Max}^{M} = \frac{2r + M\lambda}{2}\left[1 - \left(\frac{2r}{2r + M\lambda}\right)^2\right]^{1/2} \approx \sqrt{Mr\lambda} \tag{3.32}$$

where the approximation is valid for small angles and low values of M. The transversal resolution of the system is given by the distance between fringes. The distance between these fringes is not constant, and thus the transversal resolution is better the further from the optic axis.

3.5.1 Signal bandwidth and electronic processing of the signal

In order to determine the bandwidth of the transversal OCT signal, let us consider that the system is diffraction limited, and its lateral resolution can be written as:

$$\Delta r = \frac{1.22\lambda_0 f}{D} \tag{3.33}$$

where D is the diameter of the lens with focal length f. The number of pixels in the image in the Y direction is:

$$N_y = \frac{\Delta Y}{\Delta r} = \frac{D\Delta Y}{1.22\lambda_0 f} \tag{3.34}$$

where ΔY is the dimension of the image, that depends of the scanning angle of the rotating mirror. Since ΔY is related to the voltage applied to the mirror following:

$$\Delta Y = 4\zeta_y \frac{z_1}{z_2} f U_y \tag{3.35}$$

the resulting bandwidth of the signal is:

$$B = \frac{8\zeta_y D}{1.22\lambda_0} \frac{z_1}{z_2} F_y U_y \tag{3.36}$$

This result shows how the bandwidth of the transversal OCT signal is proportional to the frequency of oscillation of the scanning mirror.

The demodulation of the transversal OCT signal is made in similar way to the case of longitudinal OCT, the only difference is that after the signal is amplified, it is filtered using a high pass filter, and not a band pass filter. In this way, low frequencies are eliminated and transversal resolution gets closer

to that given only by diffraction. Finally, notice how the bandwidth of the electronic devices used to demodulate the transversal OCT signal need to be larger than for those used to demodulate the longitudinal OCT signal. This produces a reduction in the signal to noise ratio.

3.6 Noise in OCT systems

The capability of an OCT system to produce images with good quality is characterized by the value of the signal to noise ratio (SNR). Therefore it is essential to know the sources of noise as well as the possible causes of reduction of the value of the SNR in an OCT system.

3.6.1 Sources of noise

Thermal noise

Thermal noise is produced by random movements at finite temperatures of charge carriers inside resistive materials. These movements produce a certain electric current even in absence of optical radiation in the detector. The contribution of thermal noise to the photocurrent is expressed in terms of the variance of thermal photocurrent:

$$< \Delta i_T^2 >= \frac{4k_B T}{R_L} B \tag{3.37}$$

where B is the bandwidth of the electric circuit, k_B is the Boltzmann constant and R_L is the resistance of the charge resistance.

Shot noise

Shot noise is related to the fact that photons arrived randomly to the detector. Therefore, a flux of photons reaching the detector produces during an interval T a certain electric current $I = \frac{e}{T}n$, where e is the electron charge and n is the number of photo-electrons generated. This current will fluctuate, and the magnitude of these fluctuations is:

$$< \Delta i_{SN}^2 >= \left(\frac{e}{T}\right)^2 (< n^2 > - < n >^2) \tag{3.38}$$

This expression depends on the statistics of number of photo-electrons n. If the electrons are non-correlated, the probability to measure n electrons is described by Poisson statistics, where $< n^2 > - < n >^2 =< n >$. Therefore, and since the bandwidth of the electronic circuit, B, is given by $B = 1/2T$, the expression of the contribution of shot noise to the total photocurrent is:

$$< \Delta i_{SN}^2 >= 2e < i > B \tag{3.39}$$

Excess photon noise

Excess photon noise is characteristic of detectors with internal gain. It is due to the randomness of the amplification process. It can be shown that the contribution of the excess photon noise to the total noise can be expressed as:

$$< \Delta i_{EPN}^2 >= (1 + \Pi^2)\frac{B}{\Delta\nu_{eff}} < i >^2 \tag{3.40}$$

where Π is a factor related to the polarization state of the optical radiation, and $\Delta\nu_{eff}$ is the effective bandwidth of the light source, and it is defined by:

$$\Delta\nu_{eff} = \sqrt{\frac{\pi}{2\ln 2}}\frac{\Delta\lambda}{\lambda_0^2}c \tag{3.41}$$

Therefore, to reduce the excess photon noise it is necessary to maintain the bandwidth of the electronic device as low as possible, as well as the degree of polarization of light needs to be also low.

After the different sources of noise have been determined, and their expressions have been calculated, it is possible to obtain a mathematical expression for the total noise of the OCT system, that is as follows:

$$< \Delta i^2 >= \frac{4k_BT}{R_L} + 2eB < i > +(1+\Pi^2)\frac{B}{\Delta\nu_{eff}} < i >^2 \tag{3.42}$$

Finally, the signal to noise ratio is given by:

$$\frac{Sig}{No} = \frac{2I_{Obj}I_{Ref}}{\Delta i^2} \tag{3.43}$$

3.6.2 Signal to noise ratio in a balanced detection configuration

In this section we discuss how the noise in an OCT system can be reduced using a balanced detection configuration. First of all, it is known that the thermal noise does not affect the SNR considerably, since the other sources of noise are predominant [80]. It should also be considered the fact that the shot noise could not be completely removed since it is related to the detection process. Therefore, it is only the noise introduced by the internal gain of the detectors that can be somehow minimized, and balanced detection is used to do so.

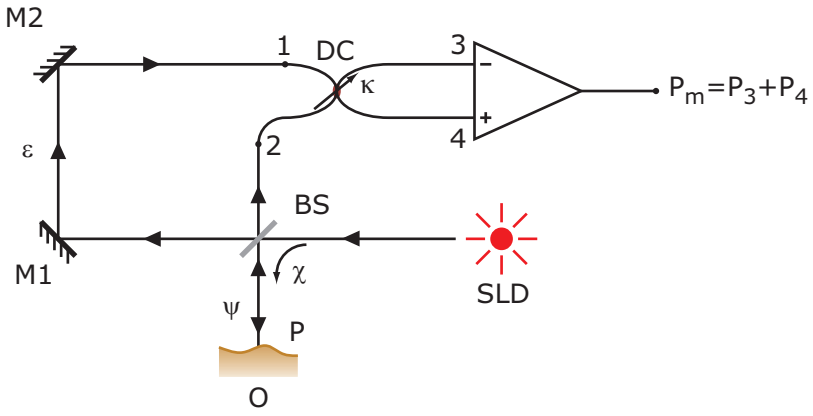

Figure 3.5: Layout of an OCT system based on balanced detection. χ is the reflection coefficient of the beam splitter (BS). ψ and ϵ are the transmission coefficient of the optical instrumentation in the object and reference arms respectively. γ is the transmission coefficient of the directional coupler (DC). O is the reflectivity of the object and P is the optical power reaching it.

In a balanced detection system, the common signals that vary in anti-phase between two detectors are extracted from a common signal in phase between the detectors. In order to successfully implement a balanced detection system it is necessary to have a 50/50 directional coupler (DC) or a 50/50 beam splitter (BS). Figure 3.5 shows an example of a configuration using a 50/50 DC. The main reason to a DC is the fact that at the output, points 3 and 4 in fig. 3.5, the electric fields of the two beams are in anti phase:

$$\begin{cases} E_3 = \dfrac{1}{\sqrt{2}}(E_2 - iE_1) \\ E_4 = \dfrac{1}{\sqrt{2}}(E_1 - iE_2) \end{cases} \tag{3.44}$$

Therefore, the common components of the signal not due to interference between the beams (the DC components of the light intensity and the noise

introduced by the gain of the electronic devices) are eliminated in the amplifier. It has been shown that using balanced detection the SNR can be improved by a factor of 2 with respect to a system in which this method is not used, furthermore in a balanced configuration the value of the SNR cannot exceed a limit value, independent of the optical power reaching the detector [67]. This value is calculated for a system like the one shown in figure 3.5 is calculated below.

The optical power measured at the detector is the sum of the optical power measured at the outputs labelled as 3 and 4 in the figure:

$$P_m = P_3 + P_4 \tag{3.45}$$

P_3 and P_4 can be expressed as:

$$\begin{cases} P_3 = (1-\kappa)P_1 + \kappa P_2 \\ P_4 = \kappa P_1 + (1-\kappa)P_2 \end{cases} \tag{3.46}$$

Since the directional coupler, DC, is characterized by a transmission coefficient $\gamma = 0.5$. On the other hand, P_1 and P_2 can be expressed as:

$$\begin{cases} P_1 = O\psi(1-\chi)P \\ P_2 = (1-\chi)\dfrac{\epsilon}{\psi\chi}P \end{cases} \tag{3.47}$$

Finally, the OCT signal can be expressed in terms of the optical power as:

$$S = 2\theta^2 P_1 P_2 \tag{3.48}$$

where θ is the sensitivity of the detector. The current can be written as:

$$< i >= \theta P_m \tag{3.49}$$

and using the result from equation 3.43:

$$\frac{Sig}{No} = \frac{A \cdot P^2}{C + D \cdot P + E \cdot P^2} \tag{3.50}$$

where:

$$\begin{cases} A = & 2\theta^2 O(1-\chi)^2/\epsilon \\ & \text{(signal)} \\ C = & 4K_B T/R_L \\ & \text{(thermal noise)} \\ D = & 2eB\theta\left(O\psi + \dfrac{\epsilon}{\psi\chi}\right)(1-\chi) \\ & \text{(shot noise)} \\ E = & (1+\Pi^2)\dfrac{B}{\Delta\nu_{eff}}\theta^2\left(O\psi + \dfrac{\epsilon}{\chi}\right)^2(1-\chi)^2 \\ & \text{(excess photon noise)} \end{cases} \tag{3.51}$$

Therefore, the maximum value for the SNR that can be obtained for this system is;

$$\left(\frac{Sig}{No}\right) = \frac{\frac{2O\epsilon}{\chi}}{(1+\Pi^2)\frac{B}{\Delta\nu_{eff}}\left(O\psi + \frac{\epsilon}{\psi\chi}\right)^2} \tag{3.52}$$

3.7 Simultaneous *en-face* OCT and SLO systems

When the scanning method for *en-face* OCT was introduced in section 3.5, it was explained how the scanning method is very similar to that used in SLO. This similarity has made it possible to combine both techniques in just one system that is able to produce pairs of simultaneous *en-face* OCT and SLO

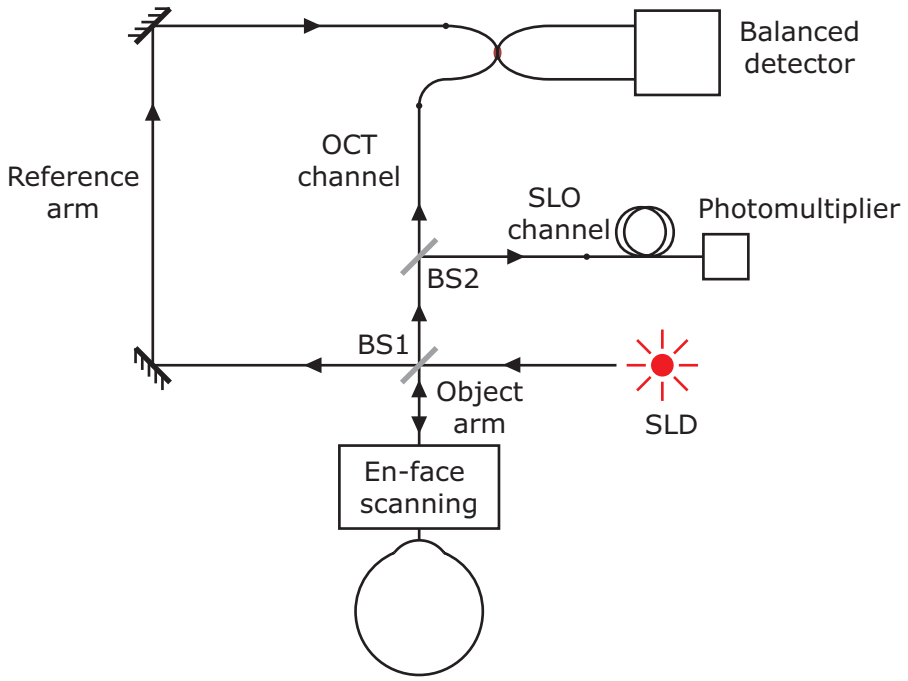

Figure 3.6: Sketch of a configuration valid for the implementation of simultaneous en-face *OCT/SLO system.*

images of the *in-vivo* human retina that show pixel to pixel correspondence [72]. This combination is based on an *en-face* OCT system that incorporates a beam splitter that sends part of the light scattered back from the back of the eye into the OCT channel. The rest is sent to a second detector, in this case a photomultiplier, that produces the signal needed to create the SLO image, as shown in figure 3.6.

Because the two images show pixel to pixel correspondence [73], the SLO image can be used to precisely guide the exploration in the OCT channel. Furthermore, specific orientation and location of B-scan slices can be guided by the information in the SLO image. It has been explained how OCT can produce *en-face* images with very high depth resolution. Previous results [74] have shown that the higher the depth resolution, the more fragmented

is the *en-face* OCT image. This effect often makes it difficult for a visual scientist or ophthalmologist to determine the exact spatial location of the retinal patch imaged. The SLO images obtained using the combined system, shows coarser depth resolution, and can help interpret the information of the fragmented OCT image. Furthermore, OCT images present high levels of speckle noise due to the interferometric nature of the technique. On the other hand, SLO images obtained using a broad band light source present very low levels of speckle noise, almost negligible. The performance of such combined instrument was evaluated on several pathology cases [69].

4

Wavefront Sensing in the Eye

Up to this point of this Thesis, it has been considered that the systems used to produce OCT and SLO images are aberration free, and therefore, the performance of such systems is diffraction limited. In the case of systems used for *in-vivo* human retinal imaging this assumption is not valid. The human eye is affected by optical aberrations; they have an effect on its performance and also on the quality of the images obtained using any technique where light propagates through the optics of the eye. In this chapter we explain the origin of these aberrations, and how they can be measured and characterized using different methods. In particular, the Shack-Hartmann wavefront sensor is introduced. In further chapters it is explained how the output of such wavefront sensor can be used to correct for ocular aberrations and thus improve the performance of any *in-vivo* retinal imaging technique.

4.1 Aberrations of the Eye

The performance of the human eye is affected by different types of aberrations that degrade its optical quality. The most commonly known of these aberra-

tions are defocus and astigmatism, but other aberrations such as chromatic aberration, and higher order monochromatic aberrations, e.g. spherical and coma-like aberrations [91], are also present in the eye.

There are several causes for these aberrations to appear. Misalignments in the optical surfaces of the eye or the decentered position of the pupil can be the cause for them to appear [13, 45], although it is thought that irregularities in the optical surfaces like the cornea [60, 11, 16] may produce the most important contribution to the aberrations of the eye. It may be worthwhile to emphasize at this point that this irregularities in the optical surfaces of the eye, and especially in the lens, are often matched to the aberration in the cornea and, as a result, the overall aberration of the eye is actually lower than the sum of the aberration introduced by each one of these surfaces on their own [11].

It is also known that the aberrations of the eye are not constant in time. Young eyes are usually less aberrated than older eyes and so aberrations change with age [61]. These changes are slow enough to be neglected in the process of *in-vivo* retinal imaging, since images of the retina are obtained in a time usually shorter than a second. However, ocular aberrations also change in a shorter timescale. Changes in the aberrations of the eye have been reported with frequencies from $1 - 2Hz$ up to $\sim 250Hz$. Several possible reasons have been suggested for this temporal variation of aberrations, for example heart beat [47, 42, 43] and accommodation [58, 45], although conclusions are not definitive. Another source for ocular aberration change is related to involuntary movements of the eye, known as saccades and microsaccades. These movements produce changes in pressure within the eye

due to the effect of contraction of the muscles that produce them. These movements cannot be avoided since they play an important role in vision. Saccades are slow movements of the eye, and their frequency is related to the amplitude of the movement itself. This movements improve the resolution of the image perceived by the subject: as the eye moves, the patch of the image that falls on the fovea changes. Since the fovea is the retinal part that presents the highest density of photoreceptors, the mental map can be built from high resolution patches as the eye moves around the scene. Microsaccades, also called tremour, play a different role in vision. They are very fast movements (60 Hz in frequency) with small amplitude (roughly 20 arcseconds). If they were not present, when staring fixed at a scene the vision would cease, since the photoreceptors respond to changes in luminance [52]. Finally, some reports have been presented studying the link between changes in ocular aberrations and fluctuations in the tear film [31, 41, 41, 41]. Again, the results are not conclusive.

However, it is unclear the range of frequencies of aberration fluctuation that can be neglected in terms of its effect in the quality of retinal images. Although it is agreed the main component of eye aberration fluctuates at frequencies of $\sim 1 - 2Hz$ [47], it is unclear if fluctuations beyond 40 Hz are negligible [47], or they have an impact in image quality to a value of up to $\sim 250Hz$ [26]. It is clear that fluctuating aberrations of the human eye affect the quality of retinal images.

Aberrations introduced in the eye by the causes mentioned above do not depend on the wavelength of light, and that is why sometimes they are referred to as monochromatic aberrations. But chromatic aberration is also present in

the eye [39, 59]. There are two different kinds of chromatic aberration present in the human eye. One is longitudinal chromatic aberration, in which the focal length of the optics of the eye depends on the wavelength considered. The second is lateral chromatic aberration, in which magnification is different depending on the wavelength. Research carried out in this area suggests that monochromatic aberrations play an important role in vision, since they reduce the impact chromatic aberration has in eye performance [62].

Aberrations in the human eye vary widely between subjects[56], and some efforts have been made in order to characterize them for a large population [76, 87].

It is not an easy task to determine the aberrations of the living eye. Traditionally, several techniques have been used to determine the amount of defocus or astigmatism in the eye. The most common is the trial of ophthalmic lenses. This is a subjective method as it depends on the perception of the subject, and therefore there are a series of parameters other than the aberrations of the eye that may influence the results, such as the neurological process of the optical information [10]. So it is interesting to be able to determine the aberrations of a the eye using a certain protocol in an objective way.

It is obvious that aberrations of the eye degrade the perception of the subject, since they degrade the image of the world formed in his retina. This is not the only problem that they present. Sometimes it is desirable to obtain images of the retina, for example, for medical diagnosis. In this case, the image of the retina needs to be obtained through the optics of the eye, and therefore its aberrations also lower the quality of these images. It would be a

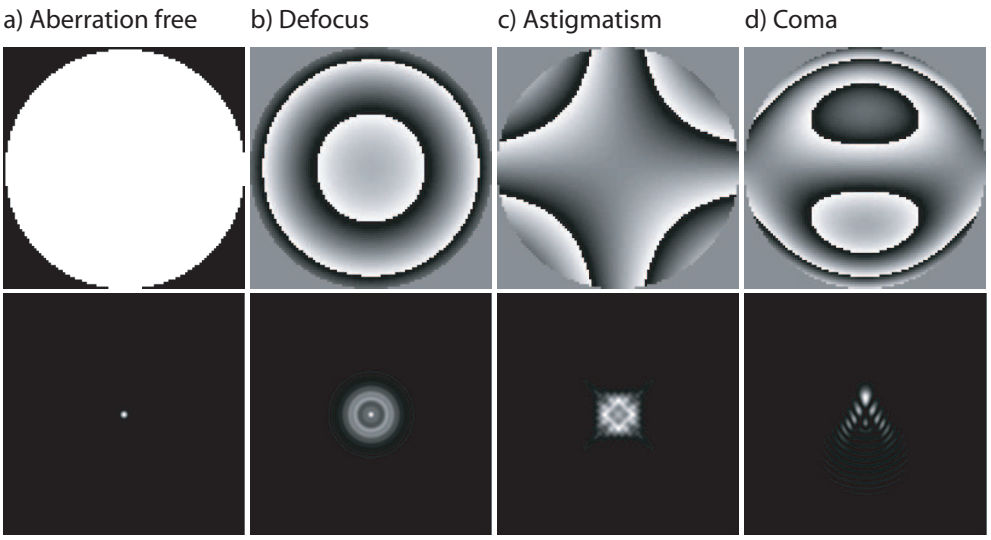

Figure 4.1: Aberration map and corresponding PSF for the following Zernike modes a) no aberration, b) Z_0^2, c) Z_{-2}^2, d) Z_{-1}^3

clear advantage to determine the aberrations of the eye of the patient, if they could be corrected. In further chapters it will explained how adaptive optics has been used to dynamically correct for ocular aberrations and improve the quality of retinal images obtained using several different techniques. In this chapter a technique widely used to determine the aberrations of the human eye is going to be presented: the Shack-Hartmann wavefront sensor.

4.2 Basic Concepts of Wavefront Sensing

The wavefront of a light beam is the continuous surface defined by the points in space in which the electric field of the light beam have the same phase. For a perfectly collimated beam, this wavefront is a plane perpendicular to the direction of propagation of the beam. The image of a point in an aberration free system is only limited by diffraction, and is called the diffraction

limited point spread function (PSF). If the system is aberrated, the shape of the wavefront of the beam will differ from this flat plane. The wavefront aberration can be then expressed as the distance along a direction parallel to the optical axis from the ideal non aberrated flat plane (reference plane) to the actual wavefront for each point of the pupil. The image of a point for an aberrated system will no longer be the diffraction limited PSF, but this function will broaden instead. Figure 4.1 shows different wavefront maps for aberrated and non-aberrated beams, and also the associated PSF's. A wavefront sensor should be able to determine the deviation of the beam from the reference plane. There are several techniques used to determine the shape of a wavefront. Some of them are based on interferometry, and they have been used for different applications, such as surface quality determination. Lateral shearing interferometry is one of the interferometric techniques used historically for wavefront sensing in adaptive optics. A shearing device is used to split the wavefront to be measured into two components. One of these components is shifted, so they are mutually displaced by a distance called shear. In order to determine the shape of the wavefront, the interference pattern in the overlap area is recorded, and the phase map of the wavefront can be determined [78]. Another method that is widely used in adaptive optics for astronomy is the curvature sensor [79]. In this technique a lens is used to focus the wavefront to be determined at a certain plane. The irradiance distribution is then recorded at two planes at a certain distance from this focal plane: one of them is slightly before and the other slightly behind. It can be shown in the geometrical optics approximation that the difference between the two plane irradiance distributions is a measurement

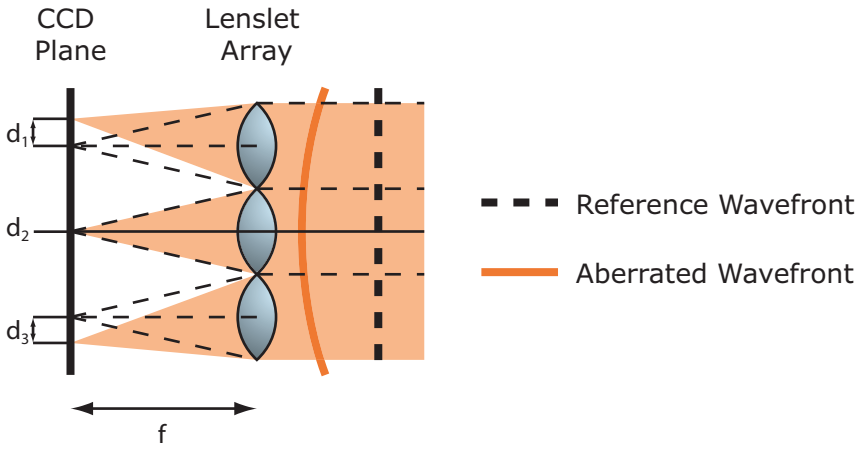

Figure 4.2: Lenslet Array

of the local wavefront curvature inside the beam and of the wavefront radial first derivative at the edge of the beam. Pyramid wavefront sensing is another technique that has been used in adaptive optics for astronomy and also for retinal imaging[50, 21]. In this technique the beam under study is focused on the tip of a glass pyramid. Each of the facets of the pyramid will deflect the beam in a different direction. Each of these beams is imaged, and the information related to the intensity difference between the beams is used to reconstruct the related wavefront.

However, in the case of wavefront sensing in the living human eye, the Shack-Hartmann wavefront sensor is the technique that has been most widely used. The technique is easy to implement at a very low cost.

4.2.1 Shack-Hartmann wavefront sensor

The Shack-Hartmann wavefront sensor [85] is basically formed by a lenslet array and a CCD placed at its focal plane, as shown in fig 4.2. The figure

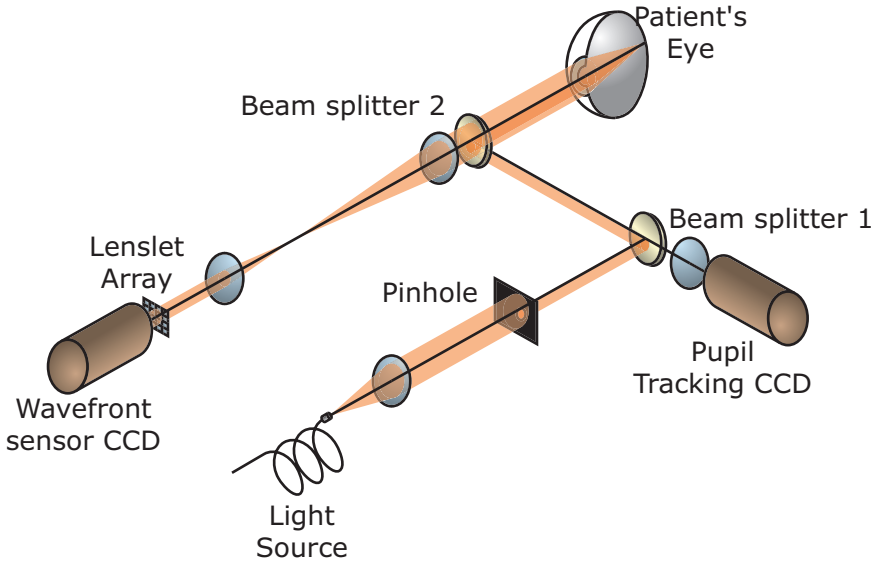

Figure 4.3: Implementation of a Shack-Hartmann wavefront sensor for eye aberration determination

shows how each of the lenslets creates a spot on the CCD, and the position of these spots will depend on the average tilt of the wavefront over the sub-aperture defined by the lenslet. The relationship between the average tilt of the wavefront, ϕ_i, over a certain lenslet area, i, and the spot displacement, d_i, is as follows

$$tan(\phi_i) \approx \phi_i \approx \frac{m_i}{f} \tag{4.1}$$

where f is focal length of the lenslet. So by determining the spot displacement for each of the lenslets of the array the local slopes of the wavefront can be determined, in order to reconstruct it.

Although the concept is quite simple, there are a series of considerations to take into account when applying this technique to determine the aberration of the human eye. First of all, the retina of the eye does not emit light, so

there is the need for an artificial way to illuminate the eye. This is in general done by sending a probing beam into the eye. Usually, laser beams are used, since they are easily collimated, and there are many options of wavelengths and powers available in the visible range. The illumination is made by means of a beam splitter (beam splitter 2 in fig. 4.3). Light from the source reflected from the beam splitter is sent into the eye, where it is focused at the retina. Light scattered back from the retina passes through the beam splitter, and is sent via some relay optics into the wavefront sensor. It should be noted that the light passes through the optics of the eye twice: on the way into the retina from the source, and back after being scattered from the back of the eye. In this case, the measurement obtained with the wavefront sensor may not be correct, since in this case the effect of odd aberrations may be lost, and only even aberrations may be measured. This is referred to as the double pass effect [14, 12, 66, 25]. In order to avoid the double pass effect, a very simple method has been developed. It is based in the fact that the performance of normal eyes can be considered as almost diffraction limited for pupil diameters of 1 mm or less. Using this characteristic, a pinhole can be used in order to make the diameter of the incoming beam small, and therefore when focusing on the retina it can be considered aberration free. In this case the beam is only distorted in the way out from the eye, and the double pass effect is avoided. Typically the pinhole can be placed slightly off axis in order to avoid reflections from the cornea reach the CCD of the wavefront sensor [48].

Once the pattern of spots created by the eye of the subject is obtained, it is compared to that created by a beam considered as reference. Usually this

beam is a parallel beam, and is created using a flat mirror in the position where the eye is placed. The displacement of the spots with respect to this reference spots pattern gives the information necessary to reconstruct the wavefront aberration as explained in section 4.4.

4.3 Zernike Polynomials

In general, the wavefront aberration will be a complicated surface. In order to simplify its description, a set of two dimensional functions that form a complete basis within the pupil area can be used. Using this basis, the wavefront can be written as [17]:

$$W(x,y) = \sum_{i=0}^{\infty} a_i \Phi_i(x,y) \tag{4.2}$$

where $\Phi_i(x,y)$ are a set of vectors that form a complete basis over the pupil of the system. Therefore, if $\Phi_i(x,y)$ are known, the set of values a_i determine the wavefront.

The base most commonly used in optics for wavefront aberration description is that formed by the Zernike polynomials. It is convenient to introduce them here to understand how they are used to reconstruct the wavefront aberration, which will be explained in following sections. It is important to note that there are many bases that can be used instead of the Zernike polynomials and the reconstruction of the wavefront should be as accurate. Traditionally, they have been preferred over other choices for a series of characteristics that make them appropriate for optics. First of all, Zernike polynomials form an orthonormal base over the unit circle pupil. This is a very convenient property in optics, since usually lenses are formed by surfaces with radial

symmetry. The Zernike polynomials are also related to optics because some of them are very closely related to aberrations commonly present in rotationally symmetric optical systems. For example, defocus is described by the Zernike term Z_2^0, astigmatism by terms Z_2^{-2} and Z_2^{+2}, coma like aberration is related to terms Z_3^{-1} and Z_3^{+1}, and spherical aberration is described by term Z_0^{+4}. The notation used here is detailed in the next section.

For these reasons, the Zernike polynomials are widely used in describing aberrations of optical systems in general, and in particular to describe the aberrations of the eye. They are so commonly used in the field of vision science that a standard way to report the aberrations of the eye has been developed that unifies the several forms of generating and normalize the Zernike polynomials [86].

4.3.1 Generation of the Zernike Polynomials

As already stated, the Zernike polynomials [17] are a set of two dimensional functions that are orthonormal for the interior of the unit circle. This property can be expressed as follows:

$$\int\int_{x^2+y^2\leq 1} Z_\alpha^*(x,y) Z_\beta(x,y) = \delta_{\alpha\beta} \tag{4.3}$$

Zernike polynomials are "invariant in form" with respect to rotations of axis about the origin, i.e., when a rotation is applied as follows:

$$\begin{aligned} x' &= x\cos\phi + y\sin\phi, \\ y' &= -x\sin\phi + y\cos\phi, \end{aligned} \tag{4.4}$$

the Zernike polynomial is transformed into

$$Z(x, y) = G(\phi)Z(x', y') \tag{4.5}$$

where $G(\phi)$ is a continuous function of period 2π of the angle of rotation, and $G(0) = 1$. The application of two successive rotations of angles ϕ_1 and ϕ_2 is equivalent to a single rotation of angle $\phi_1 + \phi 2$. Therefore:

$$G(\phi_1)G(\phi_2) = G(\phi_1 + \phi_2) \tag{4.6}$$

The general solution for $G(\phi)$ is well known, and is as follows:

$$G(\phi) = e^{il\phi} \tag{4.7}$$

where l is an integer number. Using this result:

$$Z(\rho\cos\phi, \rho\sin\phi) = R(\rho)e^{il\phi} \tag{4.8}$$

where $R(\rho) = Z(\rho, 0)$. If we assume Z is a polynomial of degree n in the variables x and y, from 4.8 it follows that $R(\rho)$ is a polynomial in ρ of degree n, and contains no power of ρ of degree lower than $|l|$. Moreover, $R(\rho)$ is an even or odd polynomial according as l is even or odd.

The set of Zernike polynomials contains a polynomial for each pair of the permissible values of n (degree) and l (angular dependence), i.e., for integral values of n and l, such that $n \geq 0$, $n \geq |l|$, and $n - l$ is even. This is denoted by:

$$Z_n^l(\rho\cos\phi, \rho\sin\phi) = R_n^l e^{il\phi} \tag{4.9}$$

An explicit derivation of the expressions of the radial polynomials of Zernike can be found here [17]. The expression of the radial part of the Zernike polynomials is as follows:

$$R_n^{\pm l} = N_n^{\pm l} \sum_{s=0}^{\frac{1}{2}(n-l)} (-1)^s \frac{(n-s)!}{s!\left(\frac{n+l}{2}-s\right)!\left(\frac{n-l}{2}-s\right)!} \rho^{n-2s} \tag{4.10}$$

where $N_n^{\pm l}$ is a normalization factor for the radial component of the Zernike polynomials. There are several different options to choose this factor. In the work presented here the normalization of the Zernike polynomials has been chosen so that:

$$R_n^{\pm l}(1) = 1 \tag{4.11}$$

and therefore:

$$N_n^l = \sqrt{\frac{2(n+1)}{1+\delta_{l,0}}} \tag{4.12}$$

where $\delta_{l,0}$ is the Kronecker delta function, which is 0 for $l \neq 0$ and 1 for $l = 0$.

4.3.2 Wavefront RMS

The wavefront RMS is a quantity that relates to the similarity of the measured wavefront to the reference, in this case a flat wavefront. It is the root mean square (RMS) of the wavefront aberration, or equivalently, the RMS of the distance from the measured wavefront to the reference, in a direction parallel to the optical axis over the pupil area. It is expressed as:

$$RMS^2 = \int_{Pupil} (W(x,y) - W_0(x,y))^2 \mathrm{d}x\mathrm{d}y \tag{4.13}$$

where $W_0(x, y)$ is the wavefront used as the origin for the calculation of the RMS. Generally this wavefront is a planar wavefront equal to zero, and therefore it can be ignored in the equation. But sometimes, it is convenient to consider other situations, e.g. it may be interesting to calculate the wavefront aberration without considering tilt, because tilt does not distort the resulting image, it only introduces a displacement. In other situations, only high order aberrations are considered, and in that case it may be important to subtract defocus and astigmatism too.

If the reference is considered to be constant and equal to zero, and the wavefront aberration is determined by means of a Zernike polynomials decomposition, then the previous expression results in:

$$RMS^2 = \int_{Pupil} (\sum_{i=0}^{\infty} a_i Z_i(x, y))^2 \mathrm{d}x\mathrm{d}y \tag{4.14}$$

The base formed by the Zernike polynomials is chosen so that its elements are orthonormal, then the previous expression becomes:

$$RMS^2 = \sum_{i=0}^{\infty} a_i^2 \tag{4.15}$$

This result is very commonly used to give a parameter related to the optical quality of the optical system considered, and particularly to the optical quality of the eye that is being studied, because the lower the RMS, the closer is the measured wavefront to a flat wavefront, and therefore the better its optical quality.

4.3.3 Strehl Ratio

The Strehl ratio is another quantity that gives information about the flatness of the wavefront, and therefore the quality of the optical system being evaluated. It is the ratio between the peak intensity of the aberrated PSF of the system to the peak intensity of the aberration free PSF. An approximation of the Strehl ratio, st, that is valid for low aberrated wavefronts is given by:

$$st \simeq e^{-(2\pi\iota)^2} \tag{4.16}$$

where ι is the wavefront RMS given in waves. Usually a system is considered to be aberration free when the Strehl ratio is greater than 0.8. This corresponds to an $RMS < 0.7$, where the RMS is expressed in waves, or equivalently $\lambda/14$. This is referred to as the Maréchal criterion [17].

4.4 Wavefront Aberration Determination

In order to reconstruct a wavefront the spots displacements in the CCD need to be translated into the components in which the wavefront is decomposed in the chosen basis. In order to do so a matrix is built that links the spots displacements to the wavefront decomposition. This matrix would be of the form:

$$\begin{bmatrix} a_1^{-1} \\ a_1^{+1} \\ a_2^{-2} \\ \vdots \\ a_n^l \end{bmatrix} = \begin{bmatrix} c_{1,1} & c_{1,2} & \cdots & c_{1,2l} \\ c_{2,1} & c_{2,2} & & c_{2,2l} \\ \vdots & & & \vdots \\ c_{n,1} & c_{n,2} & \cdots & c_{n,2l} \end{bmatrix} \begin{bmatrix} m_{x,1} \\ m_{x,2} \\ \vdots \\ m_{x,l} \\ m_{y,1} \\ m_{y,2} \\ \vdots \\ m_{y,l} \end{bmatrix} \tag{4.17}$$

where a_n^l, the elements of vector $\mathbf{A}$, are the Zernike components that describe the wavefront aberration, $m_{x,i}$ and $m_{y,i}$, which form the vector $\mathbf{M}$, are the spots displacements in the x and y directions for the ith lenslet, $c_{i,j}$ are the elements of matrix $\mathbf{C}$ that needs to be determined.

After this set of equations has been solved, the wavefront aberration, $W(x, y)$, can be determined as:

$$W(x, y) = \sum_{n,l} a_n^l Z_n^l(x, y) \tag{4.18}$$

For simplicity and clarity, from now on the Zernike polynomials will be numbered with only one subindex n, that can be easily translated into the standard notation of two subindexes (n, l).

It is not easy to determine what the components of the matrix $\mathbf{C}$ are, because it is not known how a certain spots pattern is related to the decomposition of the wavefront aberration into Zernike polynomials, in fact this is the problem to be solved. On the other hand, the displacement of the spots for a certain

Zernike component can be determined, as it is explained below. Consider the following equation, which is the inverse of equation 4.17:

$$\mathbf{M} = \mathbf{C}^{\dagger}\mathbf{A} \tag{4.19}$$

Assume the aberration of the wavefront matches the shape of the first Zernike mode. The displacement of each of the spots in the CCD will be related to the average slope of the Zernike component over the area of the lenslet. Since the analytical expression of the jth Zernike component is known, its average slope over the ith lenslet area can be determined using the following expression:

$$m_{x,i} = \int_{lenslet} \frac{\partial Z_j(x,y)}{\partial x} \mathrm{d}s \tag{4.20}$$

Using this expression, the matrix $\mathbf{C}^{\dagger}$ can be determined, and equation 4.19 can be written as:

$$\begin{bmatrix} m_{x,1} \\ m_{x,2} \\ \vdots \\ m_{x,l} \\ m_{y,1} \\ m_{y,2} \\ \vdots \\ m_{y,l} \end{bmatrix} = \begin{bmatrix} \int_1 \frac{\partial Z_l(x,y)}{\partial x}\mathrm{d}s & \int_1 \frac{\partial Z_2(x,y)}{\partial x}\mathrm{d}s & \cdots & \int_1 \frac{\partial Z_n(x,y)}{\partial x}\mathrm{d}s \\ \int_2 \frac{\partial Z_l(x,y)}{\partial x}\mathrm{d}s & \int_2 \frac{\partial Z_2(x,y)}{\partial x}\mathrm{d}s & \cdots & \int_2 \frac{\partial Z_n(x,y)}{\partial x}\mathrm{d}s \\ \vdots & \vdots & \ddots & \vdots \\ \int_l \frac{\partial Z_l(x,y)}{\partial x}\mathrm{d}s & \int_l \frac{\partial Z_2(x,y)}{\partial x}\mathrm{d}s & \cdots & \int_l \frac{\partial Z_n(x,y)}{\partial x}\mathrm{d}s \\ \int_1 \frac{\partial Z_l(x,y)}{\partial y}\mathrm{d}s & \int_1 \frac{\partial Z_2(x,y)}{\partial y}\mathrm{d}s & \cdots & \int_1 \frac{\partial Z_n(x,y)}{\partial y}\mathrm{d}s \\ \int_2 \frac{\partial Z_l(x,y)}{\partial y}\mathrm{d}s & \int_2 \frac{\partial Z_2(x,y)}{\partial y}\mathrm{d}s & \cdots & \int_2 \frac{\partial Z_n(x,y)}{\partial y}\mathrm{d}s \\ \vdots & \vdots & \ddots & \vdots \\ \int_l \frac{\partial Z_l(x,y)}{\partial y}\mathrm{d}s & \int_l \frac{\partial Z_2(x,y)}{\partial y}\mathrm{d}s & \cdots & \int_l \frac{\partial Z_n(x,y)}{\partial y}\mathrm{d}s \end{bmatrix} \begin{bmatrix} A_1 \\ A_2 \\ \vdots \\ A_n \end{bmatrix} \tag{4.21}$$

Once the inverse matrix $\mathbf{C}^{\dagger}$ has been determined, it can be inverted to deter-

mine $\mathbf{C}$. Since the matrix $\mathbf{C}^{\dagger}$ is not square in general (it is overdetermined, since the number of lenslets is larger that the number of Zernike polynomials used in the reconstruction), its inverse is not uniquely defined, and only the pseudo-inverse of the matrix may be calculated. In order to calculate the pseudoinverse of the matrix, the singular value decomposition (SVD) of the matrix is used as described in the following section.

4.4.1 Singular value decomposition (SVD)

The singular value decomposition is a tool that allows the decomposition of any $m \times n$ matrix where $m > n$ into the product of three matrices: an $m \times n$ column-orthogonal matrix $\mathbf{U}$, an $n \times n$ diagonal matrix $\mathbf{W}$ with positive or zero elements, or *singular values*, and the transpose of an $n \times n$ orthogonal matrix $\mathbf{V}$. The decomposition of any matrix can be then expressed as:

$$\mathbf{A} = \mathbf{U} \cdot \mathbf{W} \cdot \mathbf{V}^T \tag{4.22}$$

The matrices $\mathbf{U}$ and $\mathbf{V}$ are orthogonal in the sense that their columns are orthonormal:

$$\begin{cases} \sum_i = U_{ik}U_{il} = \quad \delta_{kn}; 1 \leq k \leq n; 1 \leq l \leq n \\ \sum_j = V_{jk}V_{jl} = \quad \delta_{kn}; 1 \leq k \leq n; 1 \leq l \leq n \end{cases} \tag{4.23}$$

or equivalently

$$\mathbf{U}^T \cdot \mathbf{U} = \mathbf{V}^T \cdot \mathbf{V} = \mathbf{I} \tag{4.24}$$

where $\mathbf{I}$ is the identity matrix. Matrix $\mathbf{V}$ is related to the Zernike polynomials

coefficients in terms of spots displacements, while matrix **U** is related to the spots pattern.

There are a series of computational routines available that can perform the SVD decomposition of a matrix. In the case of the work presented in this Thesis, the routine used is the one provided by "Numerical Recipes in C++" [77].

4.5 Determining the Position of the Spots

Up to this point, it has been discussed how to determine the wavefront aberration from the displacement of the spots recorded using the CCD camera in the wavefront sensor. However, the spots position determination in the pattern obtained using the CCD is not a trivial task. Furthermore, there are a series of factors, such as speckle or the readout noise in the CCD, that play a role in the measurement and need to be taken into account. There are several methods that can be used to determine the position of the spots in the CCD frame. In this section two of these methods are described: finding the center of "mass" of the spot, and fitting the spot profile to a certain function, in this case a gaussian profile.

4.5.1 Center of "Mass"

In this method for centroid determination the grey levels of each pixel within the lenslet area are used in a similar way to the mass when determining the center of mass of a certain body, as follows:

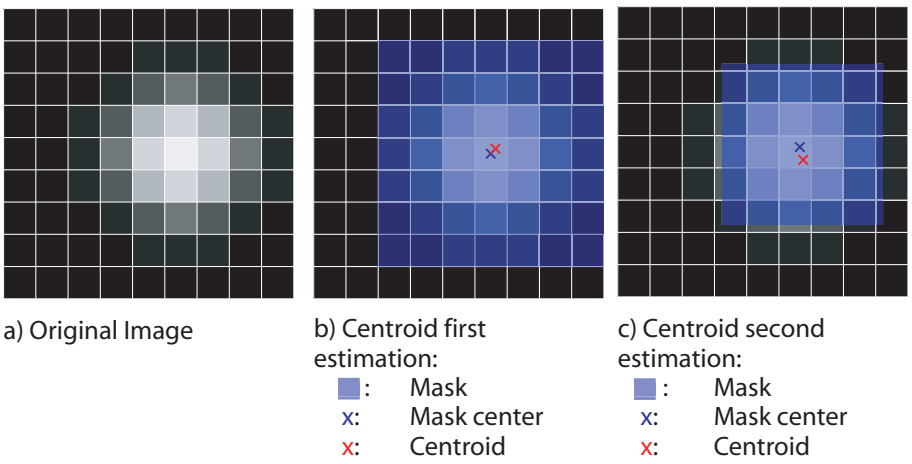

Figure 4.4: Diagram of the evolution of the mask on the centroid determination

$$C_l(x,y) = \frac{\sum_{l;i,j} g_{i,j} r_{i,j}(x,y)}{\sum_{i,j} g_{i,j}} \tag{4.25}$$

where $C_l(x,y)$ is the resulting centroid value for lenslet l, $g_{i,j}$ is the grey level for pixel (i,j), and $r_{i,j}(x,y)$ is the distance from the reference point to the center of the (i,j) pixel.

To calculate the centroid position using this method, a reference point has to be determined. In our case, this reference point is the center of a square mask that is used to reduce the influence of pixels that are far away from the centroid of the spot, and only contribute to this calculation with noise. To reduce the effect of such pixels, the calculation is repeated a few times, using the result of the previous estimation as the reference point (and thus the center of the mask) of the following one. The size of the mask is reduced in every calculation, minimizing the effect of dark and hot pixels or light scattered from the different surfaces and media in the eye, and therefore minimizing noise effects.

Fig. 4.4 shows the evolution of the mask in two different iterations of the algorithm used for centroid determination. In the first attempt, the reference point used is the center of the pixel with the highest grey value within the lenslet area, and the square mask is centered on that point (blue cross in fig. 4.4.b). Note that the result of the centroid algorithm is in general a real number, not an integer. Therefore, the boundary of the mask may not coincide with the edge of the pixels. A new parameter, $w(i,j)$, is introduced that is related to the overlap area between the mask and the pixel. This parameter can take any value from 0, if the pixel is completely outside the mask, to 1, when the whole pixel area is inside the mask. The modified centroid algorithm can then be written as:

$$C(x,y) = \frac{\sum_{i,j} w(i,j) g_{i,j} r_{i,j}(x,y)}{\sum_{i,j} w(i,j) g_{i,j}} \tag{4.26}$$

A second estimation of the centroid is obtained using 4.26. This result may be used as the reference point for a third iteration, using a new smaller mask, centered on this point to repeat the process. This procedure is repeated a number of times, that depends on the accuracy desired.

Other methods have been developed that do not need different iterations changing the size of the mask applied to calculate the centroid position. These methods calculate a threshold value for the grey level in the pixels of the lenslets[9, 8]. Pixels with a grey value below this threshold value are not considered for estimation of the centroid of the lenslet.

Other kinds of weights, $w(i,j)$, can be used in the centroid determination different than the overlap factor between the mask and the pixel area. Sometimes these weights are related to the distance to the reference pixel itself

(the closest to the reference point, the more importance has that pixel in the algorithm). The problem with this method is that the reference point has to be then a good estimation of the centroid itself.

The center of mass determination is very commonly used in Shack-Hartmann wavefront sensing because it involves simple calculations, and therefore it is fast in terms of computing time. However, it is difficult to determine the accuracy of the determination on the moment of calculation. It needs to be determined *a priori* to set the number of iterations needed to reach the expected accuracy.

The determination of the accuracy of the centroid position using the center of mass criterion is made by repeating the measurement of spots position several times for a non changing pattern, smoothing the effect of random noise produced by readout and photon noise. In order to avoid the effect of hot pixels in the CCD the background is recorded, and subtracted from the grey level values from each CCD frame. The number of iterations and the size of the masks used in each of the iterations can be optimized in order to maximize the accuracy with minimum calculation time.

4.5.2 Fit to Gaussian

Another method for centroid estimation is presented in this section, in which the accuracy can be changed as a parameter of the algorithm at the moment of calculation of the centroid position, and not beforehand as in the previous method. The Gaussian fit method assumes that the shape of each spot in the CCD corresponds approximately to a two dimensional Gaussian shape described by:

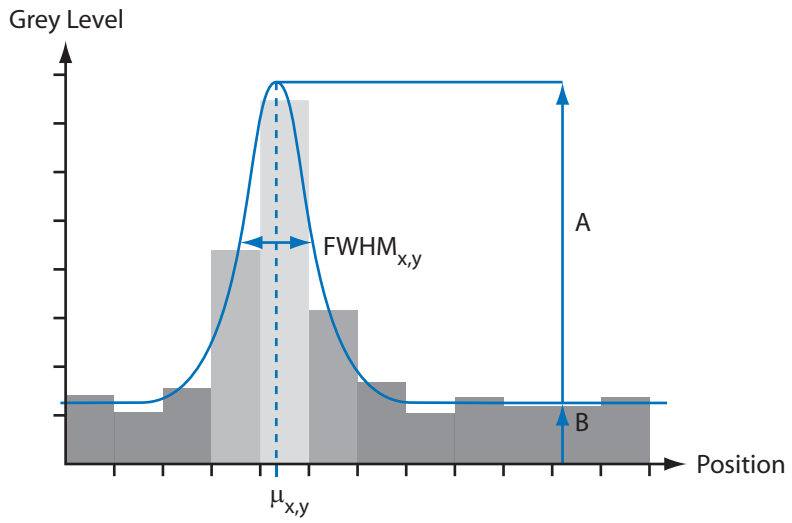

Figure 4.5: Diagram showing the different parameters to be fitted to a Gaussian function in order to determine the centroid position. Although the diagram shows the fit in only one dimension, it can be easily extended to two dimensions.

$$GF(x,y) = B + A\left(\frac{1}{2\pi\sigma_x\sigma_y}\right) e^{-\left[\frac{(x-\mu_x)^2}{2\sigma_x^2}+\frac{(y-\mu_y)^2}{2\sigma_y^2}\right]} \tag{4.27}$$

where B is related to the background noise, A is related to the amplitude of the function, σ_x and σ_y are related to the full width at half maximum in the x and y direction respectively, and μ_x and μ_y are the x and y positions where the Gaussian function is centered, i.e., the centroid position. A diagram where all these parameters are present is shown in fig. 4.5

The algorithm used in order to fit a Gaussian function to the grey level profile of the spots in the CCD consists on an iterative process in which the error or difference between the Gaussian function at the positions placed at the center of the pixels and the grey level of the corresponding pixel is minimized. The error function is defined as:

$$E_k = \Sigma_{i,j} \left(GF(x_i, y_j)_{i,j} - g_{i,j} \right)^2 \tag{4.28}$$

where k is the kth spot of the spot pattern, i, j designates the pixel within the lenslet area in the CCD, and x_i and y_j are the coordinates of the center of the i, j pixel. Since $G(x_i, y_j)$ depends on the parameters A, B, σ_x , σ_y, μ_x and μ_y, the appropriate values for these parameters that minimize ϵ_k need to be found. To do so, an iterative algorithm such as simplex [77], can be used in order to find those values.

The main drawback of this method is that it is time consuming: there are a number of iterations performed in order to determine the final estimation of each centroid. This time depends on the desired accuracy of the result and the number of pixels contained in each lenslet area. Therefore, this method of centroid determination is not suitable to determine the wavefront aberration in real time. However, it is suitable to determine the wavefront aberration a posteriori, i.e., the information of the CCD can be stored for each frame, and once the measurement has finished, the necessary data processing can be done in order to determine the wavefront aberration for each of the frames.

4.5.3 Fourier Transform Method

In order to determine the shape of the wavefront associated to a certain spot pattern, not only the centroid positions of the measurement frame have to be determined, but also those for the reference frame. The measurement in this case needs to be specially accurate, since any error that may exist would affect all of the measurements performed. Furthermore, the positions of the spots in the reference pattern may be used as a starting point for measurement

frames spot centroid determination. In the case of the reference pattern, it is not necessary to have a fast calculation, since it can be taken once before the measurement and used for different sets of measurements if the system does not change between them. Usually some information related to the geometry of the lenslet array and known *a priori* is used to determine the spots position in the reference pattern. This helps to create a relationship between the pixels grid in the CCD and the center of the lenslets in the array. In the work presented here a Fourier transform method was used to determine the position of the spots in the reference pattern. This method is based on the work from Dr. Carl Patterson (Imperial College, private communication).

Consider the lattice of spots in the reference beam. It has already explained in the previous sections how the centroid of each spot can be determined. In the case of the center of mass method, the position of the spots can be expressed as:

$$\langle r \rangle = \frac{\int\int I(r) r d^2 r}{\int\int I(r) d^2 r} \tag{4.29}$$

The square error for a given estimate of the position of the spot, r_0 is:

$$\delta r^2 = |\langle r \rangle - r_0|^2 = \frac{|\int\int I(r)(r - r_0) d^2 r^2|}{|\int\int I(r) d^2 r^2|} \tag{4.30}$$

Consider the function:

$$\begin{aligned} X &= \frac{|\int\int I(r)(r - r_0) d^2 r^2|}{|\int\int I(r) d^2 r^2|} && (4.31) \\ &= \langle r^2 \rangle - 2 r_0 \langle r \rangle + r_0^2 && (4.32) \\ &= [\langle r^2 \rangle - \langle r \rangle^2] + [\langle r \rangle - r_0]^2 && (4.33) \end{aligned}$$

$\langle r \rangle$ is the centroid, $[\langle r^2 \rangle - \langle r \rangle^2]$ is the second moment about $\langle r \rangle$. Therefore:

$$X = |r_0 - \langle r \rangle|^2 + const. = \delta r^2 + const. \tag{4.34}$$

Now, consider the function:

$$F(r) = f_1(r) + f_2(r) \tag{4.35}$$

where:

$$f_1(r) = 0.5[1 - cos(k_1 r + \varphi_1)] \tag{4.36}$$

$$f_2(r) = 0.5[1 - cos(k_2 r + \varphi_2)] \tag{4.37}$$

In the case in which $(k_1 r_0 + \varphi_1) \approx 2\pi n$ and $(k_2 r_0 + \varphi_2) \approx 2\pi m$ then:

$$F(r) \approx 0.25(k_1(r - r_0))^2 + 0.25(k_2(r - r_0))^2 \tag{4.38}$$

If a linear warp is applied o the field such that $k_1 k2 = 0$ and $|k_1| = |k_2|$, then $F(r)$ is proportional to $(r - r_0)^2$. So:

$$C = \int\int I(r)F(r)d^2r \tag{4.39}$$

where $I(r)$ is the intensity of the image of the array of spots. C is a weighted sum of the square errors of the spot intensity centroids from the lattice points defined by $F(r) = 0$ in the warped space. Minimizing C the parameters of $F(r)$ will find an approximate weighted least-squares best-fit lattice for the array of sensor spots. To do this, note that:

$$C = \tilde{F}(k) \otimes \tilde{I}(k)|_{k=0} \tag{4.40}$$

where $\tilde{A}$ denotes the Fourier transform of A, and

$$\tilde{F}(k) = \tilde{f}_1 + \tilde{f}_2 \tag{4.41}$$

$$\tilde{f}_1(k) = 0.5\{\delta(0) - 0.5\left[e^{i\delta_1}\delta(k_1) + e^{-i\delta_1}\delta(-k_1)\right]\} \tag{4.42}$$

$$\tilde{f}_2(k) = 0.5\{\delta(0) - 0.5\left[e^{i\delta_2}\delta(k_2) + e^{-i\delta_2}\delta(-k_2)\right]\} \tag{4.43}$$

Therefore:

$$C = \tilde{I}(0) - 0.5\left[e^{i\delta_1}\tilde{I}(-k_1) + e^{-i\delta_1}\tilde{I}(k_1) + e^{i\delta_2}\tilde{I}(-k_2) + e^{-i\delta_2}\tilde{I}(k_2)\right] \tag{4.44}$$

but, $\tilde{I}(-k) = \tilde{I}^*(k)$, which means

$$C = \tilde{I}(0) - \Re\left[e^{-i\delta_1}\tilde{I}(k_1) + e^{-i\delta_2}\tilde{I}(k_2)\right] \tag{4.45}$$

Thus the problem is reduced to finding the two largest peaks (non-DC) in one half of the Fourier transform of $I(r)$, which will be k_1 and k_2, and setting δ_1 and δ_2 such that $e^{-i\delta_1}\tilde{I}(k_1)$ and $e^{-i\delta_2}\tilde{I}(k_2)$ are both positive and real.
The points in a two dimensional lattice with lattice base vectors e_1 and e_2 are given by:

$$r_{mn} = \mathbf{E}\begin{pmatrix} m \\ n \end{pmatrix} + r_0 \tag{4.46}$$

where

$$\mathbf{E} = \begin{pmatrix} e_{1x} & e_{2x} \\ e_{1y} & e_{2y} \end{pmatrix} \tag{4.47}$$

If the lattice points are defined by:

$$F(r) = f_1(r) + f_2(r) = 0 \tag{4.48}$$

$$f_1(r) = 0.5[1 - cos(k_1 r + \varphi_1)] \tag{4.49}$$

$$f_2(r) = 0.5[1 - cos(k_2 r + \varphi_2)] \tag{4.50}$$

then:

$$k_1 r_{mn} + \varphi_1 = 2\pi m \tag{4.51}$$

$$k_2 r_{mn} + \varphi_2 = 2\pi n \tag{4.52}$$

Equations 4.51 and 4.52 can be written as:

$$\begin{pmatrix} k_{1x} & k_{1y} \\ k_{2x} & k_{2y} \end{pmatrix} \begin{pmatrix} x_{mn} \\ ymn \end{pmatrix} = \begin{pmatrix} \varphi_1 \\ \varphi_2 \end{pmatrix} = 2\pi \begin{pmatrix} m \\ n \end{pmatrix} \tag{4.53}$$

Defining:

$$\mathbf{K} = \begin{pmatrix} k_{1x} & k_{2x} \\ k_{1y} & k_{2y} \end{pmatrix} \tag{4.54}$$

then eq. 4.54

$$\mathbf{K}^T \mathbf{E} \begin{pmatrix} m \\ n \end{pmatrix} + K^T r_0 = 2\pi \begin{pmatrix} m \\ n \end{pmatrix} - \begin{pmatrix} \varphi_1 \\ \varphi_2 \end{pmatrix} \tag{4.55}$$

for all m ad n, where K^T is the transpose of K. This gives:

$$\mathbf{E} = 2\pi(\mathbf{K}^T)^{-1} \tag{4.56}$$

and

$$r_0 = -(\mathbf{K}^T)^{-1}\varphi = -(1/2\pi)\mathbf{E}\varphi \tag{4.57}$$

and the inverse:

$$\mathbf{K} = 2\pi(\mathbf{E}^{-1})^T \tag{4.58}$$

and

$$\varphi = -\mathbf{K}^T r_0 = -2\pi\mathbf{E}^{-1}(r - r_0) \tag{4.59}$$

Thus to get the lattice coordinates for a point, the following expression can be used:

$$r = \mathbf{E}\begin{pmatrix} n \\ m \end{pmatrix} + r_0 \Longrightarrow \begin{pmatrix} n \\ m \end{pmatrix} = \mathbf{E}^{-1}(r - r_0) \tag{4.60}$$

4.6 Implementation of a Shack-Hartmann wavefront sensor

As a first step to achieve an adaptive optics system to correct for aberrations of the human eye, we have implemented a Shack-Hartmann wavefront sensor as described in this chapter. The system was based on a single pass configuration, where the pupil of the incoming beam was smaller than the pupil of the outgoing one [12]. Figure 4.6.a shows a picture of the set-up used for aberration determination in the human eye, which is based on the sketch shown in fig. 4.3.

The incoming beam in the wavefront sensor had a pupil size of $1mm$, and it was parallel to the optic axis of the system, but it was decentered $2mm$. In

this way, reflections of the cornea reaching the detector were avoided [47, 48]. The pupil size of the outgoing beam was $6mm$. The light scattered back from the subject's retina was collected using a $2:1$ telescope, that sent the light to the lenslet array where the spots pattern was recorded in the CCD camera. The CCD camera used was a LCL-902C from Watec America Corp., which showed a quantum efficiency of 0.2 at $\lambda = 780$. The light source used was a pigtailed laser source from Thorlabs, with $\lambda = 780nm$. The optical power reaching the cornea of the subject is $\sim 5\mu W$, which is ~ 20 times lower than the maximum permissible exposure determined by the European Standards for Safety of Laser Products [6] for a configuration similar to the one presented here. The system used a B/W CCD 2005XA camera from RF Concepts for pupil tracking. These are cheap cameras for surveillance and they have very high sensitivity in the near IR. We used a Welch Allyn lenslet array, with square lenslets of $200\mu m$ pitch and $7.5mm$ focal length.

The system was able to show the evolution of the reconstructed wavefront aberration in real time at a frame rate of $4s^{-1}$, although it could reach video frame rate limited by the camera if the reconstruction procedure was performed after the measurements of the aberrated wavefront spot patterns were recorded.

Fig. 4.6.b shows a reconstruction for subject DM's left eye using the wavefront sensor built, and 4.6.c shows the same reconstruction using a commercially available Zywave wavefront sensor from Bausch and Lomb. It can be seen how both reconstructions are very similar both in shape, and in range of aberration, supporting the validity of the method used.

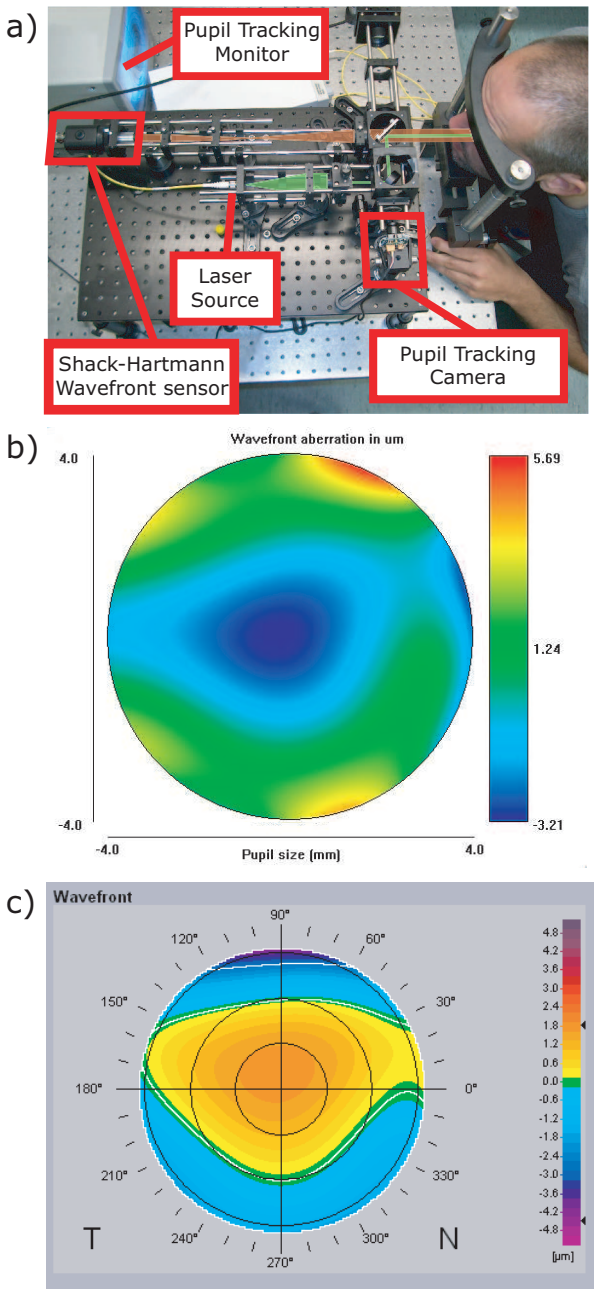

Figure 4.6: a) Picture of the wavefront sensor set-up built. b) Wavefront aberration reconstruction for subject DM using the wavefront sensor built. c) Wavefront reconstruction for subject DM using a commercially available Zywave wavefront sensor from Bausch and Lomb.

5

Adaptive Optics

Adaptive optics is a technique that was developed to improve the quality of images obtained by ground based telescopes. The quality of the images obtained using them is worsened by the distortion introduced in the wavefront by atmospheric turbulence. The technique allows their performance to be comparable to that obtained by telescopes placed outside the Earth's atmosphere which is close to diffraction limit. Since its invention, adaptive optics has been used for several different applications. One of the fields in which adaptive optics has become truly revolutionary is in retinal imaging [83]. When the aberrations of the eye are corrected using adaptive optics, the quality of the retinal images obtained is improved [56, 82], leading to the development of new diagnosis techniques.

In this chapter adaptive optics is introduced in order to understand how it can be used together with *en-face* OCT and SLO.

5.1 Introduction

Astronomical objects are very distant to Earth, and the light they emit can be considered to come from infinity. Since the space is mainly vacuum, the wavefront related to light coming from these objects can be considered as a plane. However, during the propagation of this light through the atmosphere the shape of the wavefront is changed due to atmospheric turbulence, caused by fluctuations in the refractive index of the different layers of the atmosphere. Atmospheric turbulence introduces phase delays in the light wavefront that are very complicated to predict or even describe. However, Kolmogorov's model describes to a certain extent the behavior of atmospheric turbulence using a series of parameters [53, 98]. As a result of the aberration introduced, the image of a point is no longer the characteristic point spread function of the system, but it is broadened instead as explained in the previous chapter. Therefore, the performance of ground-based telescopes is limited by atmospheric turbulence, and not by diffraction.

Adaptive optics was first suggested by Babcock *et al.* in 1953 [15] as a possible solution to this problem. However it was not successfully implemented until 1977 by Hardy *et al.* [44]. The technique consists on determining the aberration of the wavefront of the beam that forms the image of the astronomical object, and then correct for it using a wavefront correcting device, as shown in fig. 5.1. The determination of the wavefront aberration is performed by means of a wavefront sensor, that sends this information to a control device, usually a computer. The control computer then performs the processing of the data in order to determine the signal to be sent to the wavefront corrector (usually a deformable mirror) to correct for the wavefront

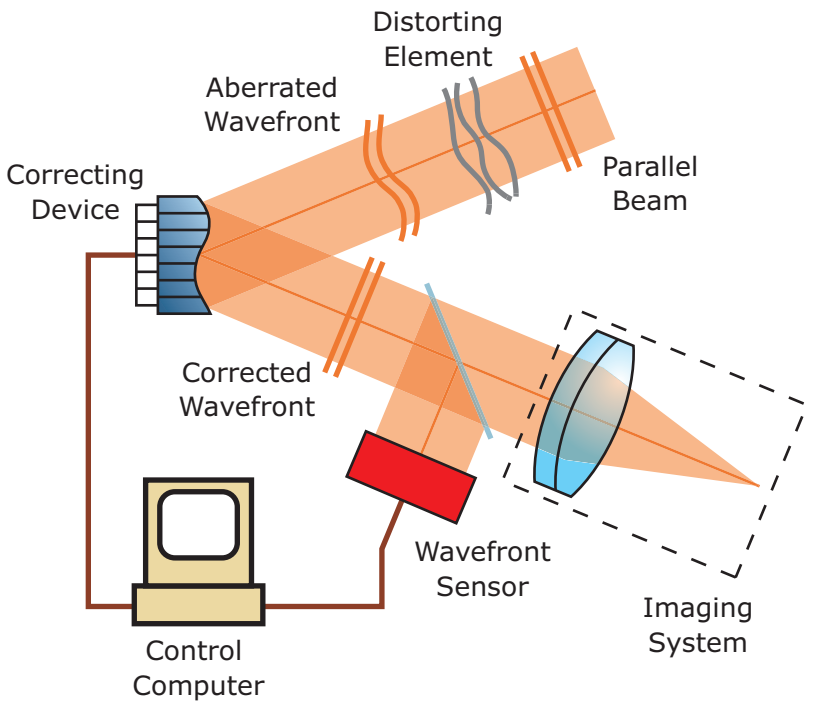

Figure 5.1: Adaptive Optics System

aberration. The process is repeated in a closed-loop, since the atmospheric turbulence changes in time, and the correction is only valid for a certain period of time.

In the case of retinal imaging, the element that introduces the aberration into the wavefront that reaches the imaging system is the subject's eye, as already mentioned in section 4.1. As in the case of atmospheric turbulence, the perturbation is not constant in time, thus adaptive optics is a suitable technique in order to correct for it.

Adaptive optics has been used in several areas of vision science, mainly in *in-vivo* retinal imaging. The first retinal imaging device that incorporated adaptive optics is a fundus camera developed by Liang *et al.* [57]. The system was able to produce images of the retina that showed unprecedented

resolution.

Since then other techniques used in the field have been improved by means of adaptive optics, such is the case of scanning laser ophthalmoscope [82], and optical coherence tomography systems [46, 103, 102]. These and other applications of AO in vision science are detailed in sec. 6.1.

But not only retinal imaging has benefited from adaptive optics. Since the technique was developed and proved to correct the aberrations of the eye, the concept of supernormal vision or super-vision appeared. It is related to the study of the eye perception when aberrations are eliminated. The resolution of the eye in this situation is comparable to the size of the photoreceptors, and the improvement in contrast sensitivity is studied under this condition [57, 95, 94, 100]. Also, a series of experiments related to psycho-physics have been possible thanks to adaptive optics, studying the perception of the outside world related to the neural processing of the optical information when changes in the aberrations of the subject are introduced [10, 94].

5.2 Elements of an adaptive optics system

The main elements of an adaptive optics system are a wavefront sensor, a control system and a wavefront corrector. In this section the last two are going to be described, since the wavefront sensor has already been described in chapter 4.

5.2.1 Wavefront correction

There are several different types of wavefront correctors that can be used in an adaptive optics system. They can be classified by several different characteristics [88, 89, 78]. Some of the most common kinds of correcting devices are going to be briefly described in this section.

A first possible classification of wavefront correctors divides them into those using a reflecting surface and transmissive devices. Most of the wavefront correctors used in adaptive optics are deformable mirrors, in which the shape of a reflecting surface is changed by means of a series of actuators. In the case of transmissive devices, a liquid crystal device is used. In such devices the optical path of light going through the screen can be changed in each pixel by applying a certain voltage to its electrodes. These devices can produce very high phase differences between adjacent pixels, and they are also very accurate in reproducing the shape of the wavefront to be corrected; however, their overall phase modulation is typically a maximum of $\approx 3\pi$, so that phase wrapping techniques must be used and their use is restricted to monochromatic light. On the other hand, since they are transmissive devices, dispersion needs to be taken into account, specially when using broadband sources of light. Also, the pixels in the screen form a grid, and its diffraction pattern can affect the quality of the image. In order to avoid the effect of the grating, only the central lobe of the transmitted beam is used, which means an important loss of light.

Deformable mirrors can be classified into continuous and segmented. Segmented mirrors can be described as small flat mirrors that can move in piston tip and tilt, although sometimes each segment can only perform some of these

movements. Different shapes have been used for the segments of these mirrors: square, hexagonal and circular. These kinds of devices are scalable to a very large number of segments, covering very large pupil sizes. Similarly to the case of transmissive devices, the grid of segments can diffract energy from the central lobe. Furthermore, light is lost in the gap between the segments. Another issue that needs to be considered with this kind of deformable mirror is the phase steps between the segments. If a broadband source is used, the segments must be absolutely phased (there should be no phase difference in the common side of adjacent segments), since modulo-2π steps would seriously degrade the performance of the system. These problems are avoided when using deformable mirrors with continuous faceplates.

Continuous faceplate deformable mirrors can be classified depending on the technique used to change the shape of the reflecting surface. There are several different techniques used to do so. One of them uses magnetostrictive materials, such as Terfenol, that change their shape when exposed to magnetic fields. Other use voice coils or helical solenoids, etc. But the most common actuators use either the piezoelectric effect or the electrostatic repulsion and attraction.

The piezoelectric effect can be used in several different ways to change the shape of the deformable mirror. It is used in edge actuated mirrors, in which a strip of piezoelectric ceramic is glued to the edges of the mirror as shown in figure 5.2.b. When a voltage is applied to the strip it changes its length, introducing a deformation in the mirror. However, the most common use of the piezoelectric effect in deformable mirrors is *bimorphs*. In this implementation, two layers of materials are bonded together. In general,

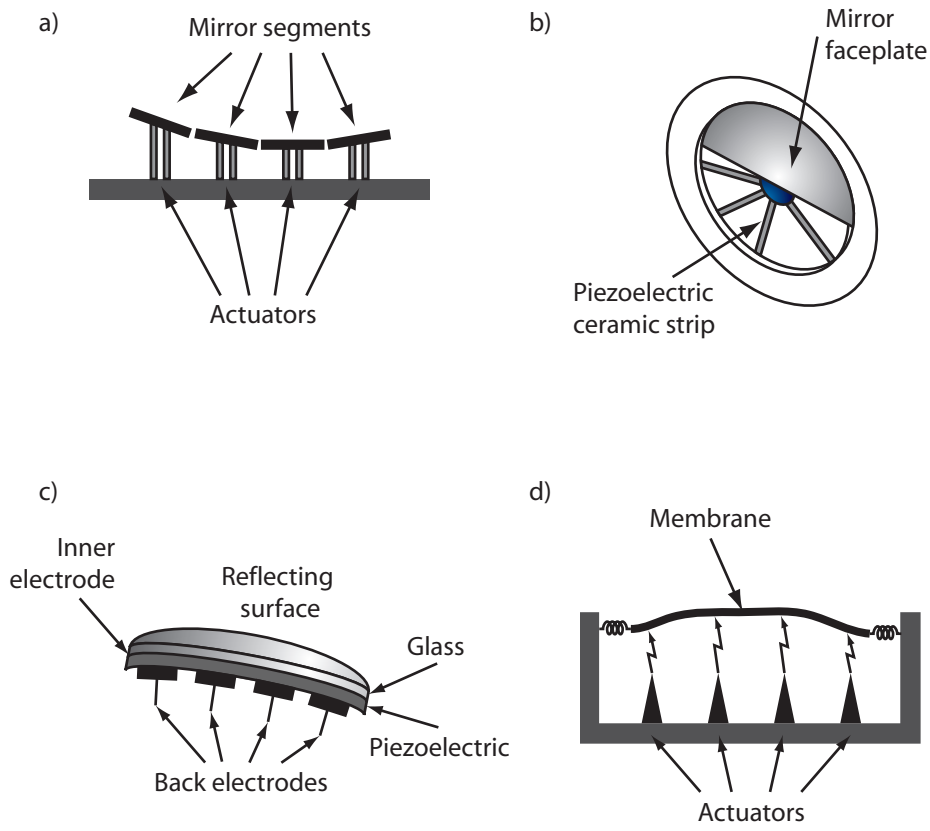

Figure 5.2: Simple scheme for several different types of deformable mirrors. a) Segmented mirror, b) Edge actuated piezoelectric mirror, c) bimorph mirror, d) micromachined membrane mirror

one of these is a piezoelectric material, while the other one is the optical surface, although other configurations are available in which both materials are piezoelectric, and the outer surface is the polished mirror face. A thin conductive film is deposited between the layers acting as electrode. When voltage is applied to the electrode, the area of the piezoelectric layer changes. Since the other layer, which in this case is the mirror, does not expand,the voltage results in a local bending. The surface deformation can be described using Poisson's equation as follows:

$$\nabla^2\Omega(x,y) = \frac{\partial^2\Omega(x,y)}{\partial x^2} + \frac{\partial^2\Omega(x,y)}{\partial y^2} \propto v(x,y) \tag{5.1}$$

Therefore, the mirror responds with a curvature proportional to the voltage applied. This behavior is very convenient for operation with curvature wavefront sensors because the reconstruction becomes simpler. The drawback, however, is the limit to which the bimorph can be forced into a series of aberration modes. This depends directly on the number of actuators in the mirror. Another characteristic to bimorphs is hysteresis, which is always present. Although this effect is usually low enough to be neglected, there are several reports presenting methods to minimize its effect [30].

In the implementation of the adaptive optics system described in this Thesis a micromachined deformable mirror (MMDM) is used. They can be made with up to a hundred actuators, a high bandwidth and negligible hysteresis. Furthermore, their production costs can be very low. Since they are based on electrostatic attraction and repulsion, their performance is limited to the voltage that can be applied to each of the actuators without interfering with the neighboring actuators. The mirror used in this work was a 37 actuator

OKO membrane deformable mirror, and is described with more detail in the sec. 6.4.

5.3 Control

In previous sections it has been explained how in an adaptive optics system, information from the wavefront sensor is collected, and it is processed using a control computer in order to send the appropriate signal to the correcting device. In this section a method to process this information is described.
The problem to solve in this situation is very similar to that faced in wavefront reconstruction in section 4.4. The signal obtained from the wavefront sensor is a series of displacements of the spots in the x and y directions. These displacements can be expressed as a vector:

$$\mathbf{M} = \begin{bmatrix} x_1 \\ x_2 \\ \vdots \\ x_l \\ y_1 \\ y_2 \\ \vdots \\ y_l \end{bmatrix} \tag{5.2}$$

where x_i and y_i are displacements in the x and y directions respectively and l is the number of lenslets in the Shack-Hartmann wavefront sensor. This signal needs to be transformed into a vector that contains the voltage that needs to be applied to each actuator of the correcting device:

$$\mathbf{V} = \begin{bmatrix} v_1 & v_2 & \dots & v_n \end{bmatrix} \tag{5.3}$$

where n is the number of actuators available in the correcting device. Therefore, a matrix is needed of the form:

$$\mathbf{V} = \mathbf{CM} \tag{5.4}$$

where $\mathbf{A}$ is a $2l \times n$ matrix, and it is referred to as calibration matrix from now on. The matrix $\mathbf{A}$ is unknown, but similarly to section 4.4 the pseudoinverse matrix $\mathbf{A}^{\dagger}$ can be easily determined. Consider the following equation:

$$\mathbf{M}^T = \mathbf{C}^{\dagger}\mathbf{V}^T \tag{5.5}$$

In order to determine this pseudoinverse matrix, it is necessary to assume that the influence function of each of the actuators in the wavefront corrector are independent of the voltage applied to the neighbor actuators. Furthermore the wavefront corrector is considered such that all the influence functions can be added linearly, i.e., if voltage is applied to actuators 1 and 2, for example, the effect on the wavefront is the same as if the deformation is applied using two identical mirrors in conjugate planes where in one of them voltage is applied only to actuator 1 and in the second voltage is applied to actuator 2. Using this assumption, the calibration matrix can be determined by applying the maximum and minimum voltage to each of the actuators while the rest are in the biased position. The spot position is determined for both voltages applied to each actuator. A certain matrix is determined then for each of these situations as follows:

$$\left.\begin{aligned} \mathbf{M}_{+,1}^{T} &= \mathbf{C}^{\dagger}\mathbf{V}_{+,1}^{T} \\ \mathbf{M}_{-,1}^{T} &= \mathbf{C}^{\dagger}\mathbf{V}_{-,1}^{T} \end{aligned}\right\} \tag{5.6}$$

where

$$\left.\begin{aligned} \mathbf{V}_{+,1} &= \begin{bmatrix} v_{max} & 0 & \dots & 0 \end{bmatrix} \\ \mathbf{V}_{-,1} &= \begin{bmatrix} v_{min} & 0 & \dots & 0 \end{bmatrix} \end{aligned}\right\} \tag{5.7}$$

Equations 5.6 and 5.7 are valid for actuator number 1, but they can be easily modified to correspond to each of the actuators of the wavefront corrector. Since only one of the voltages applied to the wavefront corrector is different to zero, each of the measurements of the spots displacements is related to one of the columns of $\mathbf{A}^{\dagger}$. If vectors $\mathbf{M}_{i,+}$ and $\mathbf{M}_{i,-}$ are subtracted, the quantity obtained is related to the displacement of the spots in the wavefront sensor for the whole range of voltages that can be applied to each of the actuators. Therefore, the pseudoinverse of the calibration matrix can be written as:

$$\mathbf{C}^{\dagger} = \begin{bmatrix} \frac{x_{1,1}^{+}-x_{1,1}^{-}}{v_{max}-v_{min}} & \frac{x_{2,1}^{+}-x_{2,1}^{-}}{v_{max}-v_{min}} & \cdots & \frac{x_{n,1}^{+}-x_{1,1}^{-}}{v_{max}-v_{min}} \\ \frac{x_{1,2}^{+}-x_{1,2}^{-}}{v_{max}-v_{min}} & \frac{x_{2,2}^{+}-x_{2,2}^{-}}{v_{max}-v_{min}} & \cdots & \frac{x_{n,2}^{+}-x_{1,2}^{-}}{v_{max}-v_{min}} \\ \vdots & \vdots & \ddots & \vdots \\ \frac{x_{1,l}^{+}-x_{1,l}^{-}}{v_{max}-v_{min}} & \frac{x_{2,l}^{+}-x_{2,l}^{-}}{v_{max}-v_{min}} & \cdots & \frac{x_{n,l}^{+}-x_{1,l}^{-}}{v_{max}-v_{min}} \\ & & & \\ \frac{y_{1,1}^{+}-y_{1,1}^{-}}{v_{max}-v_{min}} & \frac{y_{2,1}^{+}-y_{2,1}^{-}}{v_{max}-v_{min}} & \cdots & \frac{y_{n,1}^{+}-y^{-}1,1}{v_{max}-v_{min}} \\ \frac{y_{1,2}^{+}-y_{1,2}^{-}}{v_{max}-v_{min}} & \frac{y_{2,2}^{+}-y_{2,2}^{-}}{v_{max}-v_{min}} & \cdots & \frac{y_{n,2}^{+}-y_{1,2}^{-}}{v_{max}-v_{min}} \\ \vdots & \vdots & \ddots & \vdots \\ \frac{y_{1,l}^{+}-y_{1,l}^{-}}{v_{max}-v_{min}} & \frac{y_{2,l}^{+}-y_{2,l}^{-}}{v_{max}-v_{min}} & \cdots & \frac{y_{n,l}^{+}-y_{1,l}^{-}}{v_{max}-v_{min}} \end{bmatrix} \tag{5.8}$$

After $\mathbf{A}^{\dagger}$ is determined, the calibration matrix can be determined by performing the pseudoinverse as explained in section 4.4.

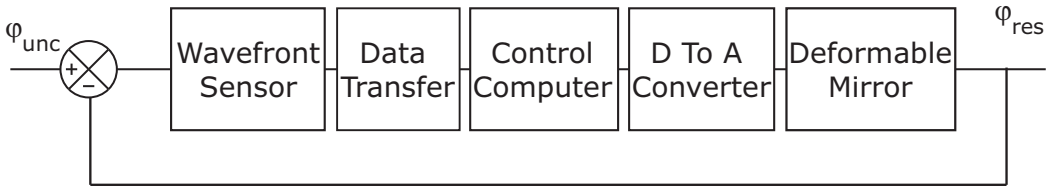

Figure 5.3: Block diagram for an AO system.

5.4 Temporal response

Any adaptive optics system can be considered as a servo-loop system. As shown in fig. 5.3, it consists of a sensor (the wavefront sensor), a control device (the computer that calculates correction from the wavefront sensor signal), and finally a compensating device (usually a deformable mirror, although other kinds of compensating devices can be used). The goal of this servo is to minimize the residual phase variation of the wavefront recorded by the wavefront sensor.

The input of the servo-loop is the uncompensated wavefront, that at a certain point (x, y) and time t is denoted by $\varphi_{unc}(x, y, t)$. If the correction introduced by the deformable mirror is $\varphi_{corr}(x, y, t)$, then the residual phase, $\varphi_{res}(x, y, t)$ is given by:

$$\varphi_{res}(x, y, t) = \varphi_{unc}(x, y, t) + \varphi_{corr}(x, y, t) \tag{5.9}$$

5.5 Transfer Function

From systems engineering it is known that in a linear system, the input $r(t)$ and output $c(t)$ signals are related by the following differential equation:

$$\frac{\mathrm{d}^n c(t)}{\mathrm{d}t^n} + a_{n-1}\frac{\mathrm{d}^{n-1} c(t)}{\mathrm{d}t^{n-1}} + \ldots + a_0 c(t) = b_m \frac{\mathrm{d}^m r(t)}{\mathrm{d}t^m} + b_{m-1}\frac{\mathrm{d}^{m-1} r(t)}{\mathrm{d}t^{m-1}} + \ldots + b_0 r(t) \tag{5.10}$$

Taking the Laplace transform of the previous expression, and using its properties it can be expressed as follows:

$$(s^n + a_{n-1}s^{n-1} + \ldots + a_0)C(s) = (b_m s^m + b_{m-1}s^{m-1} + \ldots + b_0)R(s) \tag{5.11}$$

where $C(s)$ and $R(s)$ are the Laplace transforms of $c(t)$ and $r(t)$ respectively. The transfer function can now be defined as the ratio between the Laplace transform of the output and the input, as shown below:

$$G(s) = \frac{R(s)}{C(s)} \tag{5.12}$$

It is also known that when the input function is an impulse function $r(t) = \delta(t)$, then its Laplace transform is $R(s) = 1$, and so the transfer function is the Laplace transform of the impulse response function. So, if the impulse response of the system can be measured, then its transfer function can be easily determined.

When two system components are combined in series, then the combined impulse response is the convolution of the impulse responses of the two components. Once again, using the properties of the Laplace transform it can be concluded that the transfer function a number of systems combined in series is given by:

$$G_{OL}(s) = G_1(s)G_2(s)\ldots G_n(s) \tag{5.13}$$

For the moment only an open loop system has been considered. This means that the the output of these systems have no interaction with its input, i.e. there is no feedback. Opposite to this would be a closed-loop system. In such systems a part of the output is coming back into the system as input again. In a system in which there is certain feedback, the input has the form of $C(s) - H(s)R(s)$, where $H(s)$ is the feedback parameter of the system. As stated before, the output is then:

$$C(s) = G_{OL}(C(s) + H(s)R(s)) \tag{5.14}$$

And from here, the closed loop transfer function can be obtained as

$$G_{CL} = \frac{G_{OL}s}{1 + H(s)G_{OL}(s)} \tag{5.15}$$

It is very interesting to determine both the closed-loop and open-loop transfer functions since they provide information of the temporal response of the system. In the following sections we discuss how these functions can be determined.

5.6 Open Loop Transfer Function

In order to estimate the open loop transfer function of the system, G_{OL}, the individual transfer functions for each component of the system must be determined. The system can be divided into the following components:

- Wavefront sensor
- Data transfer to control computer

- Control computer
- Digital-to-analogue converter
- Deformable mirror

5.6.1 Wavefront Sensor

The transfer function for the wavefront sensor is determined by the detector, in the case presented in this work, a CCD. The detector needs a certain integration time T to collect the light from the object. The signal at a certain time t is:

$$g(t) = \frac{1}{T}\int_{t-T}^{t} \phi(\tau)d\tau = \frac{1}{T}\int_{0}^{t} \phi(\tau)d\tau - \frac{1}{T}\int_{0}^{t-T} \phi(\tau)d\tau \tag{5.16}$$

Using the properties of the Laplace Transform $\mathscr{L}[f(t)e^{-at}] = F(s+a)$ and $\mathscr{L}[\int_0^t f(\tau)d\tau] = \frac{1}{s}F(s)$, the previous equation can be re-written as:

$$G_{WFS}^{OL}(s) = \frac{1 - e^{-Ts}}{Ts} \tag{5.17}$$

5.6.2 Data transfer to computer

Once the image has been acquired, it needs to be digitized and transferred to process its information. This task introduces a delay, that is going to be referred to as τ. The transfer function related to this process is;

$$G_{OL}^{TR}(s) = e^{-\tau s} \tag{5.18}$$

5.6.3 Control computer

The main task of the control computer is to perform a matrix multiplication in order to determine the voltage values that need to be applied to the deformable mirror to correct for the wavefront aberration. In general, the values of the voltages that need to be applied to the mirror depend on the previous values applied to the mirror and previous measurements of the wavefront sensor. So the controller can be described as:

$$O(nT) = \sum_{j=0}^{p} b_j I((n-j)T) - \sum_{i=1}^{l} a_i O((n-i)T) \tag{5.19}$$

where $O(kT)$ and $I(kT)$ are respectively the output (voltage values) and the input (wavefront sensor results) of the controller at the kth control step, and a_i and b_j the coefficients of the controller. The temporal characteristics of the controller depend then on the values of a_i and b_j. Since the controller works in the sampled time domain, its transfer function is defined by its Z-transform. Using the following characteristic of the Z-transform:

$$Z(O((n-k)T)) = z^{-k} Z(O(nT)) \tag{5.20}$$

the transfer function of the control computer can be written as:

$$G_{OL}^{CC}(z) = \frac{\sum_{j=0}^{p} b_j z^{-j}}{1 + \sum_{i=1}^{l} a_i z^{-i}} \tag{5.21}$$

In general, the output of the system can be considered proportional to the previous output values, i.e., $a_i = 1$, and in a simple approach of the controller, only the results related to the previous measurement of the wavefront sensor are taken into account. Using these approximations, eq. 5.21 can be written

as

$$G_{OL}^{CC}(z) = \frac{gz}{1+z} \tag{5.22}$$

where g is referred to as the integrator gain.

Since Z-transform is the expression of a transfer function of a process taking place in the sampled time domain, it can be studied in the continuous time domain using the classical transformation $z = e^T s$. This assumption is valid within the low frequency domain, which is of interest for an adaptive optics system. The transfer function of the control computer is then:

$$G_{OL}^{CC}(s) = \frac{g}{1+e^{-Ts}} \tag{5.23}$$

5.6.4 Digital-to-analogue converter

On the other hand, the values of the voltages that are sent to the mirror from the control computer need to be converted from the digital values calculated to some analogue voltages applied to the mirror. This task is performed by a digital analogue converter (DAC). This device holds the value of the voltages applied constant during a period of time T, until the next voltages are available from the control computer. The transfer function of such device is called zero-order holder:

$$G_{OL}^{DAC}(s) = \frac{1-e^{-Ts}}{Ts} \tag{5.24}$$

5.6.5 Deformable Mirror

The response of the deformable mirror is fast enough for its transfer function to be considered as one in the range of frequencies in which we are going to focus when determining the system temporal performance.

5.6.6 Overall open-loop transfer function

Assuming the linearity of the system, its open-loop transfer function can be written as the overall product of the transfer functions of the different components of the electronic system described above.

$$G^{OL} = \frac{g\left(1 - e^{-Ts}\right)e^{-\tau s}}{T^2 s^2} \tag{5.25}$$

As an example of a common AO system, let the value of the exposure time of the CCD used in a Shack-Hartmann wavefront sensor be $T = 50ms$, while the read-out delay time is $\tau = 20ms$. Assuming the value of the gain used in the control computer is $g = 0.7$, the open loop transfer function for such system is as shown in figure 5.4.

From the figure the bandwidth of the system can be defined. The bandwidth of the system is related to the frequency domain at which the system is effective, i.e., aberrations changing at a rate included in the bandwidth of the system can be corrected, while those changing at higher frequencies could be probably attenuated, but not completely removed. Using the open loop transfer function, the bandwidth can be determine using the 0 dB open-loop cut-off frequency. For frequencies lower than this bandwidth, the system is able to apply a gain in the loop, i.e., to compensate for perturbations. For

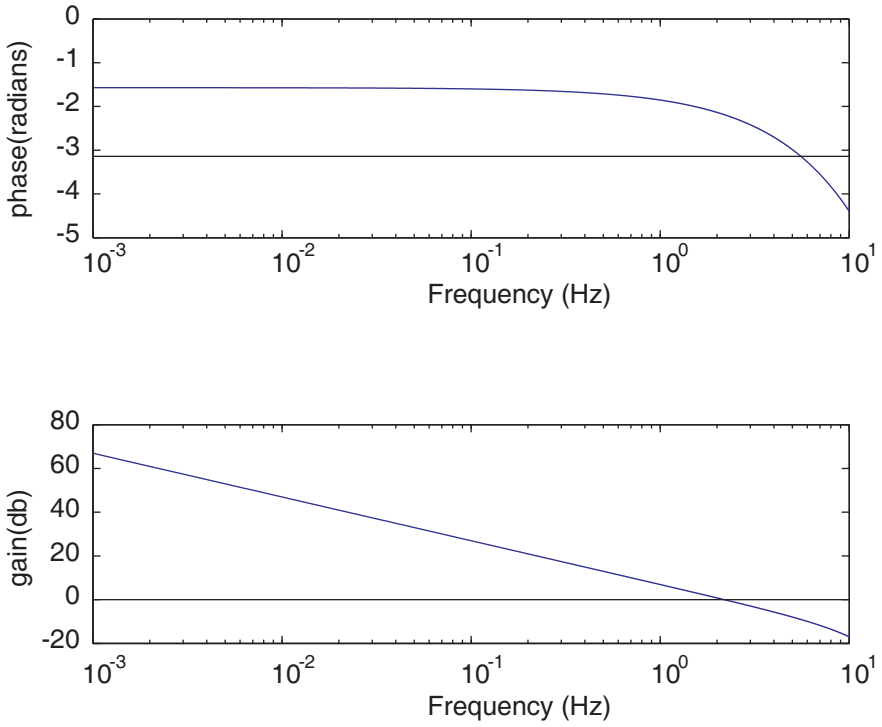

Figure 5.4: Open loop transfer function for a system with exposure time $T = 50ms$*, readout time* $\tau = 20ms$ *and gain* $g = 0.7$

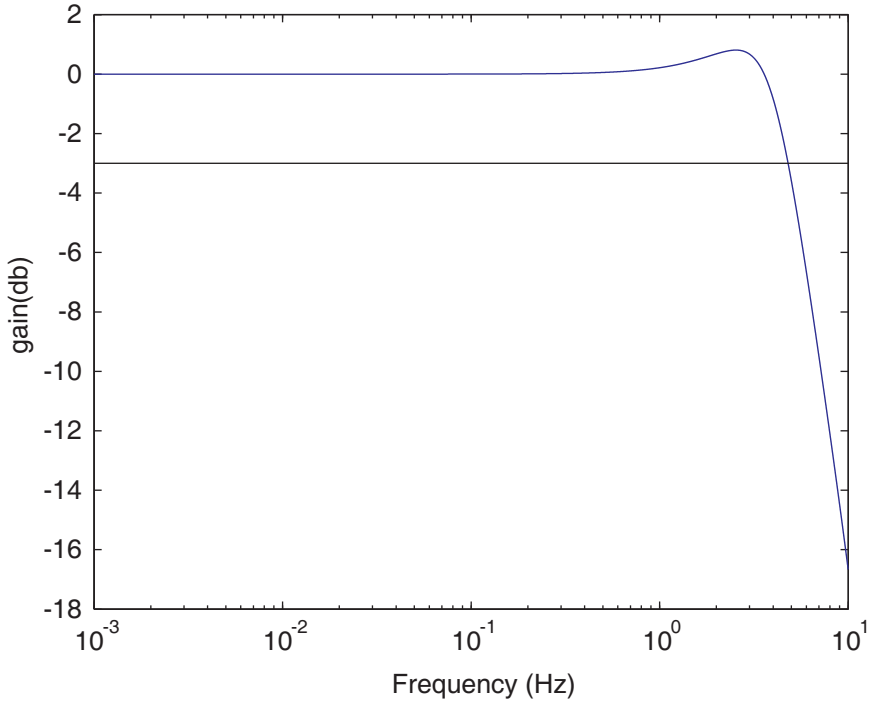

Figure 5.5: Closed loop transfer function for a system with exposure time $T = 50ms$*, readout time* $\tau = 20ms$ *and gain* $g = 0.7$

higher frequencies, the system attenuates the signal in the loop, and no more correction can be obtained. In the case of the open-loop transfer function shown in figure 5.4, the bandwidth of the system using this criterion would be approximately 2 Hz. In the following sections, other definitions of the bandwidth of the system are described.

5.7 Closed-Loop Transfer Function

As already explained in section 5.5, the closed-loop transfer function of the system can be obtain by means of the open-loop transfer function using eq. 5.15. Figure 5.5 shows an example of a closed-loop transfer function.

Using the closed-loop transfer function of the system a new definition of the bandwidth can be used. It corresponds to the classical -3 dB closed-loop cut-off frequency. This definition is well suited to a classical servo where the output is the main parameter, but in the case of an adaptive optics system it is of little interest. However, this is the definition generally used from a commercial point of view, since it gives the highest value of the bandwidth of all the definitions available. In the case of the example shown in figure 5.5, the resulting bandwidth using this definition is approximately 4.5 Hz, which is double of the bandwidth obtained using the 0 dB cut-off frequency for the open-loop transfer function.

However, the closed-loop transfer function is very useful in order to determine the maximum gain that can be applied to the system. The closed-loop transfer function is in general characterized by an overshoot close to the limit bandwidth. The stability of the system is ensured when this overshoot is below a certain value, which is generally fixed to 2.3 dB. Changing the value of the gain if the control computer, the shape of the overshoot changes, and the optimum gain can be set using the closed-loop transfer function.

5.8 Closed-loop error transfer function

The closed-loop error function is defined as the transfer function between the residual phase and the turbulent wavefront fluctuations. It represents the ability of the system to compensate for phase perturbations as a function of frequency. This quantity is very important, since it characterizes the efficiency of the correction introduced by the system. It can be written as:

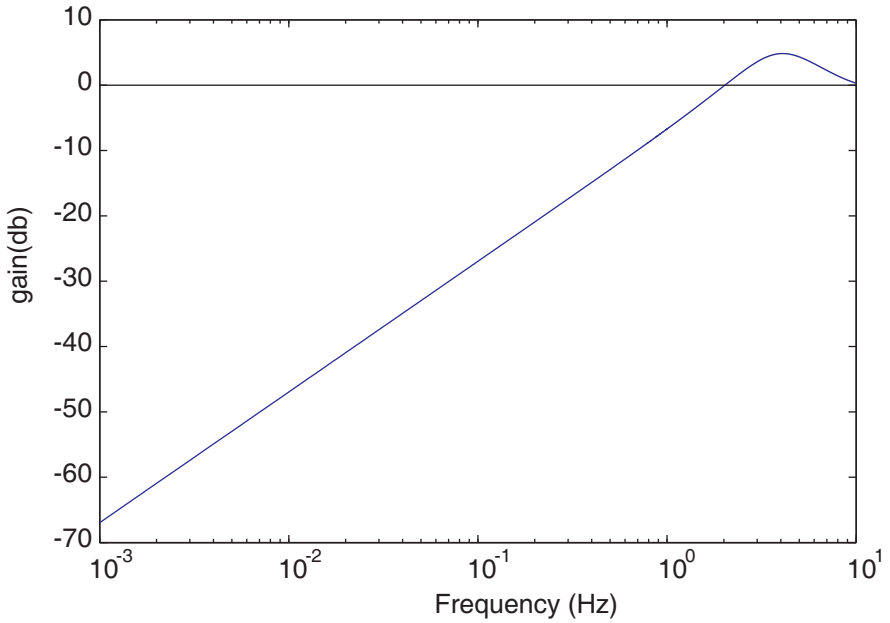

Figure 5.6: Closed loop error transfer function for a system with exposure time $T = 50ms$, readout time $\tau = 20ms$ and gain $g = 0.7$

$$E(s) = \frac{1}{1 + G_{OL}(s)} \tag{5.26}$$

A new definition of the bandwidth of the system can be suggested from the definition of the closed-loop error transfer function, and it is its 0 dB cut-off frequency. This definition is related to the residual optical phase after correction. For lower frequencies than this bandwidth the system attenuates the perturbations, while for higher frequencies there is no effect. Therefore, this is the bandwidth of frequencies for which the system is efficient. Figure 5.6 shows an example of a closed-loop error transfer function. The bandwidth using this definition of the particular system related to that transfer function is approximately 2 Hz.

5.9 Implementation

In the previous section it has been explained how the calibration matrix is used to transform the signal obtained from the wavefront sensor into a suitable vector of voltages that should be applied to the wavefront corrector in order to avoid the aberrations introduced in the system (in the case of retinal images by the aberrations of the subject's eye). However, the practical implementation of the control loop should take into account some factors that have not been mentioned so far. First, it should be taken into account that the system will sample the wavefront for its posterior correction at a certain rate F. The simplest integrator that can be performed is as follows:

$$r(n) = r(n-1) + \frac{g}{F}c(n) \tag{5.27}$$

where $r(n)$ and $c(n)$ are respectively the output and the input of the corrector for the nth iteration, which needs to be added to the correction that has been applied in the previous iteration, $r(n-1)$, and g is the gain of the integrator. In a real system, other components should be added to this controller in order to improve its performance. A component that is important to introduce in this integrator is a bleeding factor. When using a Shack-Hartmann wavefront sensor, and due to the fact that the aberration of the wavefront is sampled over the pupil area, there may be mirror modes that are not detected by the wavefront sensor that build up in the system. This is the case of the waffle modes. A simple solution to this problem is to add a weak proportional component to the control which will slowly bleed off all system modes, including the unseen modes. The controller becomes:

$$r(n) = r(n-1) + \frac{g}{F}c(n) - \beta r(n-1) \tag{5.28}$$

being β the bleeding parameter.

6

Adaptive optics enhanced simultaneous en-face optical coherence tomography and scanning laser ophthalmoscopy

Now that scanning laser ophthalmoscopy and optical coherence tomography have been introduced, and it has been explained how adaptive optics can be used to correct for ocular aberrations, improving the quality of retinal images obtained using these techniques, in this chapter we describe how they were combined together in order to obtain simultaneous *en-face* OCT/SLO images with pixel-to-pixel correspondence and improved quality thanks to adaptive optics. The adaptive optics enhancement described in this chapter is solely my own work, but the AO-OCT/SLO system as a whole is a combined effort of Dr. Adrian Bradu and Prof. Adrian Podoleanu of the University of Kent at Canterbury, and myself.

6.1 Adaptive optics and retinal imaging

Since it was first suggested, adaptive optics has been widely used in vision science for different applications. The most important of them is retinal imaging. The first implementation of adaptive optics for retinal imaging was created by Liang *et al.* [57] with a combination of a fundus camera with adaptive optics. Thanks to this technique it has been possible to map the different types of photoreceptors [65, 57] in the human eye for several different subjects, proving the variability in the distribution between subjects of the three types of photoreceptors in the human eye [83].

After improving the resolution of fundus cameras, many other techniques used in retinal imaging have benefit from the aberration correction introduced by AO. Roorda *et al.* built an adaptive optics scanning laser ophthalmoscope system [82]. This device was able to produce images of the retina of the living eye with near to diffraction limit resolution. The frame rate of the system was enough as to produce real time videos of the retina, showing the blood flow through its vessels. Furthermore, the depth sectioning capability characteristic of the SLO technique enabled Roorda *et al.* to obtain images of different layers of the retina for the first time in the living human eye [82, 81]. The system was based on a double pass configuration, and the lateral resolution was improved from $5\mu m$ to $2.5\mu m$ while depth resolution was better than $100\mu m$ while in conventional SLO systems it usually is of $300\mu m$.

Adaptive optics has also been implemented together with optical coherence tomography by several authors [46, 103, 102]. The first implementation of AO OCT was presented by Hermann *et al.* [46]. The system was based on

an ultrahigh-resolution (UHR) OCT system by Drexler *et al.* [28, 27]. An adaptive optics device was attached to the system by means of a couple of telescopes built using spherical mirrors. The telescopes ensured the wavefront corrector was on a plane conjugate to the pupil of the eye. Before the scanning mirrors, a beam splitter was used to direct light into the eye. The incoming beam only reached the deformable mirror on the way out from the eye, and therefore the diameter of the beam reaching the eye had to be small enough to ensure the spot on the retina was nearly diffraction limited [12]. The optimal correction for the subject aberration was then calculated using a closed-loop system, and once the RMS values for the residual aberration where below $0.1\mu m$ across a $3.68mm$ pupil, the deformable mirror was frozen. Then the illumination was changed in order to use the UHR OCT system as a traditional OCT system.

The lateral resolution using AO was improved by a factor of 2-3, reaching transverse resolutions of about $5 - 10\mu m$, depth resolutions of $\sim 3\mu m$ and an increase in the SNR of $\sim 9dB$.

Zhang *et al.* presented in 2005 the first implementation of a spectral domain OCT system with adaptive optics [103]. This implementation allowed real time correction of the aberrations of the eye while simultaneously acquiring longitudinal OCT retinal images at a very fast rate. The device developed also included a conventional *en-face* camera, and it was able to produce two dimensional images of the retinal microscopic structure. The system used a $843nm$ wavelength SLD for both OCT and flood illumination, and a different $788nm$ SLD to close the AO loop. Dielectric beamsplitters were used to reflect the light from the $788nm$ SLD into the arm of the Shack-Hartmann

wavefront sensor, while the light from the $843nm$ SLD is transmitted on to the OCT and flood-illuminated detection channel. In such system, the light scattered from the retina is combined with that reflected from the reference arm when reaching the deformable mirror. In order to prevent reference contamination, the central region of the deformable mirror in which the light from the reference arm is confined is frozen.

It is well known that spectral domain OCT is able to produce a higher SNR than in the case of traditional time domain OCT [49, 22, 24, 55]. Furthermore, using this technique the information needed to produce an image is acquired faster, since a complete scan in the direction of the optical axis is produced at once. However, this means that the images obtained are only focused at a certain depth of the retina, and the rest is out of focus. In consequence, different images need to be produced in order to show detail for each of the retinal layers.

A sphero-cylindrical lens was introduced in the illumination arm of Zhang's system, so that the retina was illuminated by a $100\mu m$ long line and not a point as in traditional systems. This allowed an even faster frame-rate, since no scanning was needed to produce the images.

Changes in the SNR of 11.4 to $13.1dB$ were measured when the AO loop was closed, leading to an improvement in resolution, which reached values of $3.0\mu m$ for the lateral and $5.7\mu m$ for the axial resolutions.

Zawadzki *et al.* reported the ability to image microscopic blood vessels and the photoreceptor mosaic using a new implementation of a Fourier-domain OCT system, this one based on a double pass configuration, and used scanning mirrors in order to move the illuminating spot over the retina, in a

similar way SLO systems do. An increase of $9dB$ was reported due to the use of AO, and the resolution reached with this system were $4\mu m$ lateral and $6\mu m$ axial.

The systems mentioned above produce sections of the retina in a plane that is parallel to the optical axis of the eye. Other efforts have been reported in other variants of OCT. Such is the case of full-field OCT [36, 54], in which a whole *en-face* section of the retina is obtained at once, rather than scanning. This allows very short exposure times ($\sim 7ms$), avoiding any possible artifact due to eye movements.

It has been described in previous chapters how AO has been successfully combined with retinal imaging techniques such as SLO and OCT. Furthermore, it has also been explained how SLO and *en-face* OCT have been used simultaneously to produce images of the *in-vivo* human retina [72] that present pixel-to-pixel correspondence [69]. The technique is used to produce pairs of *en-face* OCT/SLO images, where the SLO images help determine the exact spatial location of the retinal patch imaged. Furthermore, if the source used to produce the SLO images has a wide spectrum, the images will present low speckle noise levels, helping detect small features that may be missed in the OCT channel due to high speckle noise levels [64].

In this chapter a novel combination of AO with a simultaneous *en-face* OCT/SLO system for high resolution retinal imaging of the *in-vivo* human retina is presented. An increase in the lateral resolution of the images obtained for both channels is expected, as well as an increase in the signal to noise ratio (SNR). The system is described and characterized in the following sections, and some results obtained using it are shown.

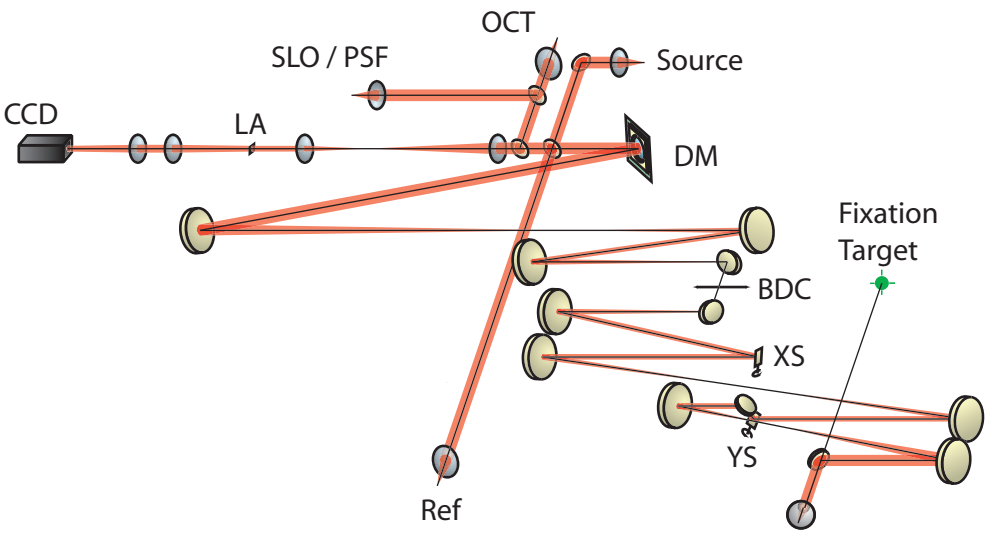

Figure 6.1: Sketch of the AO-OCT system presented in this work

6.2 Design

The AO-OCT system presented in this Thesis is shown in fig. 6.1. It consists of a Michelson interferometer, where light from the reference and probing beams is injected into optics fibers and then coupled to produce the interference patterns between them. Interference is then collected into two pin photodiodes in a balanced detector.

Light from the superluminescent diode (SLD) source, which is described in section 6.3, reaches a first beam splitter (90% transmittance, 10% reflectance) that divides the beam into the reference and probing beams. The probing beam is directed to a wavefront corrector, in this case a deformable mirror (DM) from OKO Technologies has been used and it is described in section 6.4. Light reflected from the DM is directed through a series of telescopes and scanning mirrors to the eye of the subject. These telescopes ensure that the DM plane is conjugate to the subject's pupil plane in the way in and

out of the eye. They are also used to change the diameter of the beam to match the size of the different optical elements, and finally set the size of the pupil in the subject's pupil plane. The telescopes are built with pairs of spherical mirrors placed slightly off axis. Spherical mirrors have been chosen rather than lenses in order to avoid the stray reflections from lens surfaces that may affect the performance of the Shack-Hartmann wavefront sensor. These mirrors are gold coated to suit the wavelength of the light source used. The second telescope has been set up so the distance between the spherical mirrors can be changed, as in a Badal defocus corrector. This is helpful to set the retinal layer at which the system is focused, as it is detailed in section 6.7. A telescope has been placed between the two scanning mirrors in order to ensure that the XS and YS are in conjugate planes. Other configurations have been presented in which the two scanners are close together with no elements between them. In that case the system is simpler, although some distortion is introduced to the image, that is not present in the case suggested in fig. 6.1. Furthermore, this simpler configuration does not ensure the lenslet array in the Shack-Hartmman wavefront sensor to be conjugate to the scanners planes. The scanning mirrors used in the system are described in section 6.5. They vibrate at 2 Hz for the Y or frame mirror (YS) and at 700 Hz for the X or line mirror (XS). Therefore the images are obtained at a frame rate of 2 Hz. This speed is quite slow compared to the involuntary movements of the eye (saccades and microsaccades), and may produce motion artifacts in the reconstructed images that should be take into account when interpreting them [90].

Light scattered back from the subject's retina is de-scanned by going through

the interface optics a second time, including the deformable mirror. The system is therefore a double pass system, in opposition to single pass systems, where aberrations are only corrected in the way out from the eye. The light beam reaches the deformable mirror in the way into the eye, allowing the use of a large diameter pupil on the incoming beam. Single pass systems need to work with a small entrance pupil, so the beam focused in the subject's retina is aberration free, and the PSF formed is near diffraction limited. In the case of double pass systems, the beam is pre-corrected by the deformable mirror before reaching the subject's eye, so the PSF formed on the retina is near diffraction limited even though the beam diameter is large.

The use of a double pass configuration, and long focal length mirrors determines a large size layout. The length of the probing arm is $\sim 5m$ in length each way, therefore the reference arm is $\sim$ 10 m in length. This may lead to thermal fluctuations of the optical path difference (OPD) and launching problems. An isolated optical bench was used to minimize this effect.

Light reflected from the deformable mirror passes through the first beam splitter again and reaches a second beam splitter (1% T, 99% R). Light transmitted through this splitter is directed to the Shack-Hartmann wavefront sensor. The wavefront sensor is able to work with such low light levels because it uses a very sensitive camera from Andor Technologies [1]. It is a DV887 front illuminated iXon camera. Transmitted light is sent to a third beam splitter where reflected light (30%) is sent to the SLO channel and that transmitted (70%) is sent to the OCT channel. In both channels light is injected into single mode fibers. This ensures a high confocal parameter in both channels and good spatial rejection of multiple scattered light. In

the OCT channel, light is guided towards a single mode directional coupler where it interferes with that coming from the reference arm. The two output fibers from the DC are connected to two pin photodetectors in a balanced photodetection unit, Nirvana 2007. In the case of the SLO channel, light injected into the single mode fiber is guided to a C5460-01 avalanche photodiode from Hamamatsu. The last focusing element and the fiber end in the reference arm are fixed on a translation stage that has a range of 2.5 cm along the optical axis of the beam, useful to allow coherence matching for different lengths of the subject's eyes. The stage can also be used to construct B scans. A B-scan image of the retina is obtained by stopping the frame scanner and moving the translation stage [75]. Such images are similar to longitudinal scans of the retina delivered by traditional OCT, however, in this case the fast direction of scanning is perpendicular to the optical axis, while the slow scanning is performed along the optical axis.

6.3 Light source

The light source used in the system presented is a superluminescent diode model PTLD 635-10 9003 from Laser2000 [3]. Its central wavelength is $831nm$, and its bandwidth is $17nm$. This source is in the central part of the therapeutic window, a range of the optical spectrum in which absorption in biological tissue reaches a minimum. These wavelengths range approximately from 600 to $1300nm$. The wavelength used is at the limit of sensitivity of the eye (usually considered to be 400 to $750nm$). We considered this to be another advantage of the light source used, because it is hardly visible, and although the light levels used to image the subject's retina may

be high, it is not only safe but more comfortable for the subject. Furthermore, since the wavelength used is at the red side of the visible spectrum, the maximum permitted exposure dictated by the The European Committee for Electrotechnical Standardization [6] is higher than for more energetic wavelengths, and thus higher light levels may be safely used. In the system described here the optical power reaching the subject's cornea is 300 μW. This value is well below the 700 μW threshold dictated by The European Committee for Electrotechnical Standardization for a non-scanning beam at 831 nm (note that in our case the beam is scanning, and therefore the maximum permitted exposure in this case is higher, but for safety, we calculated the values for a non scanning beam). Such a low value of optical power needed to obtain retinal images is possible in part due to the CCD used in the wavefront sensor, as it will be detailed in following sections.

Finally, the bandwidth of the optical source used determines the depth resolution of the OCT channel, as it has been explained in chapter 3. The SLD source used has a bandwidth of 17nm, which sets a depth resolution of approximately $13\mu m$ in the eye.

6.4 Deformable mirror

The wavefront corrector used in the work presented in this Thesis was a 37 actuator MMDM from OKO Technologies, shown in fig. 6.2. This mirror has been used previously in a number of reports correcting for ocular aberrations [35, 46, 43]. The actuators of this mirror are placed over the pupil in an hexagonal distribution. It has a pupil diameter of 15 mm, although the pupil used in the system presented in this Thesis is of only 9.5 mm diameter.

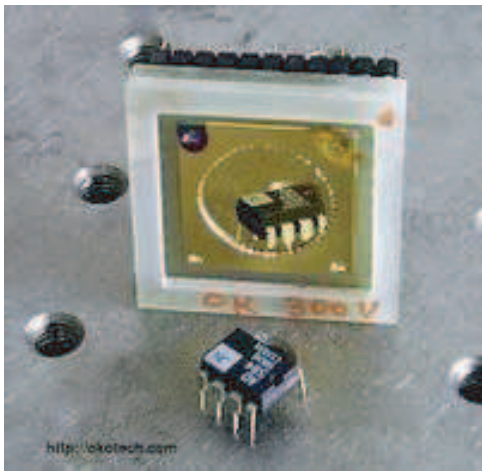

Figure 6.2: Picture of the 37 element OKO MMDM [4]

This reduction of the usable area of the pupil is to avoid the effect of the borders of the membrane.

The specifications of such device predict a maximum correction of $8\mu m$, although that depends on the shape of the wavefront to be corrected. In figure 6.3, the influence functions of the actuators of the deformable mirror are shown when each actuator is poked and the rest of them remain in the biased position. The peak to valley of such influence functions is of around 1 μm, although they are shown for a voltage applied to each actuator that is lower than the maximum allowed. The influence functions were obtained using an interferometer, and poking each of the actuators using a value of voltage of $125V$, while $0V$ was applied to the rest of the actuators.

The mirror was mainly designed to dynamically correct for defocus and astigmatism, although it has also been used to correct higher order aberrations[35, 46]. Although its performance is limited, and there are a number of mirrors available with better specifications for the application described here [23], it has been chosen because of its low cost (commonly used in low-cost implemen-

tation of adaptive optics), and the previous experience acquired using this mirror in similar applications related to retinal imaging and psycho-physical experiments in vision science [43, 40].

6.5 Scanning mirrors

The scanning mirrors used in the experiment are 6210-X and 6210-Y, from Laser 2000 and Cambridge Technology. They are galvo scanners with moving coil and moving magnet, and can vibrate at speeds of up to several kHz. However in this experiment they vibrate at $700Hz$ the line or X scanner, and at $2Hz$ the frame or Y scanner.

They have been placed in the system at two different planes, each of them conjugated to the pupil of the eye. Some other configurations have been used in similar systems, and both of the scanners have been placed close to a single conjugate plane. This would have produce a smaller system, but the image obtained may have been affected by some distortion, and therefore the option was dismissed.

6.6 Wavefront sensor

The wavefront sensor used is a Shack-Hartmann wavefront sensor based on a DV887 front illuminated CCD iXon camera from Andor Tech [1]. This is a very sensitive camera, and although it is not essential for the implementation of a system like the one described here, it has allowed to lower the light levels necessary to obtain the pairs of *en-face* OCT/SLO images.

The system was designed so only 0.9% of the light scattered back from the

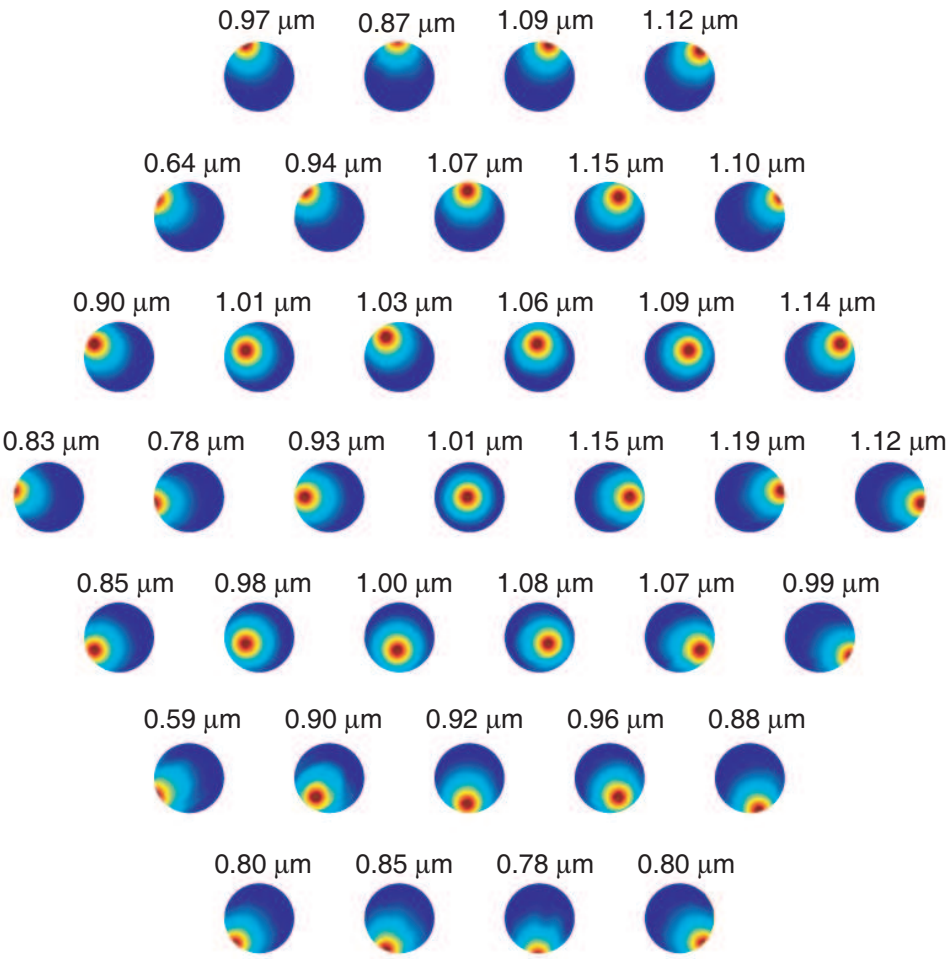

Figure 6.3: Influence functions of each of the actuators of the 37 OKO MMDM. The value above each influence function corresponds to the peak to valley distance. Results from E. Dalimier.

patient's retina is directed to the wavefront sensor. In this way, the light used by the imaging arm is maximized. This is essential, since in the system presented there are two kinds of images that are created simultaneously, and therefore in principle, more light is needed than in the case of an *en-face* OCT or SLO systems working independently. The system worked sending only $300\mu W$ of light into the subject's cornea. This value is well below the $700\mu W$ maximum exposure permitted for a non-scanning beam working at $780nm$, which is more restrictive than a scanning beam, like the one used in the system presented [6].

The focal lengths of the spherical mirrors chosen for the interface optics of the system where such that the magnification between the subject's pupil plane and the lenslet array plane is roughly 2:1. The lenslet array chosen for this set-up is a square one from WelchAllyn, with $200\mu m$ pitch and $7.5mm$ focal length, magnified to $390\mu m$ in the subject's pupil plane. For a pupil size of 6mm, the number of sub-apertures used is 120.

6.7 Image acquisition procedure

The acquisition speed is one of the reasons why it is very important to fixate the subject's head in a position that is as stable as possible. In the system presented a head rest in addition to a bite bar is used (HeadSpot and Bite-Buddy models from UHCO Tech [5]). No drops to dilate the pupil or block accommodation where used to obtain the results presented in this chapter. Furthermore the subjects selected to test the performance of the system did not require previous correction for defocus or astigmatism, and they did not wear spectacles nor contact lenses either.

The volunteers were asked to position their head in the system and to move it guided by an operator driving the system. The optimal pupil position was achieved when the spots pattern in the wavefront sensor matched the pattern used as reference. Once the pupil was placed in position, the volunteer was asked to tilt his head up and down to obtain maximum signal injected into the single mode fibers. The process was repeated if further corrections of the pupil position were needed.

After the pupil position was set, the Badal defocus corrector was adjusted subjectively to obtain maximum sharpness of the scanning line seen by the volunteer. We believe this resulted in placing the focus at the photoreceptor level, although the SLO image was used to determine the layer at which the system is focused, as it will be explained later in this chapter.

Once these steps were successfully performed, the data acquisition started, and measurements were obtained both with and without adaptive optics correction.

6.8 Adaptive optics system performance

In order to determine the performance of the adaptive optics system, it is necessary to determine a series of parameters. It is important to know to what extent the aberrated wavefront from the subject's eye is corrected and turned into a plane wavefront, and also it is necessary to determine what is the temporal response of the system, both working in open and closed look. This two points are going to be discussed separately in this section.

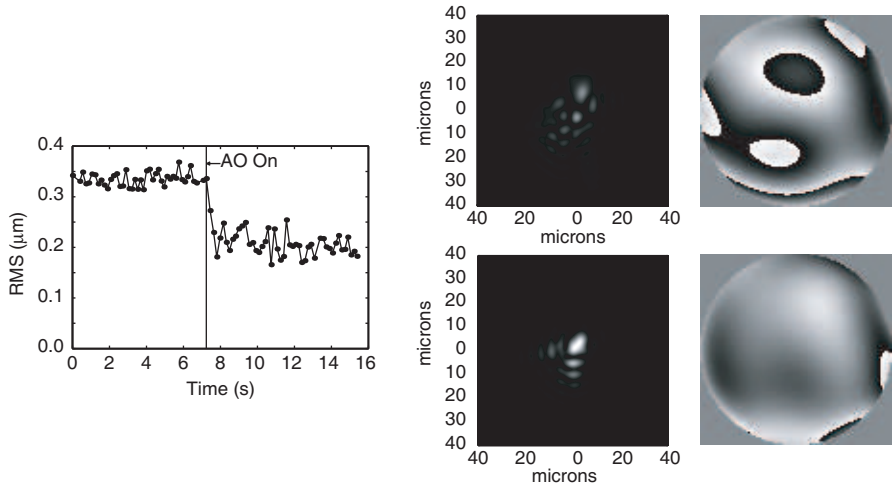

Figure 6.4: On the left the reconstructed wavefront RMS evolution is shown just before and after the AO loop is closed. On the right, the reconstructed wavefront and the corresponding PSF are shown without (top) and with (bottom) AO correction. These data were obtained from subject AB

6.8.1 Wavefront correction performance

To determine the performance of the system in terms of wavefront correction the information of the wavefront sensor is used. The information related to the spots displacement when a subject has placed his eye in the system was stored for posterior processing. The adaptive optics system was turned on during the period of time in which these data were recorded. The spots displacement information obtained from the wavefront sensor was used to determine the decomposition of the wavefront on a base using Zernike polynomials as explained in section 4.4. The RMS of the wavefront was determined using this information, and figure 6.4 shows the evolution of the RMS for subject AB. This result has been obtained for a 6 mm pupil, and is in good

agreement with previous results obtained using the same deformable mirror [23]. We believe that the correction achieved is mainly limited by the parameters of the deformable mirror used: the limited number of actuators and their restricted stroke. From a comparative study of commercially available low-cost deformable mirrors [23], it is clear that other mirror technologies will yield greatly improved performance.

6.8.2 Temporal response

The temporal response of the system has been determine as explained in section 5.5. The exposure time used in the CCD of the WS was $\sim 64ms$, which was the shortest exposure allowed by the camera. The time required to transfer the information of the image from the CCD to the computer was $\sim 55ms$. Compared to these quantities the time needed by the control computer to determine the voltages needed in the deformable mirror to correct for the subject's eye aberration and the time needed by the deformable mirror apply those voltages are negligible. Using these parameters, the open-loop, closed-loop and closed-loop error transfer functions have been determined, and the results are shown in figures 6.5, 6.6 and 6.7 respectively.

These figures can be used to determine the bandwidth of the system. There are several different criteria that can be used to calculate this quantity [78]. The first way to determine the bandwidth of an adaptive optics system is the classical -3 dB closed-loop cut-off frequency. This is the bandwidth used in commercially available adaptive optics systems. The second criterion to determine the bandwidth is to determine the point at which the open-loop transfer function is 0 dB. For frequencies lower than this bandwidth, the

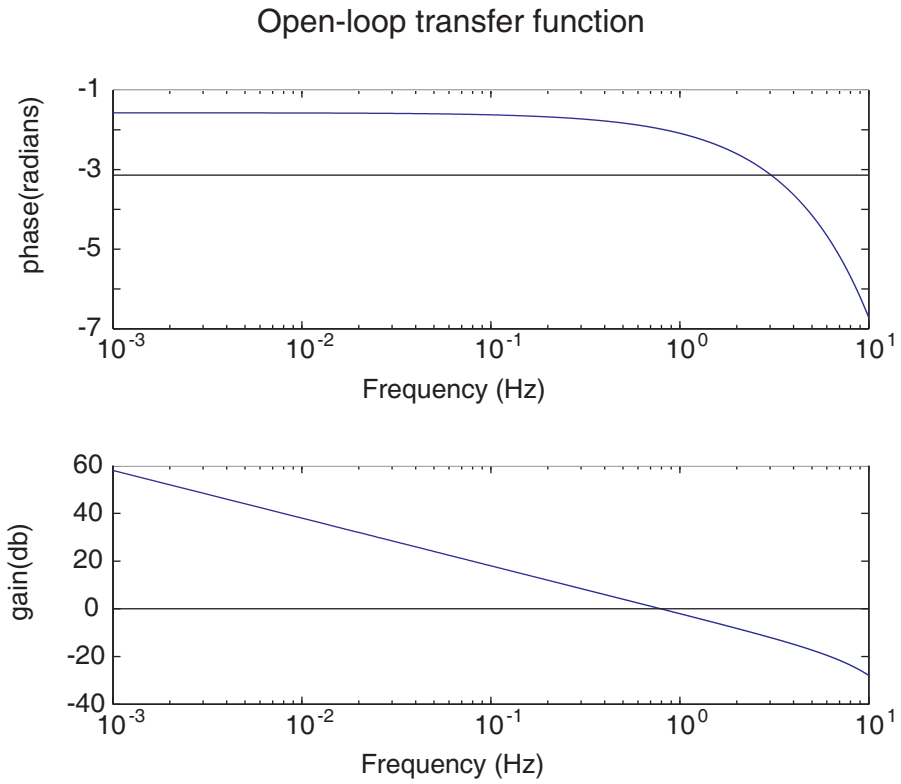

Figure 6.5: Open-loop transfer function of the adaptive optics system

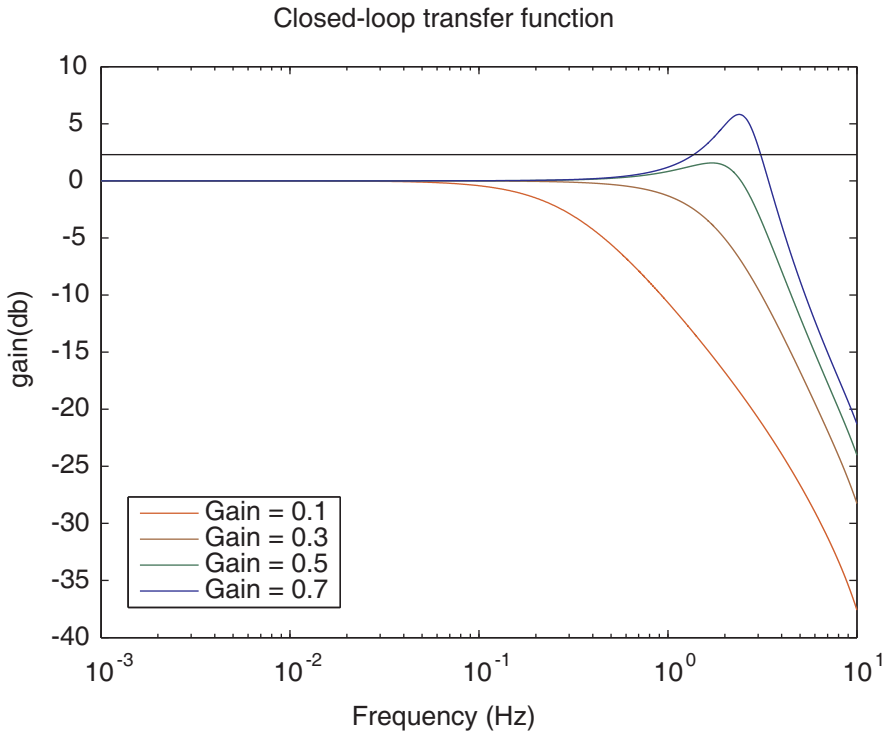

Figure 6.6: Closed-loop transfer function of the adaptive optics system

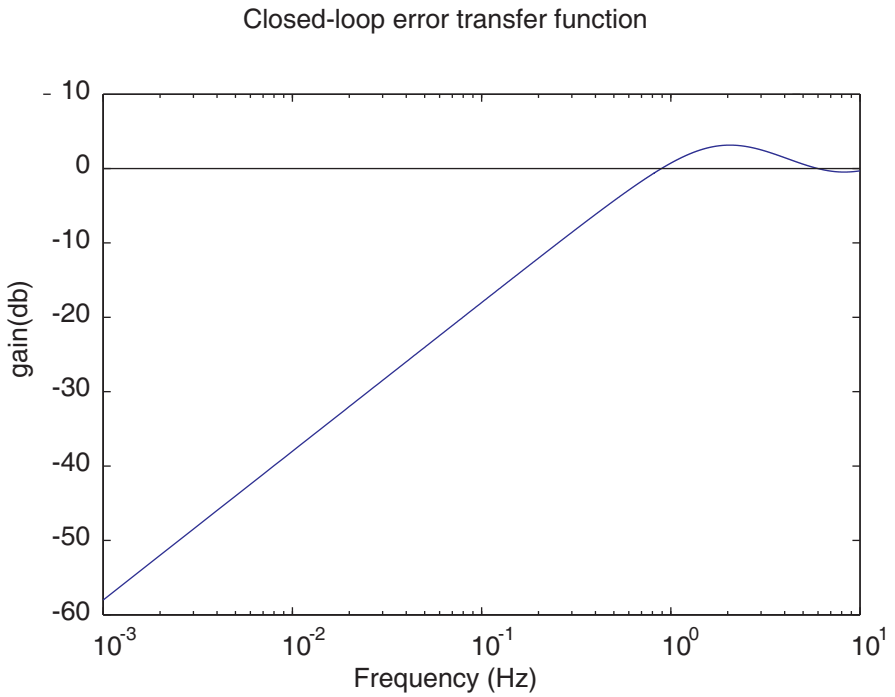

Figure 6.7: Closed-loop error transfer function of the adaptive optics system

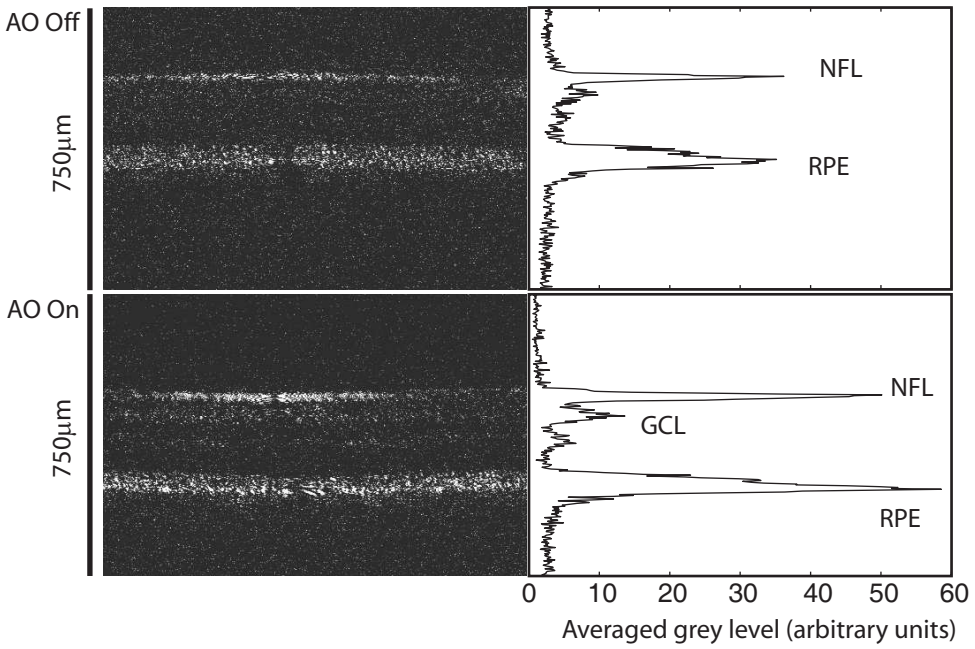

Figure 6.8: Retinal images from subject AB

system is able to apply gain in the loop, i.e., compensate for perturbations. The third is the 0 dB closed-loop error cut-off. This definition is related to the residual optical phase after correction, since for frequencies lower than this bandwidth, the adaptive optics system attenuates the perturbations. As it can be seen in the plots of the transfer functions of the system presented, the three criteria set a value for the bandwidth of the system close to 1Hz.

6.9 Results

The system has been used to obtain *en-face* B-scan and C-scan images, both using AO and without using it.

Fig. 6.8 shows an example of the B-scans or longitudinal images obtained without (top) and with (bottom) adaptive correction. The images are *en-face*

B-scans, i.e. they are longitudinal images (parallel to the optical axis) but the fast scanning axis is perpendicular to the optical axis. The plots on the right hand side show the grey level values averaged over the x axis. These values are used to compare the signal strength reflected from each of the retinal layers. The figure shows how the peaks corresponding to the nerve fiber layer (NFL) and the retinal pigment epithelium (RPE) are higher when adaptive optics correction is applied. Other peaks too, corresponding to layers that were almost masked by noise become more visible with adaptive optics, that is the case of the layer labelled as the ganglion cell layer (GCL). Due to the reduction of the wavefront aberration, an increase in the SNR is expected. Because the noise does not change when the AO loop is turned on, an increase in the signal strength due to AO produces a similar increase in the SNR. The SNR was improved by 4 to $6dB$ on the OCT channel, and of 7 to $9dB$ in the SLO channel. The range of values presented here correspond to the values obtained for two different subjects, but these values were repeatable for both of them. Because the OCT signal is proportional to the square root of the reflectivity, it is expected that the improvement in dB in the OCT channel is only half of that in the SLO channel.

Since the system is based on a confocal configuration, one would expect the intensity of the signal to increase only for the layer where the system is focused at. But the results presented in figure 6.8 show an increase in the signal strength for all depths in the retina. However, the increase in the signal corresponding to the RPE layer is higher than that for the NFL. This is compatible with the fact that the system is focused at the photoreceptor layer - RPE depth to obtain the images shown. This point will be discussed

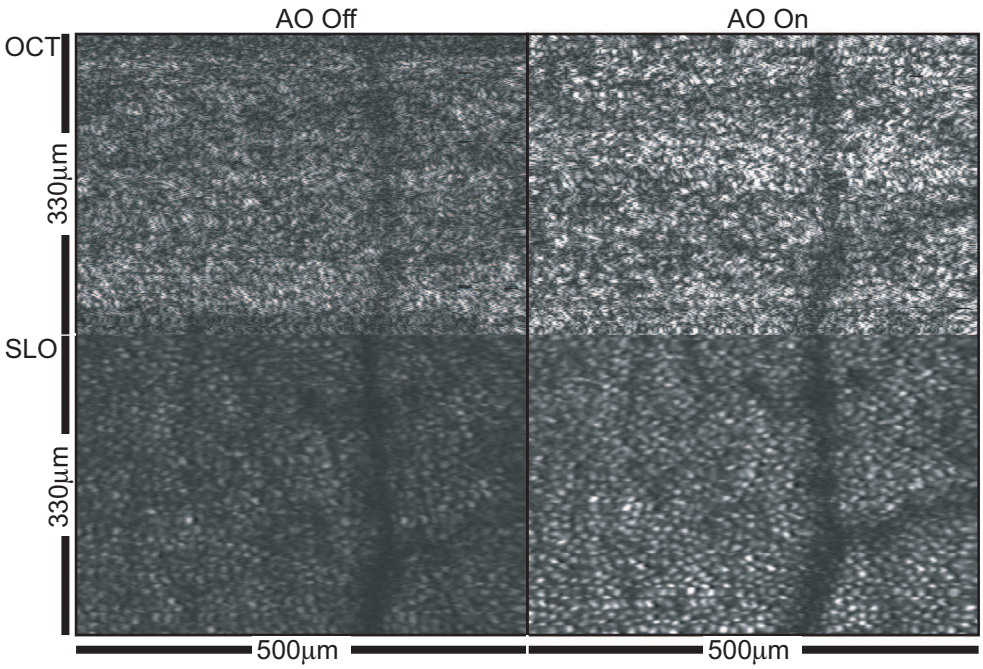

Figure 6.9: Retinal images from subject DM

in more detail later in this section.

Fig. 6.9 shows some images obtained for subject DM. These are C-scans, corresponding to the photoreceptor layer. They are pairs of images obtained simultaneously using the *en-face* OCT and SLO channels. The left pair has been obtained without adaptive optics correction, while to obtain the right pair AO correction was used.

Let us concentrate first on the SLO images (bottom). The images show the retinal layer at which the system is focused. It is obvious the similarity of the images with those shown in [82] corresponding to the photoreceptor layer: the shadow of a blood vessel shown, which places the plane at the deeper

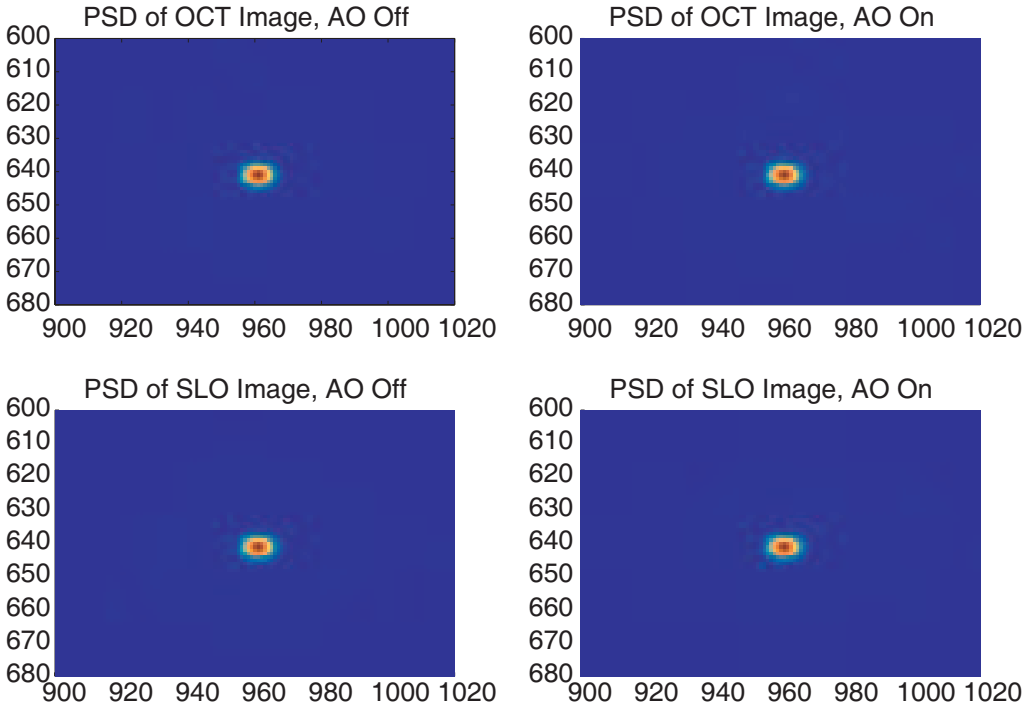

Figure 6.10: Power spectral density of the en-face *OCT and SLO images from fig. 6.9*

part of the retina, while the dimensions of the spots shown in the image correspond with those of photoreceptors for the area of the retina [57].

To measure the separation between spots in the images shown the power spectral density of the image has been performed. The results are shown in fig. 6.10. The figure shows a ring around the central spot. This rings corresponds to the spatial periodicity of the spots, and is therefore related to the separation between the spots. As already stated, this separation corresponds with the separation of the photoreceptors at that area of the retina, which is about $\sim 10\mu m$.

An improvement in the transversal resolution of the en-face images was noticed. To evaluate this enhancement we calculated the power spectral density

of the images obtained from the OCT and SLO channels was also used. We determined a circle of radius r for which the volume under the PSD curve was 99 in the resolution of the images has been detected [40], showing $r = 6.5\mu m$ before and $5\mu m$ after applying adaptive correction in both channels. This slight improvement in the transversal resolution together with the enhancement in the signal strength noticed leads to better observation of photoreceptor structure in both OCT and SLO images after the AO loop is switched on.

7

Discussion and further work

Once the results obtained using the system built have been described, in this chapter they are going to be discussed, and some directives for further work are suggested.

7.1 Discussion

We have presented a system that is able to produce retinal images of the living human eye using two different techniques simultaneously: SLO and *en-face* OCT. Due to the nature of the technique used, the images obtained from each channel present pixel-to-pixel correspondence. The system is equipped with a Shack-Hartmann wavefront sensor and a deformable mirror, that work together in closed-loop in order to correct for the aberrations of the eye in an AO system.

Measurements of the evolution of the wavefront aberration RMS have been presented that show how this value is reduced from $\sim 0.35\mu m$ to $\sim 0.2\mu m$

for a particular subject. This shows a reduction of the wavefront aberration RMS of 1.75.

The reduction in wavefront RMS introduced by the AO device, produced an increase in the SNR in both channels. In the SLO channel, the SNR increased $4 - 6dB$ in the SLO channel and $7 - 9dB$ in the OCT channel when adaptive optics correction was applied. The ratio in this increase for the SLO and OCT channel is in agreement with the theory, that predicts that the increase in the OCT channel should be half of that for the SLO channel. This produces an increase in the amount of light injected into the fiber optics.

All these effects of AO in the signal of the OCT channel allow to obtain images in which photoreceptors are visible. To our knowledge this is the first time in which cones are easily identified on an imaged obtain using OCT, and it is achieved by means of AO.

However, the increase in the SNR for the OCT system is below the values measured in reports available on the literature [46, 103, 102].

The improvement in SNR measured for the OCT channel is lower than the values available in literature and in particular it is lower than that obtained with a similar deformable mirror [46]. The pupil size in the case of Herman *et al.* is $3.7mm$. This is significantly smaller than in the case presented here, $6mm$. Furthermore, our system is based on a double pass configuration, while Hermann *et al.* present a single pass system. They can follow this approach since the beam entering the eye is very narrow, and therefore it can be considered as diffraction limited. Although both systems are using a similar mirror, we believe these differences do not allow them to be compared. It

has been observed in our laboratory how the OKO mirror is not good enough for large size pupils [23], where the aberration pattern becomes complicated and this particular mirror is not able to reproduce it. Furthermore, in the case of our system, the correction is of the order of two times the correction that Hermann *et al.* need to apply, since their is a single pass system.

For the case of Zhang *et al.*, they report an increase in the SNR of $11-13dB$. They use a similar pupil size to the one used in our system. However, the deformable mirror they used presents a much better performance than the one used in our experiments. Therefore it is expected that the wavefront aberration RMS they obtain to be better than ours, and therefore, the SNR increase would also be higher.

As in the case of Hermann *et al.*, Zhang's system is based on a single pass configuration. This point, again, is expected to affect the performance of the mirror.

In any case, we have been able to show an improvement in the image quality due to the effect of AO. The OCT images obtained show a similar structure than that present on the SLO images. The difference between them is that the information shown on the OCT image is only coming from a layer that is $13\mu m$ deep, while on the SLO image the information is coming from a layer that is more than $200\mu m$ deep. The OCT image is selecting only the information related to a certain layer of the retina (which we think is the photoreceptor layer), while the information displayed on the SLO image is probably coming also from other layers, e.g. the RPE. The images, apart from being brighter when AO is applied, show more clearly the photoreceptor structure when the adaptive optics correction is applied. Also, on that

situation, some of the individual photoreceptors can be identified both in the OCT and SLO images, while it is more difficult on the OCT image without AO.

7.2 Further Work

The main conclusion reached while working with the system presented is that the OKO MMDM is not suitable for an application like the one described here. Although it is a low cost mirror, its performance is not enough in terms of stroke and reproduction of the shape of the wavefront aberration. It is suggested to change the mirror for another one using a different technology. Some results have been presented that show how piezoelectric mirrors could be a good choice, since they are not very expensive and produce much higher stroke and a better performance in terms of wavefront aberration reproduction [23]. However there is a drawback for this kind of mirrors, and it is that they are usually larger than micromachined ones. This would be a problem for a system like the one presented here, since the size of the system is already an issue. A larger size mirror would need longer focal lengths in the spherical mirrors, and the size of the system would increase. This point will be discussed in more detail later. We believe a better choice would be the Mirao mirror from Imagine Eyes [2, 34]. The pupil size of this mirror is similar to that of the OKO mirror, while the stroke is much larger ($\sim 50\mu m$). It is formed by 52 actuators, and in the specifications it is reported that it can correct for ± 5 dipoters of astigmatism. This may mean that the deformable mirror can be used to correct for both, defocus, astigmatism and higher order aberrations, without the need for a Badal defocus corrector like the one used

in the system presented here.

As already mentioned, another issue with the AO-OCT/SLO system is its size. Due to the fact that the system is based on a double pass configuration, spherical mirrors are necessary to avoid reflections from lenses surfaces. This reduces the choice of focal lengths for the optical elements used, and due to the design requirements the distances in the system are very long. Furthermore, and also due to the double pass configuration, the reference beam is very long ($\sim 10m$). If the system was based on a single pass configuration, the size of the system could be considerably reduced. However, the use of lenses in an OCT system introduces dispersion in the beam. This should be taken into account and corrected, usually by introducing the same optical elements in both arms.

Finally another problem that should be addressed in the system we have built is the acquisition speed. The scanning mirrors used only allowed a frame rate of 2 Hz. At this frame rate we believe that only experienced subjects are suitable to obtain meaningful retinal images. For this reason it is desirable to produce images at a much faster rate, since the involuntary movements of the eye may introduce artifacts in the images obtained. Other technologies for the scanning mirrors should be then considered, such as resonant mirrors. Increasing the speed of the scanning mirrors may have an effect in the light levels needed to obtain the retinal images. This may mean that as the frame rate increases, the light levels needed would increase as well, approaching the safe maximum permitted exposure.

Bibliography

[1] Andor Technologies website: www.andortechnologies.com.

[2] Imagine Eyes website: www.imagine-eyes.com.

[3] Laser2000 website: www.laser2000.co.uk.

[4] OKO Technologies website: www.okotech.com.

[5] UHCO Tech website: www.opt.uh.edu/go/uhcotech/project-list/headspot.

[6] *Safety of Laser Products*. The European Committee for Electrotechnical Standardization, 2003.

[7] S. A. Al-Chalabi, B. Culshaw, and D. E. N. Davies. Partially coherent sources in interferometric sensors. *First International Conference on Optical Fibre Sensors*, 1983.

[8] J. Arines. *Imagen de alta resolución del fondo de ojo por deconvolución tras la compensación parcial*. PhD thesis, Universidad de Santiago de Compostela, 2006.

[9] J. Arines and J. Ares. Minimum variance centroid thresholding. *Opt. Lett.*, 27(7):497–499, 2002.

[10] P. Artal, L. Chen, E. J. Fernández, B. Singer, S. Manzanera, and D. R. Williams. Neural compensation for the eye's optical aberrations. *Journal of Vision*, 4:281–287, April 2004.

[11] P. Artal and A. Guirao. Contributions of the cornea and the lens to the aberrations of the human eye. *Opt. Lett.*, 23(21):1713–1715, November 1998.

[12] P. Artal, I. Iglesias, N. López-Gil, and D. G. Green. Double-pass measurements of the retinal-image quality with unequal entrance and exit pupil sizes and the reversibility of the eye's optical system. *J. Opt. Soc. Am. A*, 12(10):2358–2366, October 1995.

[13] P. Artal, S. Marcos, I. Iglesias, and D.G. Green. Optical modulation transfer function and contrast sensitivity with decentered small pupils. *Vision Research*, 36(22):3575–3586, 1996.

[14] P. Artal, S. Marcos, R. Navarro, and D. R. Williams. Odd aberrations and double-pass measurements of retinal image quality. *J. Opt. Soc. Am. A*, 12(2):195–201, February 1995.

[15] H. W. Babcock. The possibility of compensating astronomical seeing.

Publications of the Astronomical Society of the Pacific, 65(386):229–236, October 1953.

[16] S. Barbero, S. Marcos, and J. Merayo-Lloves. Corneal and total optical aberrations in a unilateral aphakic patient. *Journal of Cataract and Refractive Surgery*, 28:1594–1600, September 2002.

[17] M. Born and E. Wolf. *Principles of Optics*. Cambridge University Press, 6th edition, 1980.

[18] B. E. Bouma and G. J. Tearney. Clinical imaging with optical coherence tomography. *Academic Radiology*, 9(8):942–953, August 2002.

[19] A. Bradu, A. Gh. Podoleanu, D. Merino, and C. Dainty. Adaptive optics - *en-face* optical coherence tomography and scanning laser ophthalmoscopy. Adaptive optics beyond astronomy, November 2005. Glasgow, UK.

[20] A. Bradu, A. Gh. Podoleanu, D. Merino, and C. Dainty. First adaptive optics - simultaneous *en-face* optical coherence tomography and scanning laser ophthalmoscopy. Presetations by Britain's Younger Physicists at the House of Commons, November 2005. London, UK.

[21] S. R. Chamot, C. Dainty, and S. Esposito. Adaptive optics for ophthalmic applications using a pyramid wavefront sensor. *Optics Express*, 14(2):518–526, January 2006.

[22] M. A. Choma, M. V. Sarunic, C. Yang, and J. A. Izatt. Sensitivity advantage of swept source and fourier domain optical coherence tomography. *Optics Express*, 11(18):2183–2189, September 2003.

[23] E. Dalimier and C. Dainty. Comparative analysis of deformable mirrors for ocular adaptive optics. *Optics Express*, 13:4275–4285, 2005.

[24] J. F. de Boer, B. Cense, B. Hyle Park, M. C. Pierce, G. J. Tearney, and B. E. Bouma. Improved signal-to-noise ratio in spectral-domain compared with time-domain optical coherence tomography. *Opt. Lett.*, 28(21):2067–2069, November 2003.

[25] L. Diaz-Santana and J. C. Dainty. Effects of retinal scattering in the ocular double-pass process. *J. Opt. Soc. Am. A*, 18(7):1437–1444, July 2001.

[26] L. Diaz-Santana, C. Torti, I. Munro, P. Gasson, and C. Dainty. Benefit of higher closedloop bandwidths in ocular adaptive optics. *Optics Express*, 11(20):2597–2605, October 2003.

[27] W. Drexler. Ultrahigh resolution optical coherence tomography. *J. Biomed. Opt.*, 9:47–74, 2004.

[28] W. Drexler, U. Morgner, R. K. Ghanta, F. X. Kärtner, J. S. Schuman, and J. G. Fujimoto. Ultrahigh-resolution ophthalmic optical coherence tomography. *Nature Medicine*, 7:502–507, 2001.

[29] A. Dubois, K. Grieve, G. Moneron, R. Lecaque, L. Vabre, and A.C. Boccara. Ultrahigh-resolution full-field optical coherence tomography. *Applied Optics*, 43(14):2874–2883, 2004.

[30] A. Dubra, J. Massa, and C. Patterson. Preisach classical and nonlinear modeling of hysteresis in piezoceramic deformable mirrors. *Optics Express*, 13(13):9062–9070, October 2005.

[31] A. Dubra, C. Paterson, and C. Dainty. Study of the tear topography dynamics using a lateral shearing interferometer. *Optics Express*, 12(25):6278–6288, 2004.

[32] A. G. Van Engen, S. A. Diddams, and T. S. Clement. Dispersion measurements of water with white-light interferometry. *Applied Optics*, 37(24):5679–5686, April 1998.

[33] A. F. Fercher, W. Drexler, C. K. Hitzenberger, and T. Lasser. Optical coherence tomography-principles and applications. *Reports on Progress in Physics*, 66:203–303, 2003.

[34] E. Fernández, L. Vabre, B. Hermann, A. Unterhuber, B. Povaẑay, and W. Drexler. Adaptive optics with a magnetic deformable mirror: applications in the human eye. *Optics Express*, 14(20):8900–8917, October 2006.

[35] E. J. Fernández, I. Iglesias, and Pablo Artal. Closed-loop adaptive optics in the human eye. *Opt. Lett.*, 26(10):746–748, May 2001.

[36] M. Glanc, D. Lafaille, P. Puget, F. Lacombe, L. Vabre, X. Levecq, and N. Chateau. Full-field ao-assisted oct for high-resolution tomographic imaging of the retina. *Proc. SPIE*, 6079, February 2006.

[37] J. W. Goodman. *Statistical Optics*. John Wiley and Sons, 1985.

[38] K. Grieve, M. Paques, J. Sahel A. Dubois, A.C. Boccara, and J.-F. Le Gargasson. Ocular tissue imaging using ultrahigh resolution full-field optical coherence tomography. *Investigative Ophthalmology and Visual Science*, 45:4126–4131, 2004.

[39] D. A. Gros and R. W. West. *Introduction to the Optics of the Eye*. Oxford, 2001.

[40] S. Gruppetta. *High-Resolution Retinal Imaging using Adaptive Optics in a Confocal Laser Scanning Ophthalmoscope*. PhD thesis.

[41] S. Gruppetta, L. Koechlin, F. Lacombe, and P. Puget. Curvature sensor for the measurement of the static corneal topography and the dynamic tear film topography in the human eye. *Opt. Lett.*, 30(20):2757–2759, October 2005.

[42] K. M. Hampson, I. Munro, C. Patterson, and C. Dainty. Weak correlation between the aberration dynamics of the human eye and the cardiopulmonary system. *J. Opt. Soc. Am. A*, 22(7):1241–1250, July 2005.

[43] K. M. Hampson, C. Patterson, C. Dainty, and E. A. H. Mallen. Adaptive optics system for investigation of the effect of the aberration dynamics of the human eye on steady-state accommodation control. *J. Opt. Soc. Am. A*, 23(5):1082–1088, May 2006.

[44] J. W. Hardy, J. E. Lefebvre, and C. L. Koliopoulos. Real-time atmospheric compensation. *J. Opt. Soc. Am.*, 3:360–369, 1977.

[45] J. C. He, S. A. Burns, and S. Marcos. Monochromatic aberrations in the accommodated human eye. *Vision Research*, 40(1):41–48, January 2000.

[46] B. Hermann, E. J.Fernández, A. Unterhuber, H. Sattmann, A. F.

Fercher, and W. Drexler. Adaptive-optics ultrahigh-resolution optical coherence tomography. *Opt. Lett.*, 29:2142–2144, 2004.

[47] H. Hofer, P. Artal, B. Singer, J. L. Aragn, and D. R. Williams. Dynamics of the eye's wave aberration. *J. Opt. Soc. Am. A*, 18(3):497–506, March 2001.

[48] H. Hofer, L. Chen, G. Y. Yoon, Y Yamauchi, and D. R. Williams. Improvement in retinal image quality with dynamic correction of the eye's aberration. *Optics Express*, 8(11):631–643, May 2001.

[49] D. Huang, E. A. Swanson, C. P. Lin, J. S. Schuman, W.G. Stinson, W. Chang, M. R. Hee, T. Flotte. K. Gregory, C. A. Puliafito, and J. G Fujimoto. Optical coherence tomography. *Science*, 254:1178–1181, 1991.

[50] I. Iglesias, R. Ragazzoni, Y. Julien, and P. Artal. Extended source pyramid wave-front sensor for the human eye. *Optics Express*, 10(9):419–428, May 2002.

[51] W. J. Donnelly III and A. Roorda. Optimal pupil size in the human eye for axial resolution. *J. Opt. Soc. Am. A*, 20:2010–1015, 2003.

[52] P. L. Kaufman and A. Alm. *Adler's Physiology of the Eye.* Mosby, 10th edition, 2003.

[53] A. N. Kolmogorov. The local structure of turbulence in an incompressible fluid for very large reynolds numbers. *Dokl. Akad. Nauk. SSSR*, 1941.

[54] D. Lafaille. *Tomographie Optique Cohérent et Optique Adaptative: Ètude d'un prototype d'application à l'ophtalmologie*. PhD thesis, Université Paris 7, 2004.

[55] R. Leitgeb, C. K. Hitzenberger, and A. F. Fercher. Performance of fourier domain vs. time domain optical coherence tomography. *Optics Express*, 11(8):889, April 2003.

[56] J. Liang and D. R. Williams. Aberrations and retinal image quality of the normal human eye. *J. Opt. Soc. Am. A*, 14(11):2873–2883, November 1997.

[57] J. Liang, D. R. Williams, and D. T. Miller. Supernormal vision and high-resolution retinal imaging through adaptive optics. *J. Opt. Soc. Am. A*, 14(11):2884–2892, November 1997.

[58] N. López-Gil, I. Iglesias, and P. Artal. Retinal image quality in the human eye as a funtion of the accommodation. *Vision Research*, 38(19):2897–2907, July 1998.

[59] S. Marcos, S. A. Burns, E. Moreno-Barriusop, and R. Navarro. A new approach to the study of ocular chromatic aberrations. *Vision Res.*, 39:4309–4323, 1999.

[60] S. Marcos, S. A. Burns, P. M. Prieto, R. Navarro, and B. Baraibar. Investigating sources of variability of monochromatic and transverse chromatic aberrations accross eyes. *Vision Research*, 41(28):3861–3871, December 2001.

[61] J. S. McLellan, S. Marcos, and S. A. Burns. Age-related changes in monochromatic wave aberrations of the human eye. *Inv. Ophthalm. Vis. Science*, 42(6):1390–1395, May 2001.

[62] J. S. McLellan, S. Marcos, P. M. Prieto, and S. A. Burns. Imperfect optics may be the eye's defence against chromatic blur. *Nature*, 417:174–176, May 2002.

[63] D. Merino, A. Bradu, C. Dainty, and A. Podoleanu. Adaptive optics optical coherence tomography for retinal imaging. 5th International Workshop on Adaptive Optics for Medicine and Industry, August 2005. Beijing, China.

[64] D. Merino, C. Dainty, A. Bradu, and A. Gh. Podoleanu. Adaptive optics enhanced simultaneous en-face optical coherence tomography and scanning laser ophthalmoscopy. *Optics Express*, 14(8):3345–3353, April 2006.

[65] D. T. Miller, D. R. Williams, G. M. Morris, and J. Liang. Images of cone photoreceptors in the living human eye. *Vision Res.*, 36(8):1067–1079, 1996.

[66] R. Navarro and M. A. Losada. Phase transfer and point spread function of the human eye determined by a new asymmetric double-pass method. *J. Opt. Soc. Am. A*, 12:2386–2392, 1995.

[67] A. Gh. Podoleanu. Unbalanced versus balanced operation in an optical coherence tomography system. *Applied Optics*, 39(1):173–182, 2000.

[68] A. Gh. Podoleanu. New advances in the *en-face* optical coherence tomography applied to eye imaging. Engineering the Eye II: Imaging the Retina, June 2006. Galway, Ireland.

[69] A. Gh. Podoleanu, G. M. Dobre, R. C. Curu, , R. Rosen, P. Garcia, J. Nieto, D. Will, R. Gentile, T. Muldoon, J. Walsh, L. A. Yannuzzi, Y. Fisher, D. Orlock, R. Weitz, J. A. Rogers, S. Dunne, and A. Boxer. Combined multiplanar optical coherence tomography and confocal scanning ophthalmoscopy. *J. Biomed. Opt.*, 9:86–93, January 2004.

[70] A. Gh. Podoleanu, G. M. Dobre, and D. A. Jackson. *En-face* coherence imaging using galvanometer scanner modulation. *Opt. Lett.*, 23(3):147–149, February 1998.

[71] A. Gh. Podoleanu, G. M. Dobre, D. J. Webb, and D. A. Jackson. Coherence imaging by use of a Newton rings sampling function. *Opt. Lett.*, 21(21):1789–1791, November 1996.

[72] A. Gh. Podoleanu and D. A. Jackson. Combined optical coherence tomograph and scanning laser ophthalmoscope. *Electro. Lett.*, 34(11):1088–1090, May 1998.

[73] A. Gh. Podoleanu and D. A. Jackson. Noise analysis of a combined optical coherence tomograph and a confocal scanning ophthalmoscope. *Applied Optics*, 38:2116–2127, 1999.

[74] A. Gh. Podoleanu, J. A. Rogers, and D. A. Jackson. Oct *en-face* images

from the retina with adjustable depth resolution in real time. *IEEE Journal of Selected Topics in Quantum Electron.*, 5:1176–1184, 1999.

[75] A. Gh. Podoleanu, M. Seeger, G. M. Dobre, D. J. Webb, D. A. Jackson, and F. W. Fitzke. Transversal and longitudinal images from the retina of the living eye using low coherence reflectometry. *J. Biomed. Opt.*, 3(1):12–20, January 1998.

[76] J. Porter, A. Guirao, I. G. Cox, and D. R. Williams. Monochromatic aberrations of the human eye in a large population. *J. Opt. Soc. Am. A*, 18(8):1793–1803, August 2001.

[77] W. H. Press, S. A. Teukolsky, W. T. Vetterling, and B. P. Flannery. *Numerical Recipes in C++, The Art of Scientific Computing*. Cambridge University Press, 2nd edition, 2002.

[78] F. Roddier. *Adaptive Optics in Astronomy*. Cambridge University Press, 1st edition, 1999.

[79] F. Roddier, C. Roddier, and N Roddier. Curvature sensing: a new wave-front sensing method. *Proc. SPIE*, 976:203–209, 1988.

[80] J. Rogers. *Advances in Optical Coherence Tomography for imaging and flow measurement*. PhD thesis, University of Kent at Canterbury, 2001.

[81] F. Romero-Borja, K. Venkateswaran, A. Roorda, and T. Hebert. Optical slicing of human retinal tissue in vivo with the adaptive optics scanning laser ophthalmoscope. *Applied Optics*, 44(19):4032–4040, July 2005.

[82] A. Roorda, F. Romero-Borja, W. J. Donelly III, H. Queener, T. J. Herbert, and M. C. W. Campbell. Adaptive optics scanning laser ophthalmoscope. *Optics Express*, 10:405–412, 2002.

[83] A. Roorda and D. R. Williams. The arrangement of the three cone classes in the living human eye. *Nature*, 397(11):520–522, 1999.

[84] J. M. Schmitt. Optical coherence tomography (OCT): A review. *IEEE Journal of Selected Topics in Quantum Electronics*, 5(4):1205–1215, July/August 1999.

[85] L. N. Thibos. Principles of Hartmann-Shack aberrometry. *Journal of Refractive Surgery*, 16:563–565, September/October 2000.

[86] L. N. Thibos, R. A. Applegate, J. T. Schwiegerling, and R. Webb. Standards for reporting the optical aberrations of eyes. *Journal of Refractive Surgery*, 18:652–660, September/October 2002.

[87] L. N. Thibos, A. Bradley, and X. Hong. A statistical model of the aberration structure of normal, well-corrected eyes. *Ophthal. Physiol. Opt.*, 22:473–433, 2002.

[88] R. K. Tyson. *Priciples of Adaptive Optics*. Academic Press, 2nd edition, 1997.

[89] R. K. Tyson. *Introduction to Adaptive Optics*, volume TT41 of *Tutorial Texts in Optical Engineering*. SPIE Press, 2000.

[90] C. R. Vogel, D. W. Arathon, A. Roorda, and A. Parker. Retinal motion estimation in adaptive optics scanning laser ophthalmoscopy. *Optics Express*, 14(2):487–497, 2006.

[91] G. Walsh, W. N. Charman, and H. C. Howland. Objective technique for the determination of the monochromatic aberrations of the human eye. *J. Opt. Soc. Am. A*, 1:987–992, September 1984.

[92] R. H. Webb, G. W. Hughes, and F. C. Delori. Confocal scanning laser ophthalmoscope. *Applied Optics*, 26:1492, 1987.

[93] R. H. Webb, G. W. Hughes, and O. Pomerantzeff. Flying spot tv ophthalmoscope. *Applied Optics*, 19:2991–2997, 1980.

[94] D. Williams, G. Yoon, J. Porter, A. Guirao, H. Hofer, and I. Cox. Visual benefit of correcting higher order aberrations of the eye. *J. Refract. Surg.*, 16:554–559, September/October 2000.

[95] D. R. Williams. Visibility of interference fringes near the resolution limit. *J. Opt. Soc. Am. A*, 2(7):1087–1093, July 1985.

[96] B. C. Wilson and S. L. Jacques. Optical reflectance and transmittance of tissue: principles and applications. *J. Quantum Electron.*, 26(12):2186–2199, 1990.

[97] T. Wilson and C. J. R. Sheppard. *Theory and Practice of Scanning Optical Microscopy.* Academic Press, 1984.

[98] E. Wolf. *Progress in Optics XIX.* North Holland.

[99] J. S. Nelson X. J. Wang, T. E. Milner. Characterization of fluid flow velocity by optical doppler tomography. *Opt. Lett.*, 20:1337–1339, June 1995.

[100] G. Yoon and D. R. Williams. Visual performance after correcting the monochromatic and chromatic aberrations of the eye. *J. Opt. Soc. Am. A*, 19(2):266–275, February 2002.

[101] R. C. Youngquist, S. Carr, and D. E. N. Davies. Optical coherence-domain reflectometry: A new optical evaluation technique. *Opt. Lett.*, 12:158–160, 1987.

[102] R. J. Zawadzki, S. M. Jones, S. S. Olivier, M. Zhao, B. A. Bower, J. A. Izatt, S. Choi, S. Laut, and J. S. Werner. Adaptive-optics optical coherence tomography for high-resolution and high-speed 3d retinal *in vivo* imaging. *Optics Express*, 17:8532–8546, 2005.

[103] Y. Zhang, J. Rha, R. S. Jonnal, and D. T. Miller. Adaptive optics parallel spectral domain optical coherence tomography for imaging the living retina. *Optics Express*, 13:4792–4811, 2005.

Acknowledgements

I would like to take the chance to thank my supervisor, Prof. C. Dainty, for the opportunity he gave me to develop this project, and for the support and facilities he has given me to produce the results presented here.

I also would like to thank Prof. A. Gh. Podoleanu for allowing me to work in his group, sharing his knowledge in OCT and SLO.

I specially would like to thank Dr. A. Bradu, for working side by side with me while building the AO-OCT system. His help has been priceless, and without it this project would not have been possible. It has been a real pleasure to work with someone with such high spirits and so tolerant with me.

My fellowship and research were funded by Science Foundation Ireland, and I am grateful for this support.

I also would like to thank my colleagues in the lab in Galway. Eugenie has been really helpful many times, and Alf always had the answer to my technical questions up to the very last minute. Discussions with David helped

me clarify my ideas, and many times find solutions to problems that seemed they did not have one.

Finally I would like to thank Denis and Larry, because they helped through the journey that this PhD has been, and sometimes the problem is not a camera that does not work.

To everyone of you, *Ciad Mile Failte*.

Galway, October 2006.